REPUBLIQUE ALGERIENNE DEMOCRATIQUE ET POPULAIRE

MINISTERE DE L'ENSEIGNEMENT SUPERIEUR
ET DE LA RECHERCHE SCIENTIFIQUE

UNIVERSITE CONSTANTINE 1
FACULTE DES SCIENCES EXACTES,
DEPARTEMENT DE CHIMIE

N° d'ordre :
Série :

THESE

PRESENTEE EN VUE DE L'OBTENTION DU DIPLOME DE

DOCTORAT *EN* SCIENCES EN CHIMIE

PREPARATION AND CHARACTERIZATION OF NEW MATERIALS BASED ON TiO_2 AND SILVER. APPLICATION FOR ELIMINATION OF MICROORGANISMS AND HARMFUL SUBSTANCES

Option : Chimie Analytique et Physique

PAR

Mr. Oualid BAGHRICHE

Devant le jury :

Président	**:**	**M. M.S. AIDA**	**Professeur**	**Univ. Constantine 1**
Rapporteur	**:**	**M. A. ZERTAL**	**Professeur**	**Univ. Constantine 1**
Co-Encadreur	**:**	**M. J. KIWI**	**Professeur**	**EPFL. Lausanne (Suisse)**
Examinateur	**:**	**M. C. PULGARIN**	**Professeur**	**EPFL. Lausanne (Suisse)**
Examinateur	**:**	**M. A. BENABBAS**	**Professeur**	**Univ. de Jijel**
Examinateur	**:**	**M. S. ZERIZER**	**Maître de Conférences (A)**	**Univ. Constantine 1**

Soutenance prévue le 26. 06. 2013

Acknowledgments

All my respect and gratitude should be first paid to the person who guided me through all the steps of this work in his Laboratory of Innovative Techniques of Environment Preservation. University Constantine 1, Algeria, Prof. A. Zertal.

Several senior researchers and colleagues have contributed in some way to the achievement of this work which has been carried out at the SB-ISIC-GPAO. Institute of the Ecole Polytechnique Fédérale de Lausanne (EPFL).

First of all, I express my thanks to Prof C. Pulgarin, who received me in his laboratory and provided me with advices and assistance all along the period of my research in Lausanne.

I thank especially my co-supervisor Prof. J. Kiwi who proposed the subject and helped me achieve the attained goals of this thesis.

I am grateful to Dr. R. Sanjinés who provided me with the opportunity for my initial research on the PVD thin films.

My acknowledgements also address Prof. Arutiun P. Ehiasarian at M. E.R. I. Sheffield Hallam University, Howard St, Sheffield S11WB, UK for affording us the samples of HIPIMS.

I appreciate the help of my friends Evelyne Toubes-Scherrer, Paula Osorio, Cristina Ruales, Ewelina Kusiak-Nejman.

My friend Sami Rtimi, I acknowledge his contribution to this work, by supporting and helping me.

I should not forget to thank my family and my wife for their support and patience especially my father the source of my inspiration.

Table of contents

CHAPTER 3: EXPERIMENTAL TECHNIQUES

Chapter 1

GENERAL INTRODUCTION

In the last decades, there is a mounting concern about the increasing resistance to antibiotics of toxic bacteria like Methycillin resistant staphylococcus aureus (MRSA), Acinetobacter and Pseudomonas aeruginosa (P. aeruginosa) as well as fungi like Fusarium/Candida Albicans leading to hospital acquired infections (HAI) with the necessary high cost treatment and associated death of human beings having weak immune-system [1,2].

Many studies have shown contamination of common hospital surfaces such as room door handles, sterile packaging, mops, ward fabrics and plastics and healthcare workers' pens by potentially harmful microbes. In addition to this, there is mounting indirect evidence of a link between contaminated surfaces and nosocomial infection [3]. Therefore, (HAI) due to antibiotic resistant bacteria that survive on hospital surfaces for long times [3,4]. One approach to microbial contamination of surfaces is to prepare non-adherent bacterial surfaces since in recent years there has been observed an increased resistance of pathogenic bacteria to synthetic antibiotics.

TiO_2 photocatalysis has been reported to be effective in self-cleaning processes and bacterial inactivation kinetics in the dark and under light irradiation [5]. Several laboratories have addressed the activation of substrates by RF-plasma to increase the binding of TiO_2 on different substrates. Kiwi and co-workers have reported the use of RF-plasma since 2003 to introduce certain functional groups as potential binding sites for TiO_2 and nano-metals and also to increase the textile hydrophilicity [6-10]. RF-plasma and UVC has been used to activate textile and introduce oxygenated polar groups. Daoud et al. have recently worked extensively on the deposition and testing of semiconductor and metallic on textiles introducing self-cleaning and antibacterial functions. [11-12]. Radetic et al. [13] have pioneered the physical application of RF-plasma and corona discharge in self-cleaning and bactericide textiles. The EMPA laboratory [14] has recently reported the deposition of metallic films on textiles pretreated by RF-plasma.

In addition to TiO_2, silver has been employed in the preparation of nanoparticles supported or not to be used as antimicrobial/bacterial agent. Silver nanoparticles present antimicrobial properties when deposited on surfaces and textiles [15].

Sol-gel coating leads to non-uniform Ag-films, with a low antibacterial activity and adhesion [16–17,10]. Depositing Ag by magnetron sputtering has been recently used due to the increasing demand for highly quality functional uniform films outperforming physical vapor deposition (PVD). Ag-surfaces prepared by DCMS sputtering have been effective inactivating airborne bacteria [8]. DCMS-Ag deposition [18] has also been shown to be effective in bacterial inactivation. These Ag-films present uniformity, acceptable bacterial

inactivation kinetics, high adhesion and a relative low fabrication cost. These films on hospital textiles avoid the formation of bacterial biofilms that last for long times acting as a pump to spread toxic bacteria since they stick strongly to glass, prostheses and catheters [3]. On the other hand, magnetron sputtering leads to films showing improved wear resistance, corrosion resistance and defined optical properties.

High power impulse magnetron sputtering (HIPIMS) is gaining acceptance in many applications for surface treatments of metallic surfaces as a recent method for physical vapor deposition (PVD) based on magnetron sputtering due to the HIPIMS higher sputtering energy of several kW/cm^2 and higher electronic densities of $10^{18}/m^3$ compared to $10^{14}/m^3$ and $10^{16}/m^3$ by DCMS and DCMSP successively [19,20]. The films deposited by HIPIMS protect metallic surfaces from corrosion and oxidation as well as wear and have revealed to be important in the deposition of metals on semiconductors and medical devices [21–23]. Recently Stranak et al. have reported HIPIMS for the deposition of Cu–Ti thin films [24]. Using HIPIMS, the high-density plasma at low pressures leads to a higher percentage of charged ions up to 90% and a much higher metal-ion to neutral ratio as compared to DCMS and DCMSP. The metal ion-to-neutral ratio for Ag in our case is estimated as 1:1 up to 4:1 and is also much higher compared to DCMSP with 1:9. In the case of HIPIMS a high plasma density close to the target ionizes effectively the sputtered metal-ions [22,23,25].

Ag and Cu have also been sputtered on ZrN rig metals in Ar-N_2 atmosphere [26]. Ag is immiscible with ZrN and films of AgN are known to be unstable. Ag can be sputtered on ZrN or co-sputtered producing an Ag embedded composite structure with ZrN. are antimicrobial surfaces inactivating Gram-negative and Gram-positive bacteria in the dark and under light [26,27].

The benefits of the Ag and Zr-Ag-N films obtained by sputtering and co-sputtering in a reactive environment (in the presence of N_2) compared the colloidal prepared films (TiO_2/polyester) is in the microstructure of the films showing: uniformity, the ability to control of the film thickness, improved adhesion and fast bacterial inactivation kinetics. Colloidal deposited TiO_2 films are non uniform, not mechanically stable present low adhesion and can be wiped off by using a cloth or a thumb [27]. Another benefit found when using ZrN and Zr-Ag-N films is due to the nitride absorption in the visible range. This avoids the doping used in TiO_2 to extend the optical absorption into the visible region. Doping decreases considerably the photo-activity of the films compared to pristine TiO_2 [28-30].

This thesis is organized in 5 chapters in which the link is preparation and characterization of innovative coated textiles by TiO_2 and silver for *E*. coli inactivation. In the

first chapter we present a literature review of textile, theory plasma, principal of magnetron sputtering (DCMS, DCMSP, and HIPIMS) and photocatalytic destruction of bacteria.

In chapter 2, the deposition method and materials as well as the experimental techniques for characterization of the supported photocatalyst layers by X-ray fluorescence, DRS, XRD, Contact Angle, TEM and XPS is presented.

In chapter 3, the RF-plasma pretreatment of polyester surfaces leading to TiO_2 coatings with improved optical absorption and OH-radical production is reported. Preparation, testing and performance of a TiO_2/polyester for inactivation bacterial are organized around these major topics: (a) the enhanced deposition of TiO_2 on polyester pretreated by RF, (b) the effect of low intensity visible/actinic light on the TiO_2 coated polyester leading to OH-radicals, (c) the optimization of the TiO_2 coating on RF-pretreated polyester and (d) the bacterial inactivation kinetics on TiO_2 RF-plasma pretreated polyester.

Chapter 4 focuses on DCMS-magnetron sputtering, pulsed magnetron sputtering (DCMSP) and HIPIMS as effective methods to functionalizing polyester fibers containing silver nanoparticles on textile surfaces. We compare Ag-samples sputtered in the same chamber and with the same geometry varying the sputtering energy and pulse wave either in the DCMS or DCMSP and compare them with HIPIMS sputtered samples. This leads to different functionalized Ag-polyester structures. Higher current increased the Ag-deposition rate leading to a faster *E. coli* inactivation. Ag-polyester samples will be characterized by TEM, contact angle, X-ray diffraction and XPS.

In chapter 5, we present evidence for: (a) the bactericide role of Ag and ZrN (or Zr) in sputtered films of Zr-Ag-N, (b) the role of Ag and Zr separately in the inactivation kinetics of E. coli, (c) the integration of these two components into a hybrid sputtered film with high antimicrobial activity, (d) the detailed study of the Ag–ZrN film structure and (e) the correlation of DCMSP sputtered Ag-surfaces with the antibacterial kinetics, Zr-Ag-N layer thickness, the layer rugosity and hydrophobicity.

A conclusion is appended to resume the entire study at the end of the 5 chapters.

Chapter 2: Bibliography

1. Textile

1.2. Introduction

Polyester is a term often defined as “long-chain polymers chemically composed of at least 85% by weight of an ester and a dihydric alcohol and a terephthalic acid”. In other words, it means the linking of several esters within the fibers. Reaction of alcohol with carboxylic acid results in the formation of esters. Polyester also refers to the various polymers in which the backbones are formed by the “esterification condensation of polyfunctional alcohols and acids”.

Polyester can also be classified as saturated and unsaturated polyesters. Saturated polyesters refer to that family of polyesters in which the polyester backbones are saturated. They are thus not as reactive as unsaturated polyesters. They consist of low molecular weight liquids used as plasticizers and as reactants in forming urethane polymers, and linear, high molecular weight thermoplastics such as polyethylene terephthalate PET (Dacron and Mylar). Usual reactants for the saturated polyesters are a glycol and an acid or anhydride. Unsaturated polyesters refer to that family of polyesters in which the backbone consists of alkyl thermosetting resins characterized by vinyl unsaturation. They are mostly used in reinforced plastics. These are the most widely used and economical family of resins [14].

1.3. Characteristics of polyester

- Polyester fabrics and fibers are extremely strong.
- Polyester is very durable: resistant to most chemicals, stretching and shrinking, wrinkle resistant, mildew and abrasion resistant.
- Polyester is hydrophobic in nature and quick drying. It can be used for insulation by manufacturing hollow fibers.
- Polyester retains its shape and hence is good for making outdoor clothing for harsh climates.
- It is easily washed and dried.

1.4. Uses of Polyester

The most popular and one of the earliest uses of polyester was to make polyester suits – all the rage in the 70s. Polyester clothes were very popular. Due to its strength and tenacity

polyester was also used to make ropes in industries. PET bottles are today one of the most popular uses of polyester.

1.5. Polyester care tips

Taking care of polyester clothing is really easy and very time efficient.

- Polyester clothing can be machine washed and dried. Adding a fabric softener generally helps. Dry the fabric at low temperatures to get maximum usage from the clothing.
- Though polyester does not require much ironing, if you must then iron warm.
- Polyester can be dry-cleaned with no hassles.

Having learned a little something about polyester and how popular it has become, one could never imagine the history of polyester to be quite so illustrious. The manufacturing process also deserves a more detailed description. The revival and success of polyester is without doubt something that is here to stay.

PET is one of the highest volume polymeric biomaterials. It is a polyester, containing rigid aromatic rings in a "regular" polymer backbone, which produces a high-melting ($T=267C^0$) crystalline polymer with very high tensile strength. It may be fabricated in the forms of knit, velour or woven fabrics and fabric tubes, and also nonwoven felts.

Polyethylene terephthalate (PET) is a linear, aromatic polyester which was first manufactured by Dupont in the late 1940s. It was trademarked as Dacron®; this nomenclature is commonly used when referring to PET, although alternate suppliers of PET are prevalent. Dacron is a common commercial form of PET used in large diameter knit, velour, or woven arterial grafts.

The chemical structure of PET is shown in Figure (1).

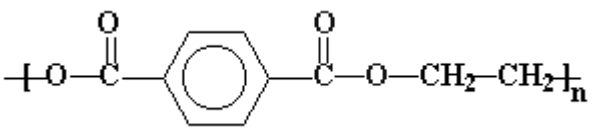

Figure (1): chemical structure of Polyethylene terephthalate

Current medical applications of PET include implantable sutures, surgical mesh, vascular grafts, sewing cuffs for heart valves and components for percutaneous access devices [31]. PET sutures were first introduced in the 1950s and are used for critical procedures where high strength and predictable long-term performance is emphasized [32] Mersilene® polyester fiber sutures were the first synthetic braided suture shown to last indefinitely in the body. Woven PET is commonly used as surgical meshes for abdominal wall repair and similar procedures where surgical "patching" is required. A PET velour fabric patch was first introduced in the 1970s.

Synthetic vascular prostheses are constructed of both woven and knitted PET and have been used clinically since the 1960s. They are used in the repair of the thoracic aorta, ruptured abdominal aortic aneurysms, and to replace iliac, femoral and popliteal vessels.

Heart valves have incorporated PET by using it as a sewing cuff around the circumference of the valve to promote tissue in growth and to provide a surface to suture the valve to the surrounding tissue. Over one million heart valves have been implanted since their inception in the late 1970s.

Percutaneous tunneled catheters incorporate a PET cuff to stabilize catheter location and minimize bacterial migration through the skin. In addition, braids and similar constructions made of multifilament PET yarns have shown promise for repairing tendons and ligaments [33] and for fixation of intraocular lenses.

In conclusion, Polyester is one of the most resistant low cost fabrics. The polyester fabrics have been chosen because they are flexible and stable materials produced in large quantities. In recent years, the modification of textiles by TiO_2 and nanoparticales (Ag, Cu, ..) aiming at pollutant degradation and self-cleaning processes has been reported. This textile presents a large surface area making it suitable as a substrate for self-cleaning and antibacterial applications [9,34].

2. RF-plasma treatment

2.1. Introduction

In recent years, the advances made in developing surface treatments have successfully altered the chemical and physical properties of polymer surfaces without affecting the properties of the bulk (especially mechanical properties). Common surface modification techniques include treatments by flame, corona, plasmas, photons, electron beams, ion beams and X-rays [35,36].

Plasma processes have become important industrial processes in modifying polymer surfaces and it is probably the most multilateral surface treatment technique [35,37].

These treatments have been widely used in a number of applications such as [35-37]:

- Improving adhesion of coatings to metals and polymers based on producing special functional groups at the surface for specific interactions with other functional groups.
- Increasing the hydrophobicity, wettability and introduce surface cross-linking.
- Enhancing biocompatibility of implants.
- Manufacturing of semiconductor devices.

In the photocatalysis area, plasma treatments have been used to modify the surface of films (activation) and to increase the binding of TiO_2 on different substrates [13,16,38-42]. Many studies, like the one of Mihailovic et all, have reported the use of RF-plasma since 2003 to introduce certain functional groups as potential binding sites for TiO_2 and nanometals and also to increase the textile hydrophilicity [10, 16, 38]. Also, these studies tackle the fixation of TiO_2 and highly active nano-particulate antibacterial metals on a variety of substrates [7,10,16,42-44].

2.1. Notion of plasma

The plasma state is often referred to as the fourth state of matter, and it can be defined as a gas containing charged and neutral species including some of the following: electrons, positive ions, negative ions, radicals, atoms, and molecules. In a plasma, the average electron energy ranges between 1 and 10 eV, the electron density varies from 10^9 to 10^{12} ions/cm^{-3} and the degree of ionization can be as low as 10^{-6} or as high as 0.3.

2.2. Overview of gas discharge plasma

A plasma generation and sustenance can be produced through different energy sources among which radio-frequency (RF-Plasma) is dealt with in details in the following.

2.3.1. Direct current (D.C) glow discharges

The applied high potential between two electrodes placed in a gas originates in the breakdown of the latter into positive ions and electrons which pushes a gas discharge [45].
The mechanism of the gas breakdown can be explained as follows: a few electrons are emitted from the electrodes due to the omnipresent cosmic radiation. In the absence of potential difference, the discharge cannot be obtained. However, when a potential difference is applied, the electrons are accelerated by the electric field in front of the cathode and collide with the gas atoms. The most important collisions are the inelastic collisions, leading to excitation and ionization. The excitation collisions, followed by de-excitations with the emission of radiation, are responsible for the characteristic name of the 'glow' discharge. The ionization collisions create new electrons and ions. The ions are accelerated by the electric field toward the cathode, where they release new electrons by ion induced secondary electron emission. The electrons give rise to new ionization collisions, creating new ions and electrons. These processes of electron emission at the cathode and ionization in the plasma make the glow discharge a self-sustaining plasma (Fig 1).

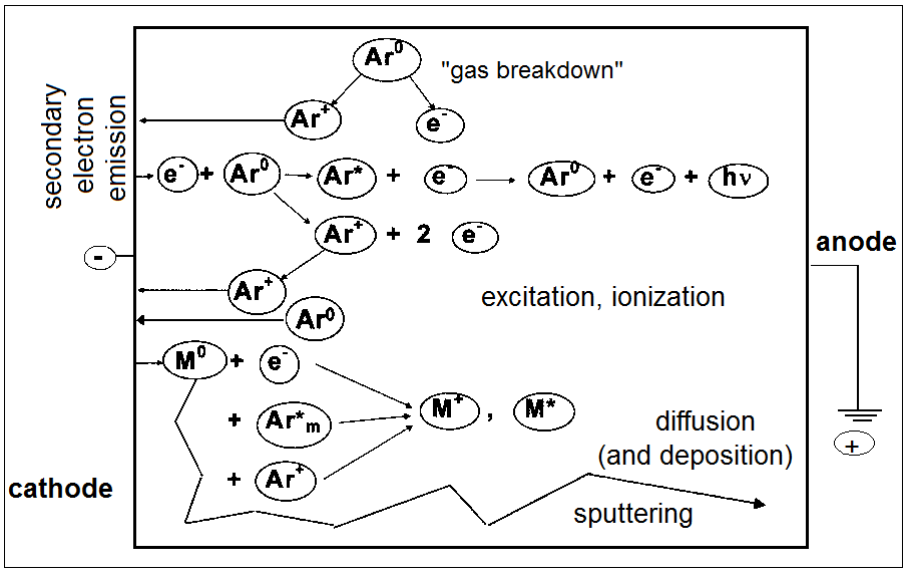

Figure (1) : Schematic overview of the basic plasma processes in a glow discharge [45]

The glow discharge exhibits other important processes such as the phenomenon of sputtering which we will tackle in details in the section ahead.

The most important discharge conditions that a DC glow discharge can operate by are the product of pressure and distance between the electrodes. The pressure can vary from

below 1 Pa to atmospheric pressure. For instance, at lower pressure, the distance between cathode and anode should be longer to create a discharge with properties comparable to those of high pressure with small distance. The voltage is mostly in the range between 300 and 1500 V, but for certain applications it can increase to several kV. The current is generally in the mA range. The discharge can operate in a rare gas (most often argon or helium) or in a reactive gas (N_2, O_2, H_2, CH4, SiH_4, SiF_4, etc.) as well as in a mixture of these gases.

2.3.2. Radio-frequency (RF) discharges

The use of DC in a plasma requires electrically conductive electrodes. If one or both of the electrodes are non-conductive, e.g. when the glow discharge is used for the deposition of dielectric films, where the electrodes become gradually covered with insulating material, the insulator would charge up and terminate the discharge. The use of an alternative current AC power source can alleviate this problem because positive charges accumulated during one half-cycle can be neutralized by electron bombardment during the next cycle. The frequencies generally used for these alternating voltages are typically in the radiofrequency (RF) range (1 kHz–10^3 MHz; with a most common value of 13.56 MHz) since the conventional AC frequency of 50 Hz is usually not very effective because the time it takes for the insulator to charge up is much less than half the period of the AC supply. Under this circumstance, the discharge is found to be off most of the time. A frequency of 50-100 kHz is sufficient to provide a continuous discharge. An RF discharge will have many of the same qualitative features as a DC glow discharge. At low frequencies, where the ions can follow the electric fields, the discharge will behave similarly to a DC discharge. At high frequencies, the ions will no longer be able to follow the electric fields but will respond to the time-averaged fields. At frequencies above 500 kHz, the half cycle is so short that all electrons or ions stay within the interelectrode volume. This significantly reduces the loss of charged particles from the system; hence, a lower voltage is required to maintain the glow discharge. In addition, at these frequencies, the regeneration of the lost electrons and ions occurs within the body of the plasma through the collisions of electrons with gas molecules. This mechanism does not require the electrodes to be in contact with the plasma. Therefore RF plasma can be initiated and sustained by external electrodes outside the reactor vessel due to the increasing frequency or the coil wound around the reactor vessel. This kind of reactor is the one used in this research. In practice, many RF GD processes operate at 13.56 MHz, because this is a frequency allotted by international communications authorities [45].

A typical system consists of a gas inlet, a reactor vessel, a vacuum pump, a matching network, and a power source as shown in figure (2).

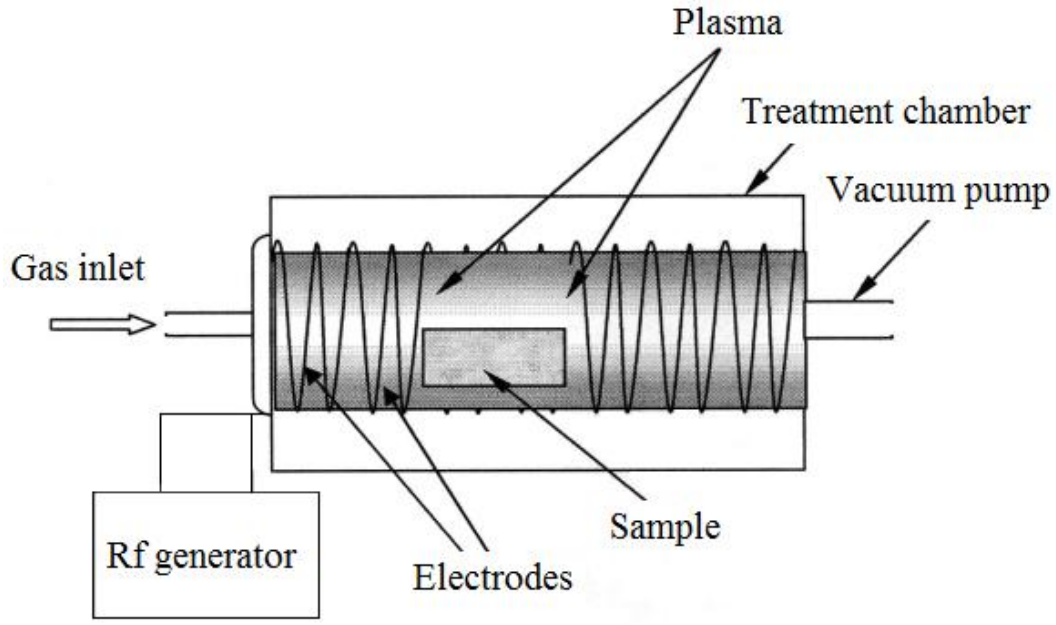

Figure (2): Schematic representation of an atmospheric pressure glow discharge [45]

2.3. Reactions between plasma and polymer surfaces

Typically, in the plasma treatment of polymers, the active species of plasma such as radicals, ions, electrons, and photons interact strongly with the polymer surface. The collision of these energetic active species with the surface results in the transfer of their energy to lattice atoms. Consequently, some of the covalent bonds at the surface break, leading to the formation of surface radicals making the surface more reactive. A variety of chemical groups (hydroxyl, carbonyl, amino, or peroxyl group) can be grafted onto the surface of the polymer [46]. The varieties of the type of process gas used effects on the groups added to the surface of the polymer. Different types of gases such as argon, oxygen, nitrogen, fluorine, carbon dioxide, and water can produce the unique surface properties required by various applications. For example, in this study, oxygen-containing plasma treatment in the RF-cavity can increase the oxidative functionalities of fabric.

2.4. Surface activation and functionalization of polyester fabrics by RF-cavity

For the generation of RF-plasma, low pressures of 0.1-1 Torr are required to enhance the capture length of the electrons generated by the applied electric field. When applying a vacuum in the RF-cavity, the pressure is reduced and the O_2 left produces O* and atomic O, singlet $1O_2$, anion radicals O^- and cation radicals like the O^+. The collisions of the excited

oxygen species with each other are drastically decreased by diminishing the number of initial molecules. This allows the O* and atomic O in the RF-cavity to react with the polyester introducing oxidative functionalities [35, 47-51]. In the plasma, the ions/molecules/electrons attain temperatures up to a few hundred degrees with high energies but lasting only nanoseconds in a system that is not in equilibrium. Within these short lifetimes, the plasma activates non-heat resistant textiles like polyester not damaging their structure and introducing oxygenated functionalities modifying the textile surface.

In the RF-cavity, the plasma discharge breaks the H-H and C-C bond scissions due to the non-uniform local heating of the fabric [48,49] segmenting partially the polyester fabric [50]. This interaction is sufficient introduce the oxidative functionalities: -C-O^-, -COO^-, -COH^-, O-C=O^-, - COOH, phenolic and lactam groups in the presence of O_2 (air) [35, 42, 47, 48]. These negative charged functionalities will react with the slightly positive Ti^{4+} charge of the TiO_2 by electrostatic attraction leading to surface coordination/chelation [7,44]. The TiO_2 nanocrystals will attach to negatively charged substrates like cotton by exchange/impregnation/electrostatic attraction as recently reported [51].

The attachment of the TiO_2 occurs for similar reasons to the ones taking place between the enhanced negative surface of polyester and the semiconductor due to the RF-pretreatment. Besides the functional oxygenated groups mentioned above, synthetic textile fibers have been reported to form a significant number of percarboxylate, epoxide, and peroxide groups upon RF-plasma pretreatment [16,40,41,49,53].

There are a number of parameters that determine the rate of plasma polymer deposition and the chemical and physical nature of the deposited films and modified surfaces. Yasuda, 1985 and Shen and Bell, 1979 have discussed in details the effects of these parameters [35].

2.5. Depth of modification

In general, the depth of surface modification mainly depends on the power level and treatment time. For plasma-treated polymer samples, the depth of the surface modification is typically of several hundred Å and has been studied by surface-sensitive techniques such as angle-resolved XPS [35].

We have chosen the technique of plasma in this study because of the varied advantages it contains:

1) Modification by plasma treatment is usually confined to the top several hundred ångström and does not affect the bulk properties.

2) Excited species in a gas plasma can modify the surfaces of all polymers, regardless of their structures and chemical reactivity.
3) By choice of the gas used, it is possible to choose the type of chemical modification for the polymer surface.
4) The use of a gas plasma can avoid the problems encountered in wet chemical techniques such as residual solvent on the surface and swelling of the substrate.
5) Modification is fairly uniform over the whole surface.

The disadvantages of the plasma processes are as follows:

(1) Plasma treatments must be carried out in vacuum. This requirement increases the cost of operation.
(2) The process parameters are highly system-dependent; the optimal parameters developed for one system usually cannot be adopted for another system.
(3) The scale-up of an experimental set-up to a large production reactor is not a simple process.
(4) The plasma process is extremely complex; it is difficult to achieve a good understanding of the interactions between the plasma and the surface necessary for a good control of the plasma parameters such as RF volume, RF frequency, power level, gas flow rate, gas composition, gas pressure, sample temperature, and reactor geometry.
(5) It is very difficult to control precisely the amount of a particular function group formed on a surface.

3. Magnetron Sputtering

In this section, we will discuss in detail the techniques that have used in our work such as: DC magnetron sputtering (DCMS), DC Magnetron Sputtering Pulse (DCMSP) and HPPMS (High Power Pulsed Magnetron Sputtering).

3.1.Introduction to Thin Films Deposition

Thin films are played an important role in materials science. Some deposition techniques enable the synthesis of materials whose properties are superior compared to other methods of preparation.

In this work, this term refers to a deposition process, shown schematically in Figure (1).

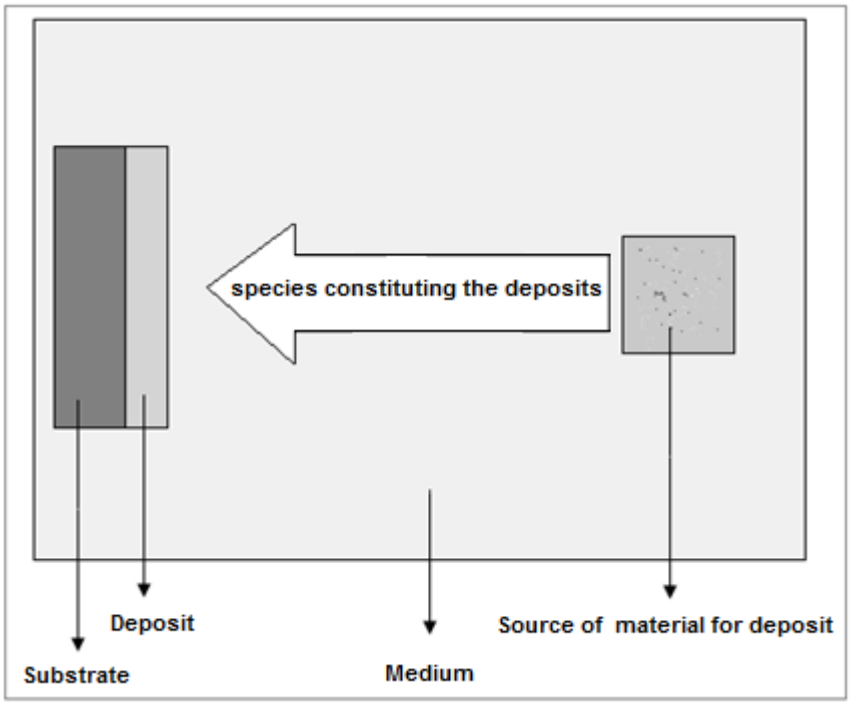

Figure (1): Schematic of a typical deposit.

As shown in figure (1), there are three steps in any physical vacuum deposition (PVD) process: Creation of an evaporant from the source material, transport of the evaporant from the source to the substrate (item to be coated), and condensation of the evaporant onto the substrate to form the thin film deposit.

3.2.Classification of thin film deposition

A classification is presented for thin film deposition technologies according to evaporative glow-discharge, gas-phase chemical and liquid-phase chemical process [54].

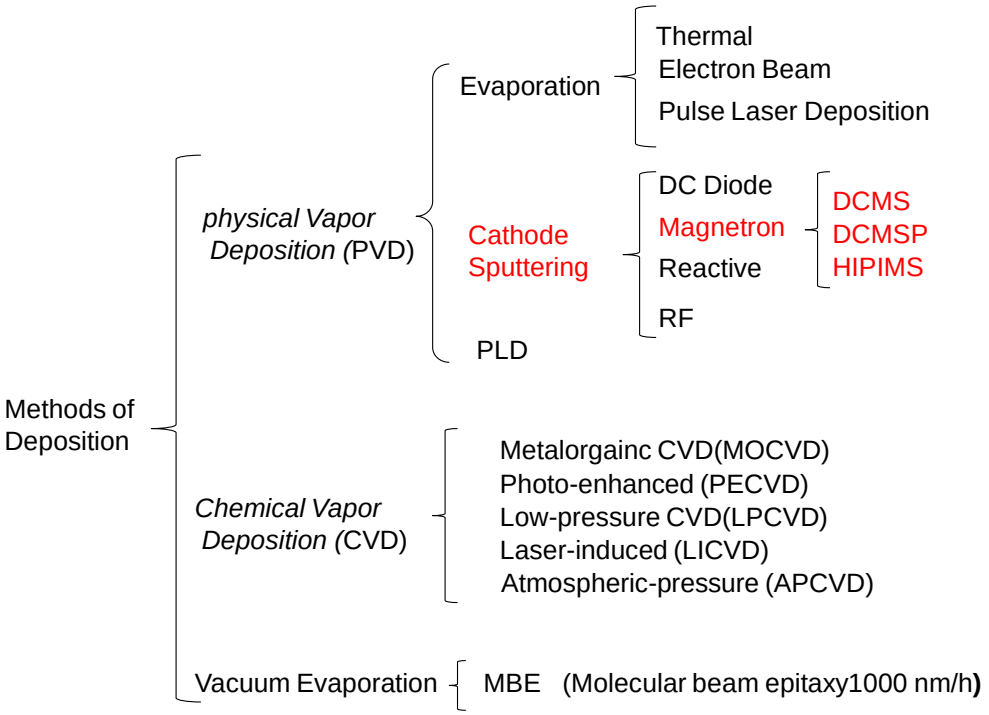

Organization chart of Deposition Methods

This organization chart shows the site of magnetron sputtering in different methods of deposition.

3.3.Advantages of sputtering

Actually, and compared to other thin film deposition methods such as evaporation, CVD, several advantages make the cathode sputtering technique more suitable and is characterized by the following advantages:

- Relatively low cost deposition method.
- Very good thickness uniformity and high density of the films.
- Good adhesion of films on substrates.
- Its capability of deposition around corners allows three-dimensional geometry parts to be uniformly coated.
- The possibility of using temperatures lower than 200°C (down to room temperature) increases the number of substrates to which the PVD process

can be applied (textiles, plastics, watch with sensitive spring components, porous cast materials, etc.).

- By reactive sputtering in rare/reactive gas mixtures many compounds can be deposited from elemental (metallic) targets.
- Cathode sputtering easily enables coating using metal alloys, such as Ti-Al, Ti-Zr, etc. This versatility is only limited by the availability of targets with complex chemical compositions.

3.4.Technology of Sputter Processes

3.4.1. Definition

Magnetron sputtering is a widely used PVD (Physical Vapor Deposition) technique to deposit thin films. This technique is based on the generation of lowpressure magnetically enhanced glow discharge plasma – magnetron discharge.

3.4.2. History of Sputtering

The depositions by sputtering are obtained by Ar ion bombardment of the target cathode. Sputtering was first described in 1852 by the Grove [55, 56]. Depositions by sputtering have been studied by Wright in 1877 while Edison patented in 1904 silver sputtered on a wax cylinder for photography [57]. Work on radars during World War II helped develop the technique of planar magnetron sputtering. The physics of sputtering has been studied by Wehner [58] and the state of research is described references [56, 59, 60] and by Mattox [57]. Today the deposition of thin films by sputtering is widely used in production processes. Important operational areas of the sputtering technology are optics (e.g. architectural glass, reflectors, lenses), optoelectronics (solar cells, photodiodes, liquid crystal displays - LCD), electronics (e.g. microchips,), memory technology (e.g. laser discs, magneto-optical media), the surface protection (tools, machine parts) or the barrier technology (diffusion barriers for example in flexible packing) and in the synthesis of nano-materials [61].

In the biomedical area, magnetron sputtering has been used to modify biomaterials and biofilms for various applications including devices or implants for diagnosis and therapy. For example, recently magnetron sputtering has been used as an effective method of functionalizing cotton and polyester fabrics containing silver nanoparticles as *Escherichia coli* (*E. coli*) inactivation agent [40, 62]. Also Ag films have been reported to prevent bacterial colonization of glass surfaces [63, 64] prostheses and catheters [19], dental implants [65] and

on several metal solid surfaces [66]. Ag-surfaces prepared by DCMS sputtering have been effective inactivating airborne bacteria [8]. Cu-surfaces prepared by DCMS [67] and DCMSP sputtering have recently been reported by the EPFL group [68]. DCMS-Ag deposition [18] has also been shown to be effective bacterial inactivation. These Ag-films and Cu-films present uniformity, acceptable bacterial inactivation kinetics, high adhesion and a relative low fabrication cost. These films on hospital textiles avoid the formation of bacterial biofilms that last for long times acting as a pump to spread toxic bacteria since they stick strongly to glass, prostheses and catheters [19,64,65].

The terms sputtering, sputtered films, sputter PVD or sputter coating are usual synonyms for this technology.

3.5. The physical mechanism of sputtering

The sputtering process is shown generically in figure (2). The vapors in the sputtering process are generated by elastic collisions between the ions and the surface of the target. A bombardment ion is accelerated into a substrate and the species used for bombardment is typically Ar^{+}, due to its chemical inertness and low coast. Argon also has the advantage that its atomic mass is similar to that of many of the metals such as Ti, Ag and Cu.

Once the bombardment ion collides with the target surface, an atom can be ejected or sputtered after a cascade of collisions in a depth of 5 to 10 nm from the surface of the target to condense on a substrate to form a thin film as indicated in figure (2).

The cylindrical chamber is evacuated (pressure from $p = 10^{-6}$ to 10^{-10} hPa) and filled with a plasma gas (Ar) until pressure reaches $p = 10^{-3}$ to 10^{-1} hPa. An electrical discharge creates plasma and the positive ions are accelerated towards the cathode target in a negative potential U = 0.5-5 KV [56].

There are a number of other ion/surface interactions, one of which is the generation of secondary electrons. These electrons are accelerated into the plasma causing further ionisation collisions. However the majority of the electrons produced will not be involved in collisions but instead escape to the anode, making the process rather inefficient.

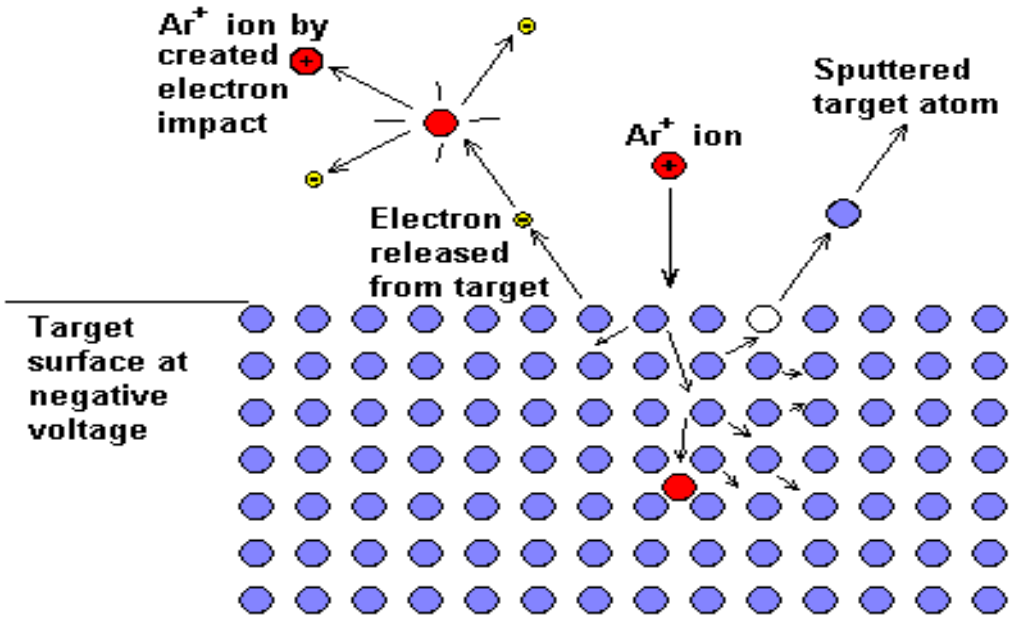

Figure (2): The sputtering cascade process

The sputtering yield is a measure of the number of atoms ejected from the target for each bombardment ion.

This sputter yield depends on:

- Type of target atom
- Binding energy of target atoms
- The nature of the incident ions (noble gas mass higher or lower, or gas reactive)
- The energy of incident ions.
- Relative mass of ions and atoms
- Angle of incidence of ions

The energy of the incident ion must exceed a certain threshold for sputtering to become possible. This threshold is approximately four times the energy of binding of the material to be sputtered.

Table 1 shows the sputtering yield for different materials bombarded by argon ions. The minimum energy that the atom can be ejected from the target can be estimated E = 25 eV [57]. The ejected atoms have energies comparable to ion-incident. Therefore, the speed of sputtered atoms can reach 10 km / s.

Table1: Sputtering yield for Ar^+ ion energy E = 500 eV [57].

Target material	Be	Al	Si	Cu	Ag	W	Au
m_c	9	27	28	64	106	184	197
Spuettering yield [atomes/ion]	0,51	1,05	0,50	2,35	2,4 – 3,1	0,57	2,4

Although all materials can be sputtered, DCMSP and radio frequency must be used for the deposition of insulator materials.

3.6. Sputtering techniques

3.6.1. Direct Current Diode sputtering deposition (DCD)

Applying a voltage between two electrodes in contact with a gas remains a conventional method to produce a discharge: it's the "diode" technique. Historically, the system diode sputtering was first used to both erode surfaces and for sputter deposition. In this system, the cathode is the target and the anode (substrate) is placed on the ground potential as show in figure (3). To support the discharge, the cathode (target) must be conductive. The system is simple, but the rate of deposition is low and has high prices (difficulty of sputtering or depositing insulators) [57].

The low rates are due to the low ionization cross section for electron-impact ionization of most gas species. This means that some of the secondary electrons can pass right through the plasma and hit the anode. While this is nice for current flow, the loss of this secondary electron means that no new ions are made from gas-phase collisions. This limits the net current flow and hence the sputtering rate.

The system diode is limited (almost not used) because it required gas pressure high around 3-300 Pa and the voltages are too large (1-3 kV) which can damage the layer, the deposition rates are too low, low ionisation efficiencies in the plasma, and substrate heating effects. These limitations have been overcome by the development of magnetron sputtering through a special magnetic field configuration and, more recently, unbalanced magnetron sputtering.

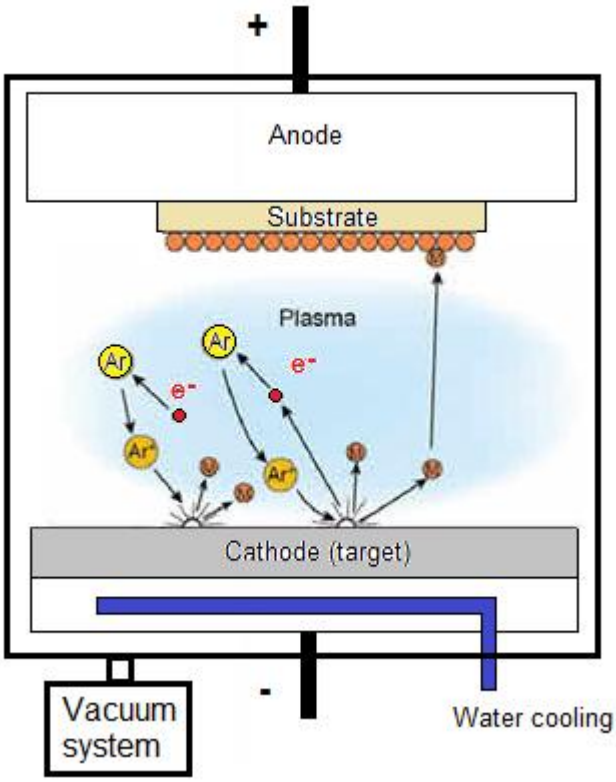

Figure (3): Schema of simple DC diode sputtering system. The vacuum system would operate at pressures in the mTorr to low Torr range.

3.6.2. Direct Current Magnetron Sputtering (DCMS)

Direct current magnetron sputtering (DCMS) is a widely used technique for deposition of metal for numerous technical applications. The magnetron uses magnetic fields to increase the plasma density. The magnetron effect is obtained by implanting permanents magnets behind the target. The magnetic field, applied to the plasma is often perpendicular to the electric field Fig (4), allows extending the electrons trajectories which, subject to the *Lorentz* force (5-2-1), perform a circular movement around the magnetic field lines and have an orthogonal drift velocity. The drift velocity is defined by the relation (5-2-2).

$$\mathbf{F} = -e(\mathbf{E} + \mathbf{v} \cdot \mathbf{B}) \quad (5\text{-}2\text{-}1)$$

$$\overrightarrow{v_d} = \frac{\vec{E} \wedge \vec{B}}{B^2} \quad (5\text{-}2\text{-}2)$$

With their long trajectory, the electrons are able to ionize more atoms and increase the concentration of ions in the plasma, and consequently of the sputtering yield of the target.

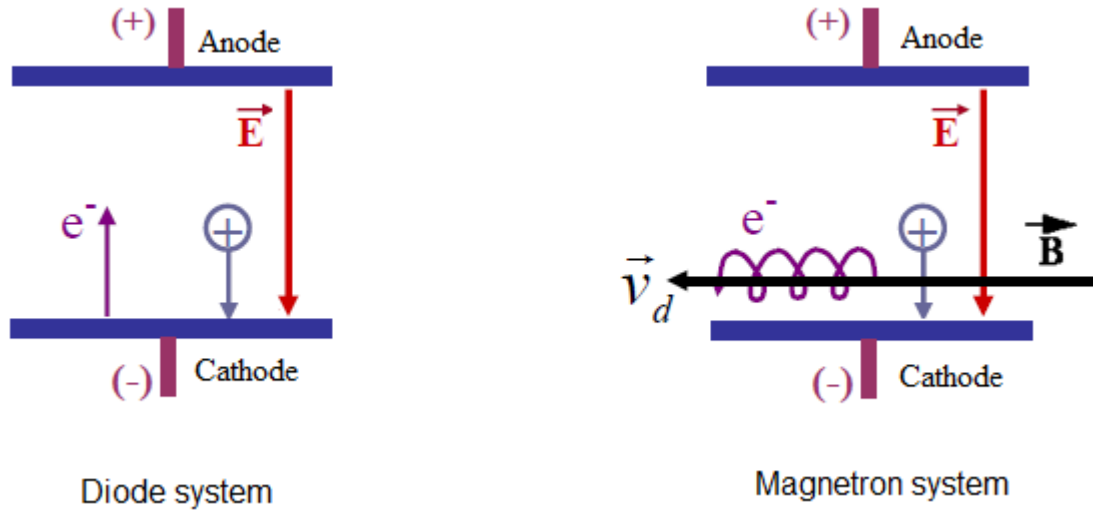

Figure (4): Comparison of electrons trajectories in the case of a diode and a magnetron system

The shape of the magnetic field lines for a circular cathode is shown in figure (5). The field lines (black arrow in the figure) are radial at the cathode. The plasma is then denser where the magnetic field is more intense.

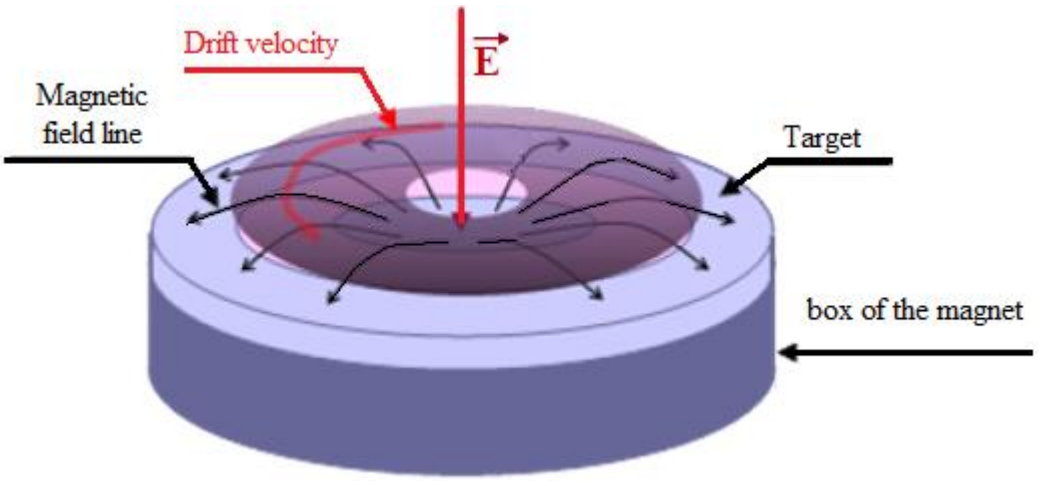

Figure (5): Typical shape of the magnetic field lines of the magnetron cathode circular

There are several more complex configurations of magnetron structure, which may involve removable magnet, variable magnetic fields and more complicated geometries, etc. [69, 70]. One of the most common geometries encountered in research laboratories is the circular planar geometry. This is the geometry used in the unit used in this thesis as shown in

figure (5). For example, Beister et al. [71] show a double magnetron plan to deposit SiO_2 for optical applications. Another example is by Hosokawa [72] lead to deposits with uniform thickness (± 5%). Degout et al. [73] associated a planar magnetron system with a plasma canon by for deposition of TiN [74].

The magnetrons are widely applied in many areas. The advantages compared to the diode: low voltage (100-600 V), higher rate. Apart from the many advantages that make the magnetron discharge used for thin film deposition, this type of discharge has some disadvantages; the heterogeneity of discharge. In fact, the flow of the particles is highly anisotropic and inhomogeneous which can strongly influence the structure and properties of the film. DCMS leads to ionisation of 1-5% of the total [75], in the range of 1-20 eV at 200-300 V [76]. The energy deposited by the sputtered atoms in the thin film forming is limited, because is reduced by collisions with gas.

In the other hand, during the conventional deposition of thin films with DC magnetron reactive discharges (reactive gases such as O_2, N_2 are added to the noble gas Ar), the target itself gets covered with an insulating layers as shown in figure (6) in consequence, due to the negative polarity of the target, positive charges are accumulated on the target surface which leads to arc inducing process instabilities. This leads to inhomogeneity and defects in the films [77].

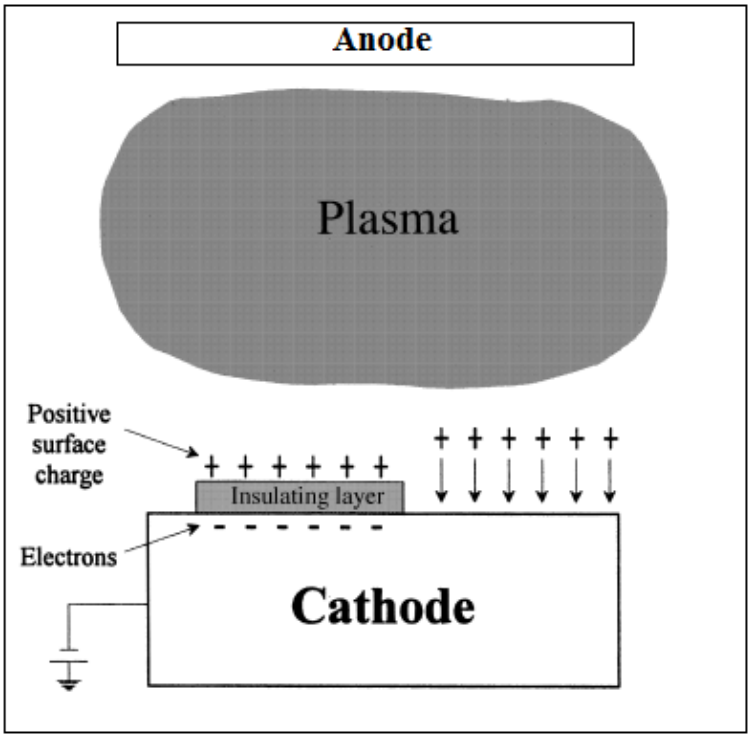

Fig (6): Positive charge accumulation on the surface of an insulating layer [77]

Besides of the inhomogeneity of discharge, the degree of ionization of metals is relatively low and been reported to be 1–5% and the equilibrium potential given by the balance of electrons and metal-ions is slightly positive [75, 77, 78].

The quantity of atoms ions ejected from a conventional magnetron discharge is therefore insufficient to contribute significantly to the growth of the layer. In order to prevent arcing (target poisoning in reactive sputtering), control the energy is necessary taking into account of additional ionization techniques.

3.6.3. Direct Current Magnetron Sputtering Pulsed (DCMSP)

Pulsed magnetron discharges were successfully introduced in coating technology to prevent arc formation during the deposition dielectrics of thin films by neutralization of surface charges. It is possible to eliminate arc formation by not allowing positive charges to accumulate through a periodic interruption of the negative DC voltage at the target which is is commonly known as pulsed direct current magnetron sputtering (DCMSP) [79].

There are two ways of applying the pulsing technique, namely: the unipolar and bipolar pulsing will be discussed.

3.6.3.a. Unipolar pulsed magnetron sputtering

In the case of a pulse unipolar that is given in the schematic rectangular waveform in figure (7). The positive charges accumulate on the dielectric during the negative phase of polarization of the target. The time to breakdown is of the order of ten microseconds; the polarization phase (t_{on}) does not exceed this magnitude. During the pulse-on time (t_{on}), sputtering of target material occurs and is accompanied by charge accumulation on the surface of the insulating layer. During the interruption (cut the discharge) referred to as the off-time (t_{off}), the surface of the insulating layer is then subject to a net negative flux of the electrons and then the accumulated positive charge is neutralized [77, 80].

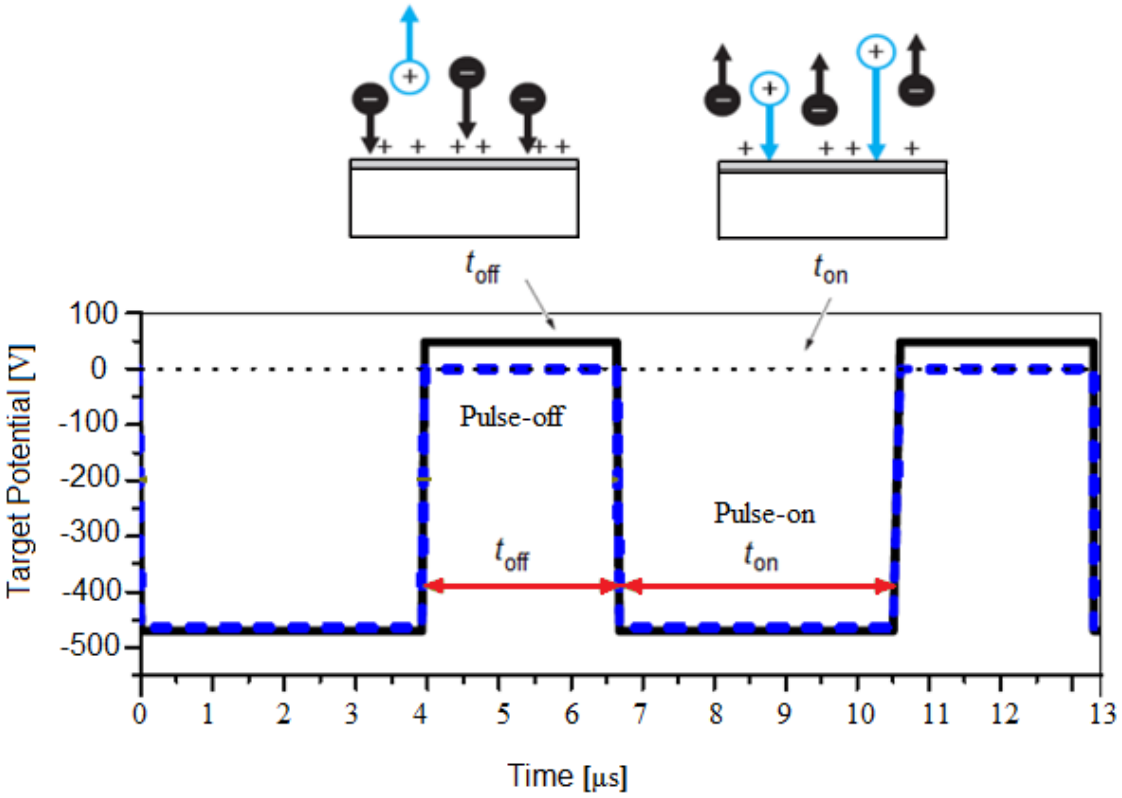

Figure (7): Typical target potential waveforms in pulsed magnetron sputtering; model for both unipolar (dots) and asymmetric bipolar sputtering (line).

The time on (t_{on}) has to be short enough to prevent arc formation. The discharge has to be switched off (t_{off}) before enough charge for a breakdown is accumulated.

For example, Frach et al. [81] has been obtained process stability, a lower arcing frequency and a good film quality of Al_2O_3, by using medium frequency pulsed power, with a pulse-on time for approximately 10-20 μs and a pulse-off time for approximately 10 μs. Other examples of effectiveness of this technique are the work carried out by Pond et al. [82] they reactively deposited films of Ta_2O_5, Nb_2O_5 and SiO_2. Belkind et al [83], found reactive sputtering of Al_2O_3 without arcing by applying to the target the pulsing frequency.

3.6.3.b. Bipolar pulsed magnetron sputtering

Instead of switching of the magnetron for a certain period of time to discharge the charged surface of the insulating layer via the plasma, as was the case in the unipolar pulsed magnetron sputtering, the surface of the insulating layer, in the bipolar mode, is discharged as a result of electron-bombardment when the polarity of the magnetron is reversed, see figure

(7). Bipolar pulsed magnetron sputtering can be carried out using one magnetron or two magnetrons [77].

As we have seen previously, many researches have shown the properties of dielectric films by utilized unipolar and bipolar pulsed magnetron sputtering [79, 81-83]. However, the using the pulse discharge (DCMSP) instead of a DC magnetron (DCMS), even without the necessity of arc prevention (depositing metals without gas reactive), has quickly emerged. There are many good examples are given by [84-89]. The results show that pulsed sputtering can change the properties of other materials apart from dielectrics [84-87]. Henderson et al [84] have used a pulsed magnetron (DCMSP) to deposit titanium in Argon, the titanium films show improved adhesion and surface roughness for the same average input power compared with DCMS films. Bradley et al [87] deposit aluminium (Al) films; they found an increase in the energy flux of charged particles arriving at the substrate by more than 35% when using a pulsed discharge DCMSP instead of DCMS with simultaneously lower deposition rate. This is a much smaller increase observed by Glocker [86] who found 50% and correlated this with an increase in plasma density by a factor of 4 and of the electron temperature by 40%. Recently, and based on these results, the EPFL laboratory has deposited Cu on cotton substrate using both methods DCMS and DCMSP to testing inactivation bacterial. The results shown for Cu-layers on cotton show that bipolar sputtering (DCMSP) accelerates the Cu-cotton biocide action compared to DC magnetron sputtering [67]. This effect is due to the formation of different microstructure/properties of the Cu nanoparticles on the cotton [67, 68].

3.6.4. High Power Impulse Magnetron Sputtering (HIPIMS).

The one of interest in developing the magnetron sputtering technology is to increase metal ionization. Furthermore, the plasma density of the conventional magnetron discharges both DCMS and DCMSP increases with increased power applied to the cathode. But the maximum power applied to the cathode is limited by the heating of the target provided by bombardment of the positive ions. However, it is possible to avoid this limitation, by decreasing the duration of pulses and separate them by a period of time sufficiently long so that the heat accumulated on the surface of the target during the discharge can be removed. This technique has been briefly reviewed by Helmersson et al [90], the new deposition technique was called in literature HPPMS (**H**igh **P**ower **P**ulse **M**agnetron **S**puttering) [91]. Later, several research groups adopted the alternative name HIPIMS (**Hi**gh **P**ower **I**mpulse **M**agnetron **S**puttering) for this technique [92].

Sputtering has lately evolved toward the higher ionization of ion/metal in the plasma flux. This enhances the film uniformity, the production of highly ionized metal-ions, the film adherence and compactness [20,23,25]. High power impulse magnetron sputtering (HIPIMS) is an important development in the sputtering field [21, 93] and is gaining acceptance in many applications for surface treatments of metallic surfaces applying several kW/cm^2 leading to high plasma densities of $10^{19}/m^3$ compared to $10^{16}/m^3$ and $10^{14}/m^3$ by DCMSP and DCMS respectively [23, 90]. HIPIMS technology produces high power homogeneous plasma glow at high currents up to 2000 V and 10 A and degrees of ionization up to 70% [94-98]. However, the deposition rate is generally lower than the conventional magnetron sputtering for average equivalent powers; the rates of deposition in HIPIMS are typically of the order of 25-35% for the same average power and under the same experimental conditions [92, 98]. Various studies have reported on this lower deposition rate [99-102]. One of the possible explanations for the reduction in the rate of deposition is that the sputtered material is ionized close to the target. Part of these metal ions is attracted back to the target surface by the negative potential applied to the cathode [103]. However, if the ion is attracted back to the target it will act as a sputtering particle. A reduction in the deposition rate is then expected to occur especially for metals with a low self-sputtering yield.

3.7.Reactive Sputtering

Sputtering discharge in reactive gases can be defined as the sputtering of a metal targets in the presence of reactive gases (O_2, N_2) that gas react with both the ejected target material and the target surface. The reactive gas leads to formation of thin films such as oxides, nitrides, carbrides, sulphides or fluorides [104]. Several factors characterize the reactive sputtering which made it popular, among these: it is capable of producing thin films of defined stoichiometry [105].

Binary and ternary transition metal nitrides are attractive materials because of their hardness, high melting point, and electrical and optical properties [106]. They are interesting materials for hard wear-resistant coatings in machining industry, optical and decorative coatings, diffusion barriers in microelectronics, electrodes in semiconductor devices, and biomedical applications [107,108].

In binary metal nitrides, their optical and mechanical properties intensively depend on the nitrogen composition. For example, the stoichiometric nitride ZrN is metallic-like with a gold, yellow color; it is the thermodynamically stable phase. On the contrary, the Zr_3N_4 compound is a metastable phase; it is insulating and almost transparent [109]. But these metal

nitrides have been poorly explored for the inactivation of micro-organisms/bacteria. Most of the transition metal nitrides crystallizing in the fcc B1 type (NaCl type) are interstitial compounds. While keeping their crystal structure, they can accommodate high concentration of vacancies in the nonmetal sub-lattice (i.e., $TiN_{,,}$ $ZrN_{,}$ NbN_x and MoNx with $0.5<x<1.1$). With regard to metal vacancies, only few nitrides such as ZrN_{1+z} and HfN_{1+z} have been reported as cation deficient with concentrations of metal vacancies in the range of 25%. Only few studies have been dedicated to Zr-based ternary nitrides, such as Zr–Ti–N, Zr–Cu–N, and, in particular, to Zr–Al–N [110]. Ternary compounds allow to adjust parameters like lattice constant, hardness, elasticity, and thermal expansion or stability against corrosion to optimize the overall performance of the coating.

Recently reports have appeared in the literature that some Ag or Cu based transition metal nitride (TmN) nanocomposites such as Ag–TiN and Ag–ZrN [111–113]. Me–TmN (Me = Ag, Cu, Pt) has been investigated for biological applications showing the formation of Ag–TmN bi-phased nanocomposites with separated Ag and cubic fcc-TmN nano crystallites. This occurs due to the non-miscibility of the Ag atoms in the fcc-TmN phase due to the higher Ag-nitridation energy compared to the TmN formation energy.

4. Theory of Photocatalysis and Bacteria

4.9. Heterogeneous Photocatalysis – TiO_2

Heterogeneous photocatalysis is a rapidly emerging field in the environmental chemistry. It has become apparent that organic, inorganic and microbial pollutants be able removed by hydroxyl radicals generated on the semiconductor surfaces in various media (water, soil and air) [114, 115]. Heterogeneous photocatalysis is a technology based on the irradiation of a catalyst, usually a semiconductor, which may be photoexcited to form electron-donor sites (reducing sites) and electron-acceptor sites (oxidizing sites), providing great scope as redox reagents. The process is heterogeneous because there are two active phases, solid and liquid. Semiconductors materials like TiO_2, ZnO, Fe_2O_3, CdS, ZnS, SnO_2 and WO_3 are commonly used in photocatalytic process for being physically and chemically stable and available at reasonable cost. Among them, titanium dioxide is one of the popular engineering materials in environmental applications and is the most effective photocatalytic materials. In addition to a large number of papers on its application to the purification of water, air, waste-water, ect. [116-126]. Photocatalytic activity of titanium oxide is predictable of large use in households [116], note that titanium is the ninth most abundant element constituting about 0.66% of the Earth's crust; it can be widely used for the water purification and air conditioning, self-cleaning in film coatings of furniture, walls, floors, window glasses, paints etc. and antibacterial functions.

Moreover, many studies have proven that titanium dioxide seems to be effective for the destruction of bacteria and viruses [117,118]. The inactivation of tumors [118,119], the mineralization of a large number of organic and inorganic compounds [120-123], and the reductive precipitation of heavy metals (for example, Pt^{4+}, Au^{3+}, Rh^{3+}, Cr^{4+}) from aqueous solutions [124,125] are further useful applications of TiO_2. Titanium dioxide has three crystal structures: anatase, rutile and brookite, however; the anatase type generally shows the highest photoactivity compared to the other types of titanium dioxide [127]. In the anatase form, the valance band (VB) and the conduction band (CB) energies are respectively +3.1 and -0.1 volts. Thus its band gap energy (Eg) is 3.2 eV. Irradiation of anatase TiO_2 with UV radiation ($\lambda < 385$ nm) greater than Eg causes promotion of an electron from VB to CB. This result in the formation of an electron-hole pairs (Eq. 1) separated between the VB and CB as shown in figure 1. This is a free electron (e^-) in the conduction band, and a hole (h^+) in the valence band.

$$TiO_2 + h\nu \longrightarrow TiO_2\,(e^-_{BC} + h^+_{BV}) \quad \text{Eq.1}$$

These reactive species either recombine or react with adsorbates at the TiO_2 surface. This is shown in Eq.2 to Eq.9 and in figure 1.

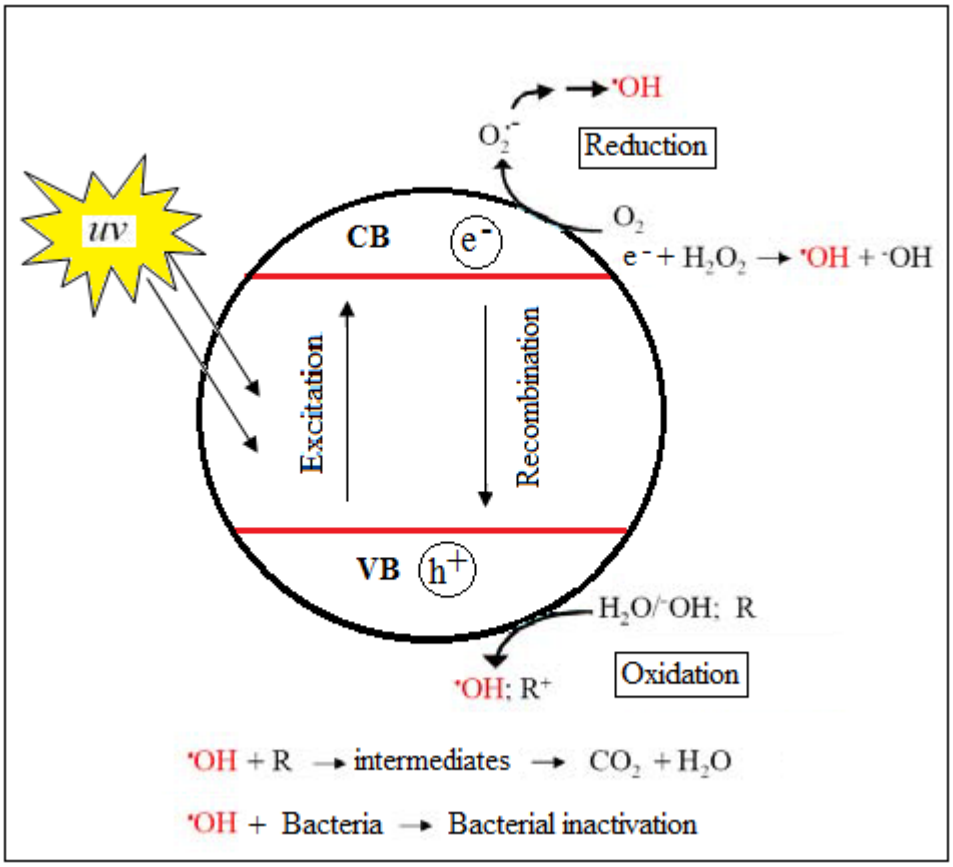

Figure (1): Photo-excitation processes in TiO2, leading to redox behavior.

The reactive species is the hydroxyl radical produced by redox reactions between photoexcited TiO_2 particles and adsorbed H_2O, adsorbed organic compounds, anions, molecular oxygen and from hydroxide groups on the catalyst surface. Three oxidation reactions have been observed: electron transfer from H_2O_{ads} (Eq.2), OH^- (Eq.3) and R_{ads} (Eq.4) adsorbed on the catalyst surface. Reactions 2 and 3 lead to OH^- adsorbed on the TiO_2 particles surfaces.

$$H_2O_{ads} + TiO_2\,(h^+) \longrightarrow TiO_2 + OH^{\bullet}_{ads} + H^+ \quad (2)$$

$$OH_{ads} + TiO_2\,(h^+) \longrightarrow TiO_2 + OH^{\bullet}_{ads} \quad (3)$$

$$R_{ads} + TiO_2(h^+) \longrightarrow TiO_2 + R^+ \quad (4)$$

On the other hand, the electrons react with electrons acceptors such as O_2 to form superoxide radicals [128]. Molecular oxygen is generally the acceptor species in an electron-transfer reaction with the photocatalyst CB (Eq.5). Superoxide anion and its protonated form subsequently yield hydrogen peroxide or peroxide anion (Eq.6.7.8).

$$TiO_2(e\text{-}) + O_2 \longrightarrow TiO_2 + O_2^{\bullet -} \quad (5)$$

$$O_2^{\bullet -} + H+ \longrightarrow HO_2^{\bullet} \quad (6)$$

$$O_2^{\bullet -} + HO_2^{\bullet} \longrightarrow OH^{\bullet} + O_2 + H_2O_2 \quad (7)$$

$$2HO_2^{\bullet} \longrightarrow O_2 + H_2O_2 \quad (8)$$

In the absence of acceptor and electron donor appropriate, there a recombination of hole/electron (very fast reaction of recombination) (Eq.9) [129].

$$TiO_2 + e_{BC}^- + h_{BV}^+ \longrightarrow TiO_2 \quad (9)$$

To enhance photocatalytic efficiency, there are several techniques: For example, doped semi-conductor by metals increases the range of absorption and in some cases decrease time of recombination [130]. It has been shown that hydrogen peroxide addition considerably enhances the photodegradation rate, most probably via Eq.10, where H_2O_2 is reduced by CB electrons, or by surface catalysed dismutation of H_2O_2 [131, 132]

$$H_2O_2 + e\text{-} + \longrightarrow OH^o + + OH^- \quad (10)$$

The hydroxyl radicals produced by the redox processes at the TiO_2 surface are highly reactive and non-selective oxidants. These attributes make the radical species potent biocides [133], with the ability to oxidize most organic and inorganic compounds. It has been found that the heterogeneous photocatalysis is influenced by several factors such as: catalyst concentration, initial compound concentration, temperature and pH, inorganic ions, light intensity, oxygen concentration, adsorption and reactor design.

4.10. Photocatalyst supports

The main role of a support is to improve the textural properties of the contact mass (increase porosity, surface area, etc.). In photocatalysis, the catalysts must be able to absorb light. Even when the latter is transparent to the incident light, the catalyst layer on the external surface absorbs the actinic light and therefore impedes penetration of the support [134]. According to Teichner et al. [135] a few hundred angstroms of TiO_2 are enough to absorb the incident light completely. Moreover, the modification of certain experimental parameters can also influence the photocatalytic reaction. Some factors influencing the photocatalytic activity are described below

4.2.a. Incident light intensity

To make the photocatalysis reaction possible, it is necessary to expose the catalyst to radiation energy sufficient to cause the transfer of electron from the valence band to the conduction band. Many studies have been shown that the efficiency of inactivation of bacteria and the rate disinfection increases when the light intensity increases [143,144]. Indeed, the results indicate that a higher light intensity produces a higher concentration of active oxygen species such as OH· and results in improved photocatalytic performance.

4.2.b. TiO_2 Loading

The mass of catalyst fixed on support plays an important role in the global efficiency of the photocalytic reaction. The initial photocatalytic reaction rate is directly proportional to the TiO_2 concentration [145], as a consequence of an increase in the number of illuminated particle surfaces, which produces a larger amount of reactive species. Yet, the catalyst mass to be immobilized on support is limited by the total photons absorption arising from the light source. Indeed, higher photocatalyst amounts result in lower reaction efficiency, due to screen effects [146]. The optimal TiO_2 amount must thus be determined for every experimental configuration [147]. In our case, the TiO_2 limit concentration was not reached since the photodegradation rate increase with increase in the mass of TiO_2.

4.2.c. Continuous Irradiation time

The effect of intermitent irradiation on disinfection processes in solution has been reported by Rincon et al., in aqueous solution [148]. This effect affects the rate of *E. coli* inactivation and the extent of this effect depends on the state of the reaction. Interruption of

the irradiation favors the bacterial self-defense mechanism or auto-repairing mechanism. In contrast, a short time of darkness after a long period of illumination does not affect the inactivation rate of bacteria. As the response towards the intermittency of the irradiation varies for each organism; it becomes crucial to determine for each microorganism the illumination time (intermittent or continuous) necessary to induce irreversible bacterial inactivation. This is relevant because the intermittency in the illumination could affect the post irradiation events to a different extent for each microorganism.

4.11. Fixation of Catalysts

Shaping of the catalyst is crucial and the support (substrate) must be adapted, titanium dioxide is available in the form of powder, granules, rods, or deposited on supports such as glass, ceramic, fiber of glass and textile or cellulose. On the other hand, Suspensions of TiO_2 as photocatalysts present two major obstacles when used in the form of suspension: (a) the separation of the semiconductor after the process a step that is expensive in terms of manpower, time and energy (centrifugation or other form of separation) and (b) the low quantum yield of the process hindering the overall efficiency. Thus, TiO_2 catalyst fixation on different supports has been investigated, i.e Nafion, Raschig glass rings, inorganic C-fabrics, synthetic fabrics, natural fabrics, textiles and thin plastic films [6,42,135-174].

Typically, it is assumed that suitable supports should present the following properties: (a) withstand reactive oxidative radicals attack during light, (b) maintain sufficient long-term catalytic stability, (c) preclude TiO_2 leaching during the light irradiation by favoring strong surface chemical-physical bonding with the TiO_2 particles without affecting their reactivity; (c) to have a high specific surface area, (d) allow the photocatalytic reaction to proceed with an acceptable kinetics, (e) to have good adsorption capability for the organic compounds to be degraded and (f) to allow reactor designs that facilitate the mass transfer processes (adsorption and diffusion behavior of target molecules).

From the coating point of view, the ideal situation is given by two basic conditions: a good adherence catalyst/ support, and no degradation of the catalyst activity by the attachment process. The first condition is essential, since the support/catalyst link should withstand strain derived from particle to particle and particle-fluid mechanical interactions in the reactor environment, in order to avoid detachment of catalyst particles from the support [139].

With regard the supports, there are two major types: (a) non-porous supports such as glasses, quartz and Pyrex principally, stainless steel. (b) Porous supports such as papers, fibers of glass and textile.

Powder anatase titania coating on a porous supports are commonly prepared by sol-gel [140]. Porous thick films consisting of fine particles of TiO_2 exhibited a high efficiency for photocatalytic decomposition [141]. This parameter is very important in destruction of microorganisms (inactivation bacterial) especially on textile coating by TiO_2. In many cases sol-gel prepared suspensions of TiO_2 fail to attach on textiles properly and for this reason we concentrated on the RF-plasma approach to fix with higher energy the TiO_2 films on textiles [142].

4.12. Choice of the preparation method

Two major ways have been explored to fix TiO_2 on different supports. The first is to fix the catalyst after being prepared in the form of suspension. The second consists in generating the catalyst *in-situ* by a sol-gel process.

4.4.a. Catalyst after synthesis

This method of preparation of supported catalyst is to fix the TiO_2 (generally commercial) directly on the support. The scheme for this method is described as following [134]:

- Thorough mixing or contact between the suspension of TiO_2 and support.
- Filtration, evaporation or separation solid-liquid
- washing and adhesion of the catalyst to support by heating
- flushing of the supported catalyst
- drying
- calcination at an appropriate temperature.

The electrostatic interactions are weak, for example, a study by Siffert and Metzger [142] deposit TiO_2 on cotton fiber and report the attractive forces of Van deer Waals for the catalyst-substrate interaction.

4.4.b. Generated catalyst in-situ

The *in-situ* formation of TiO_2 deposited on a surface by consist in the hydrolysis of $Ti(OH)_4$) and to pyrolysis (passage to TiO_2) (sol-gel process). The initial $TiCI_4$ is hydrolyzed in solution. The widely used alcoholate is titanium tetraisopropoxide (TTP) $Ti(O\text{-}i\text{-}C_3H_7)_4$, although titanium tetraisobutoxide (TTB) $Ti(O\text{-}i\text{-}C_4H_9)_4$ is used as the starting material [142].

4.13. Bacteria

The classification of microorganisms is based on the organization of cells, prokaryotes (bacteria) have a relatively simple structures characterized by the absence of a nucleus and organelles, in contrast, eukaryotic (fungi, algae, yeast) have a more advanced cell organization.

Bacteria with different membrane structures are Gram-negative or Gram positive. The structural differences lie in the organization of a key component of the membrane, peptidoglycan. Our study has been performed only for *Escherichia coli* (*E. coli*), Gram-negative, because it is generally accepted as a primary, universal target bacterium. In addition, it is the most common pathogenic bacteria family and a common indicator of fecal contamination.

The Gram negative bacteria, *E. coli* membrane is constituted of the outer membrane (cell wall), the periplasm, and the cytoplasmic membrane, figure (2). The outer membrane is chemically more complex and is in direct contact with the exterior. Here the peptidoglycan layer is thinner (2-6 nm thickness) and accounts for only 10 % of the cell wall. The outermost layer of Gram-negative bacteria, the outer membrane, is about 6 to 18 nm thick and accounts for the rest of the cell wall. The outer membrane consists of 50 % lipopolysaccharides, 35 % phospholipids, and 15 % lipoproteins. The periplasm contains many proteins, including hydrolytic enzymes and substrate transport enzymes, and the peptidoglycan layer. Together, the outer membrane and peptidoglycan provide mechanical protection to maintain the cell morphology.

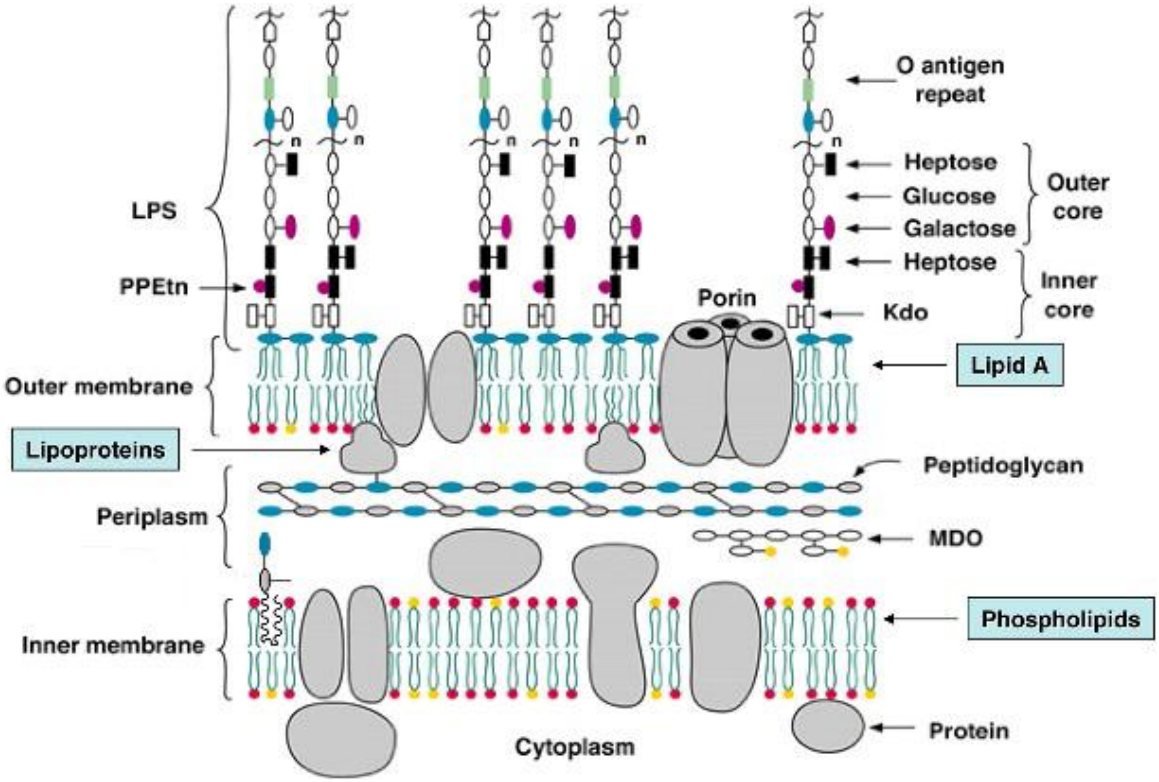

Figure (2): Schematic representation of the *E. coli* membrane LPS: lippolysaccharide; MDO: oligosaccharides; Kdo: acid3-deoxy-d-manno-oct-2-ulosonique; PPEtn: phosphoethanolamine [149].

The outer cell wall determines the antigenicity and sensitivity to phage infection, both in Gram positive and Gram-negative bacteria. In addition, the outer membrane of Gram-negative cells influences permeability of many moderate or large size molecules. At the bottom of the cell wall of bacteria, lies the cytoplasmic or plasma membrane required for the respiratory function involving electron transport and oxidative phosphorylation. The plasma membrane is about 8 nm in thickness and is composed of the phospholipid bilayer. When damaged it leads to bacteria death. This membrane has the property of selective permeability – allowing the passage of certain metabolites (porins) in and out of cells. In addition to maintaining osmotic equilibrium, the cytoplasmic membrane also contains the necessary enzymes for the synthesis, assembly and transport of cell wall components.

4.14. Bactericidal mode of titanium dioxide photocatalysis

The TiO_2 in suspension and fixed on a support under solar simulated irradiation has been reported by various studies [115-118, 150–152]. Matsunaga and co-workers demonstrated for

the first time that TiO_2 photocatalyst kills bacteria in water on light irradiation [153]. Through oxidation an oxidation mechanism involving $OH^{\bullet}$, $O_2^{\bullet-}$ and H_2O_2 production adsorbed on the TiO_2 surface.

Recently the three competing theories were evaluated showing some evidence for this process [117].

In the early studies a decrease in intracellular coenzyme A (CoA) in the TiO_2-treated cells was detected for various microorganisms [153, 154]. The oxidation of CoA that inhibited cell respiration and subsequently led to cell death was proposed as the first killing approach by Matsunaga et al [153]. This approach emphasized a direct contact between TiO_2 and target cells to ensure the direct oxidation of cell components.

The second theory was reported by Saito and coworkers [155]. It was found that the cell wall decomposition and disorder in cell permeability is observed by transmission electron microscopy (TEM). They demonstrated that TiO_2 photocatalytic reaction induced a "rapid" leakage of potassium ions and the "slow" leakage of intracellular species like DNA and proteins. Evidence for this can be found in work by Watts [156].

The third theory reports cell wall damage followed by cytoplasmic membrane damage [118, 117, 157]. Huang et al., proposed a more detailed mechanism for the bactericidal effect of TiO_2 photocatalytic reaction [117]. By probing *E .coli* with ortho-nitrophenol b-D-galactopyranoside (ONPG). An increase in cell wall permeability to ONPG, and leakage of large molecules from the interior of the cell was observed, supporting this approach. It was found that damage to the cell wall was non-lethal, whereas breach of the cytoplasmic membrane and leakage of the cytoplasm resulted in cell death. Lately, Lu et al [157] examined the effect of TiO_2 on *E. coli*, using AFM and measurement of K^+ ion leakage - AFM was able to demonstrate the decomposition of the cell wall, followed by the destruction of the cell membrane. It has been found that the loss of cell viability is consistent with the decomposition of the cell wall and the cell membrane and the leakage of intracellular species. A possible bactericidal mechanism was proposed for cells illuminated in the presence of TiO_2 thin films. The cell would be first decomposed, and subsequently the cell membrane would be destroyed, resulting in the increase in the permeability of cells, the leakage of intracellular molecules and the final death of cells.

According to Sunada [118] this process of *E. coli* photokilling on TiO_2 film proceeds as illustrated in figure (3).

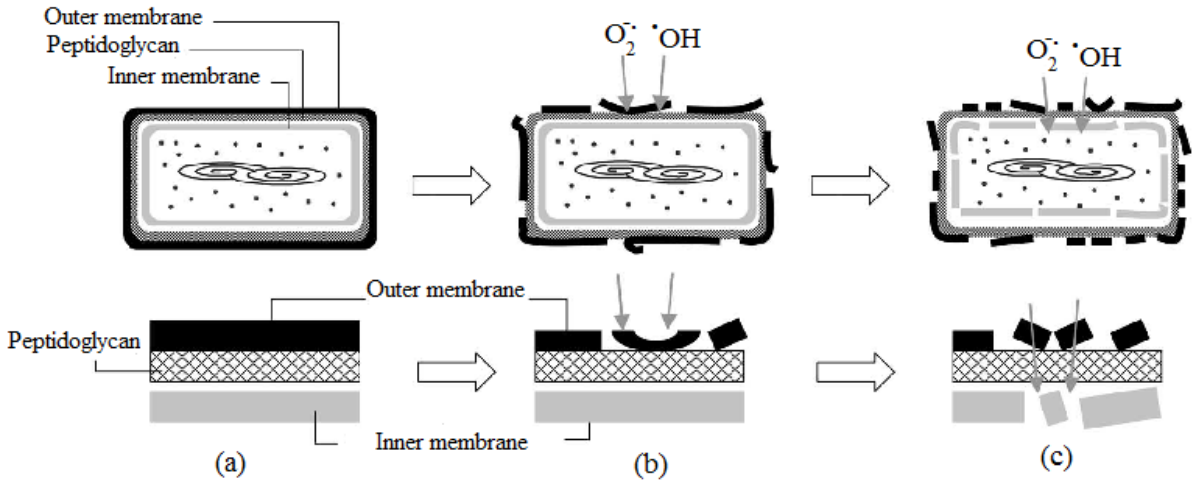

Figure (3): (a–c) Schematic illustration of the process of *E. coli* photokilling on TiO_2 film [118]

The initial reaction is a partial decomposition of the outer membrane by the reactive species produced by TiO_2 photocatalysis (b). During this process, cells were damaged but the cell wall is still viable. The partial decomposition of the membrane, however, changes the permeability to reactive species like $OH^{\bullet}$ and $O_2^{\bullet-}$ which allows them to easily reach the cytoplasmic membrane. Thus, the cytoplasmic membrane is attacked by reactive species, leading to the peroxidation of membrane lipid (c). As a result the structural and functional disorders of the cytoplasmic membrane due to lipid peroxidation lead to the loss of cell viability and cell death.

The effect of UV light by itself leads to photokiling due to the cytoplasma absorption of light of wavelength less than 330 nm by proteins and nucleic acids [158]. Indeed lamps of 254 nm are usually referred to as germicidal lamps. This was considered even in the first experiments by Matsunaga et al [153] where no microbiocidal action was observed in the absence of the photocatalyst. However, subsequent studies, such as that of Lu [157] show a small decrease in microbe viability with irradiation. In our study irradiation was carried out in the visible region, showing the same results according Matsunga [153].

4.15. Silver and silver-containing surfaces

The antibacterial activity of silver has been known for many years. Therefore, silver has been employed in the preparation of nanoparticles (NP's) supported or not to be used as

antimicrobial/bacterial agent [15,159,160]. Nano-structured nano-particulate silver presents physical and chemical properties that are highly convenient when incorporated into textiles and healing-pads. Ag-NP's provide large area-to-volume ratio and high reactivity being of practical use when supported on a variety of surfaces [8,10,16,17,161,162]. For this reason silver-based compounds have been used extensively in many bactericidal applications [163, 164]. For example, in the medical field, silver compounds have been used to treat burns and a variety of infections [165]. Therefore, nanosilver has emerged as one of the most commercialized nanomaterials, as wound dressings, textiles, water and air purification, self-sterilizing polymer films and bone implants [16, 166 – 168].

4.16. Interaction between nanoparticals of silver and Bacteria

The bactericidal effect especially of silver ions on micro-organisms is very well known 169]. However the mechanism of silver antibacterial action is poorly understood. Three mechanisms for the latter effect have been proposed: (a) interference with bacterial electron transport; (b) binding to the bacterial DNA of the Ag-ions. As a reaction against the denaturation effect of Ag/Ag-ions, DNA condenses losing their replication ability [165, 169] or ionic silver strongly interacts with thiol (- SH) groups of vital enzymes and inactivates them; and (c) interaction with cell wall membrane without entering the cell forming reversible sulfhydryl or histidyl complexes on the cell surface and preventing dehydro-oxygenation process [16].

The membrane of *E. coli* cell wall has positively charged groups, like amides, proteins and peptides, and negatively charged groups like carboxylates, polysaccharides, and phosphonates. In solution, the *E coli* cell wall membrane is always charged negatively between pH-9. The functional charged groups are unevenly distributed over the surface of the *E. coli* outer membrane and the negative groups predominate, thus conferring an overall negative charge to *E. coli* wall [151,170].

Chapter 3: EXPERIMENTAL TECHNIQUES

This chapter outlines the film deposition in detail, with an emphasis on sputtering, which is a widely used thin film deposition technique.

1. Materials and methods

The polyester fabrics have been chosen since it is flexible, resistant an low cost material. The polyester is an EMPA test cloth sample No. 407. It is a polyester Dacron polyethylene–terephthalate; type 54 spun, plain weave ISO 105-F04 used for color fastness determinations. The thermal limit of Dacron polyethylene–terephthalate was 110 ◦C for long-range operation and 140 ◦C for times ≤1 min. The thickness of the polyester was ±130 μm ±10% with average pore sizes of 20 μm and 10 μm (shown in figure 1).

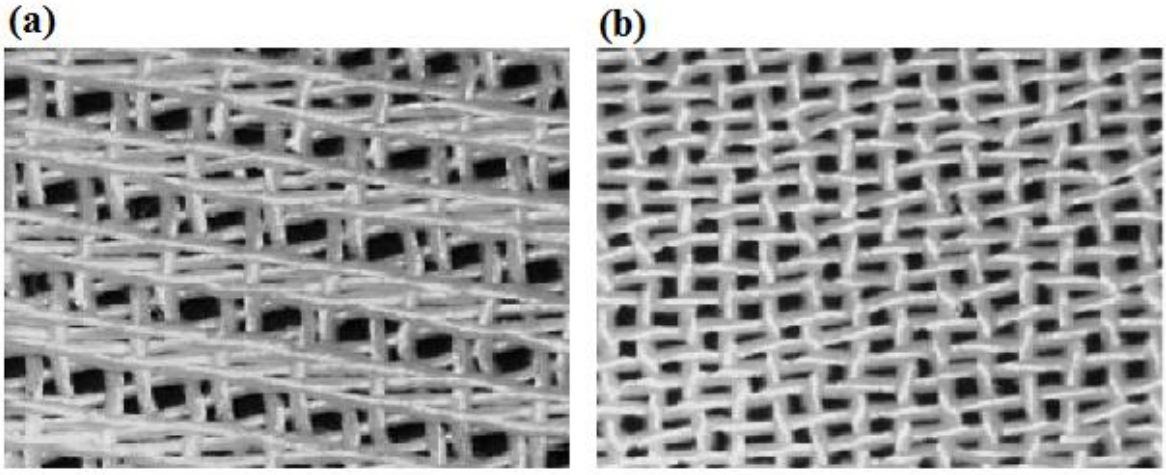

Figure (1): Images of polyester fabrics with the average pore sizes of (a) 20 μm and (b) 10 μm.

The samples of E. coli (E. coli K12) were obtained from the Deutsche Sammlung von Mikroorganismen und Zellkulturen GmbH (DSMZ) ATCC23716, Braunschweig, Germany to test the antibacterial activity of the polyester fabrics loading by different nanoparticles TiO_2 and Ag. The LB (Luria Betrani) and saline (NaCl/KCl) solutions used in bacterial growth contain the following ingredients:

LB: 10 g/L NaCl (ACROS ORGANIC) sodium chloride 99,5% for analysis, 10 g/L Tryptone (Bacto^{TM}) Pancreatic Digest of casein and 5 g/L Extract of meat (Merck. KGaA).

Saline solution (NaCl/KCl): 8 g/L NaCl (ACROS ORGANIC) sodium chloride 99.5% for analysis and 0.8 g/L KCl (Fluka, Ultra for molecular biology 99.5% AT).

Milli-Q water was used throughout for the preparation of aqueous solutions.

Characteristics of powder TiO_2 samples used to prepare TiO_2 coatings of polyester by wet techniques:

Catalyst	Supplier	Surface area (m^2/g)	Crystalline form	Crystallite size (nm)
P-25	Degussa	54	Anatase (80%), rutile (20%)	Anatase 24 ± 2, rutile 37 ± 3

1.1. Preparation of the samples

1.1.1. TiO_2 coated on Polyester

1.1.1.a. RF-plasma pretreatment of polyester textiles

In the first step, the polyester fabrics were cleaned by a nonionic detergent solution at 80 ◦C for 30 min to detach the stabilizers and impurities such as wax, fats, or additives. The polyester was then washed repeatedly with de-ionized water followed by immersion in ethanol, treated with ultrasonic for 5 min to remove organics and detergent residues and rinsed repeatedly with water and dried at 40 ◦C [7].

In the second step, the polyester fabric was pretreated in the vacuum cavity of the RF-plasma unit at 1 Torr as shown in figure (2) (Harrick Corp. UK). The experimental conditions used during the RF-plasma pretreatment were: plasma generator at 13.56 MHz, plasma power 100 W. The topmost polyester layers up to 2 nm were RF-plasma pretreated for 10 min, 20 min, 30 min, 60 min and 120 min. Figure (4) in chapter 4 shows that the ratio of the oxidized species to reduced functionalities remained constant for pretreatment times above 30 min. This is the reason for the use of the RF-pretreated plasma sample for 30 min throughout this study.

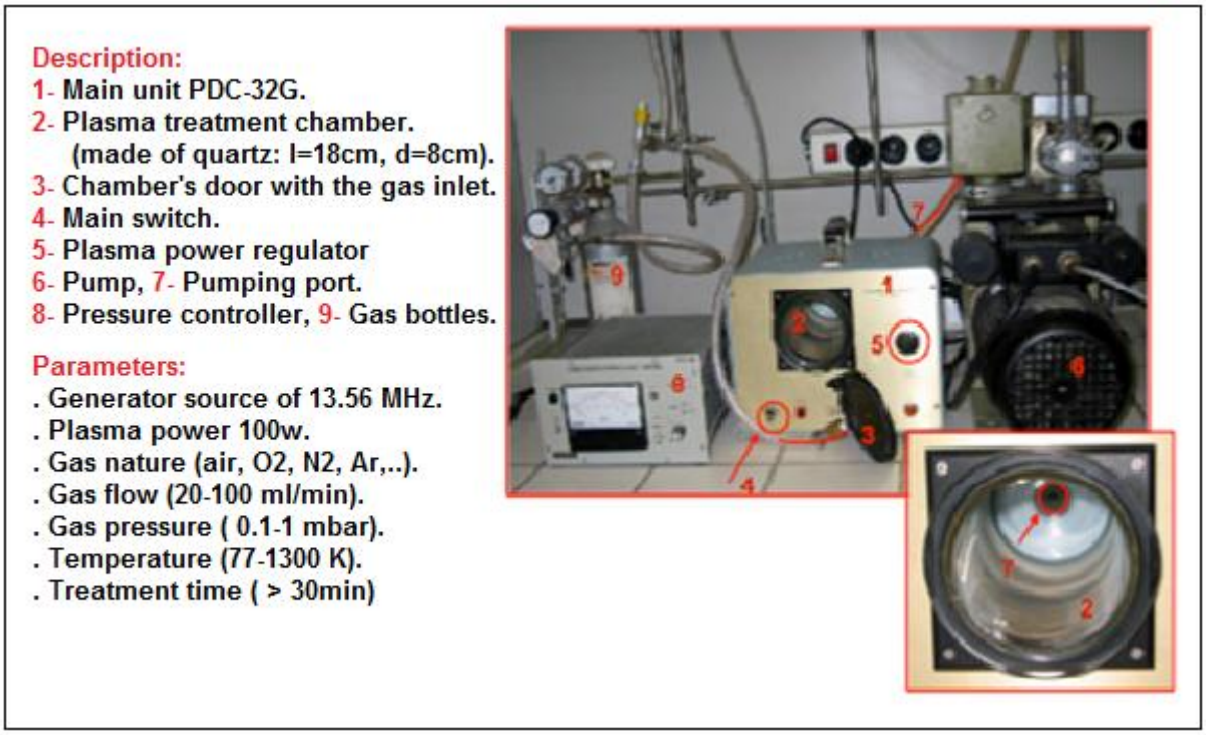

Figure (2): The RF-plasma unit (Harrick Corp) used for the pretreatment of polyester samples

During plasma pretreatment, the residual oxygen at 1 torr pressure was sufficient to modify the polyester surface due to the absorption cross-section of the oxygen O_2 for plasma. In fact, the active O^- species (single $^1O_2$, atomic O, anion-radical O^- and cation-radical O^+), induced by the plasma activation of the gas phase, react with the carbon textile of polyester surface [171] allowing introduced (or increasing) a variety functional groups like: C=O, – O – C= O, – COH, COOH, CH_2 – OH in the polyester surface. Figure (3) shows in a simplified way the functional groups introduced in the polyester fibers.

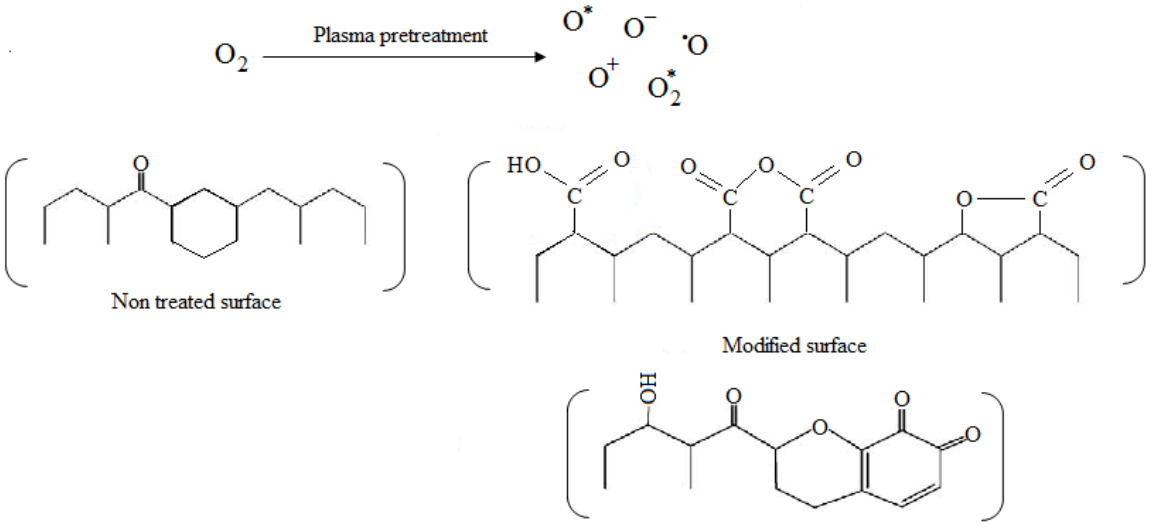

Figure (3): Diagram indicating the modification of polyester textiles induced by RF-plasma.

1.1.1.b. Loading of TiO_2 Degussa P25 suspensions on RF-pretreated polyester samples

The RF-plasma pretreated polyester samples 2 cm× 2 cm at different time (10, 20, 30. 60, 120) min were immersed in a sonicated TiO_2 Degussa P-25 suspension (5 g/L) and heated for 1 h at 75 ◦C (ultrasonic treatment for 30 min 150 W, 20 kHz). Then the samples were heated at 100 ◦C for 15 min. The loose bound TiO_2 was removed from the polyester samples by sonication and the sample washed thoroughly with water and dried at 60 ◦C [35,44]. Sometimes, this last step was repeated to deposit a second TiO_2 layer and obtain a more complete coverage of the polyester fabric. After the RF-pretreatment, the TiO_2 loading is immediately coated on the polyester since the functional groups and radicals introduced by RF-plasma on the polyester surface deactivate/hydrolyze rapidly due to the humidity and oxygen of the air [39, 40]. All samples then we called P0, P1, P2, P3, P6, P12.

P0: untreated polyester coated with TiO_2

P1: 10min RF-plasma treatment of polyester and subsequently coated with TiO_2

P2: 20min RF-plasma treatment of polyester and subsequently coated with TiO_2

P3: 30min RF-plasma treatment of polyester and subsequently coated with TiO_2

P6: 60min RF-plasma treatment of polyester and subsequently coated with TiO_2

P12: 120min RF-plasma treatment of polyester and subsequently coated with TiO_2

The nanocrystals of TiO_2 are bonded to the fabric with slightly positive Ti_4^+ of TiO_2 through electrostatic attraction surface with negative groups.

1.1.1.c. Detection of the OH-radical species on TiO_2 polyester using the fluorescence technique

The detection of the oxidative species (mainly OH-radicals) in the RF-plasma pretreated samples was carried out according to Hashimoto [172] and Girault [173]. We have applied fluorescence techniques to the detection of $OH^{\bullet}$ formed on a photo-illuminated TiO_2 surface using terephthalic acid which readily reacts with $OH^{\bullet}$ to produce the highly fluorescent 2-hydroxy-terephthalic acid , as shown below.

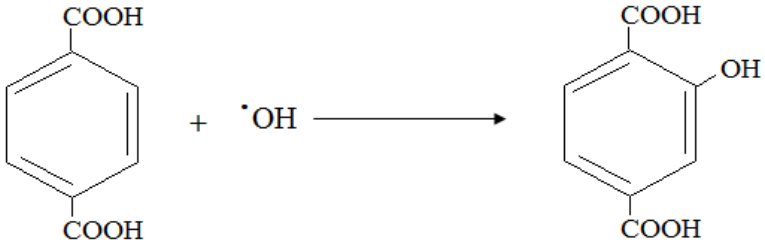

Terephthalic acid 99% was purchased from ACROSS and the NaOH 98% was from Sigma Aldrich. A sample of 4 cm^2 of TiO_2 coated fabric was immersed in a solution made of terephthalic acid at 0.4 mM dissolved in a 4 mM NaOH solution as shown in figure (4).

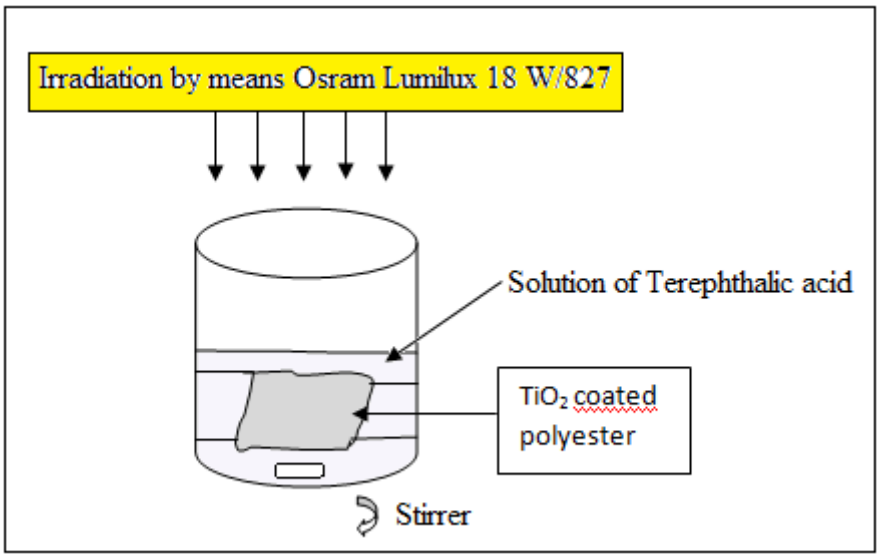

Figure (4): Schematic illustration of the illumination system.

After each irradiation by means Osram Lumilux 18 W/827 actinic, the solution was transferred in a quartz cell and the fluorescence spectra of 2-hydroxyterephthalic acid generated by the reaction of terephthalic acid with the $OH^{\bullet}$ containing compound were measured on a Perkin Elmer LS-50B fluorescence spectrometer. The spectra were recorded between 300 and 600 nm (scan rate: 100 nm/min) under an excitation at 315 nm. The excitation and emission slits were fixed at 5 nm.

1.1.2. Ag and Zr-Ag-N Sputtering films on polyester

Thin films of Ag-polyester were deposited by DCMS, DCMSP, and HIPIMS. The Zr-Ag-N-polyester films were deposited by DC reactive pulsed magnetron sputtering.

1.1.2.a. Magnetron sputtered Ag-deposition on polyester

The deposition machine used in DCMS, DCMSP and also DCMSP reactive is shown in figure (5). The deposition chamber is a stainless cylindrical and equipped with two confocal targets of 5 cm in diameter. The distance between the targets and the substrate

(polyester) was 10 cm. The targets were used either to sputter by DCMS and DCMSP which optimizing the voltage, current and power.

In the sputtering chamber the Ag-cathode plate was bombarded by Ar-ions generated in the glow discharge plasma situated in front of the Ag-target. The plasma working pressure was 0.4 Pa, and the diameter of the 99.99% pure Ag target was 5 cm and received from K. Lesker Ltd. UK. The deposition currents used were of 0.05 Amp and 0.03 Amp and a current of 0.3 Amp needed a bias voltage of −400 V.

DC pulsed was operated at 50 kHz with 15% reversed voltage. A negative voltage was applied of -430 V and then the voltage was switched to + 65 V (15% of - 430 V) to accelerate the Ag-particles toward the substrate. During DCMS pulsed, continuous pulses of 10 microseconds were applied, but with time the target gets overcharged and when this occurs, the unit tries three times to clear the charging arc with additional three pulses (see Fig. 6) before the power supply shuts down for 7 ms and turns on automatically after this recovery time. Figure (6) shows schematically these three additional pulses within 50 μs. This sputtering mode is neither: a) unipolar pulsed sputtering, where the target voltage is pulsed between the normal operating voltage and ground nor a b) bipolar pulsed sputtering where the target voltage is reversed and becomes more positive during the pulse-off period and as shown in figure (7) chapter 2, the DCMS pulsed operation becomes bipolar asymmetric. In the case of 0.3 Amp DCMS pulsed, the voltage applied of - 430 V on the 5 cm diameter Ag-cathode leads to a power density of about 6.6W/cm^2 and provides current densities up to15.3 mA/cm^2.

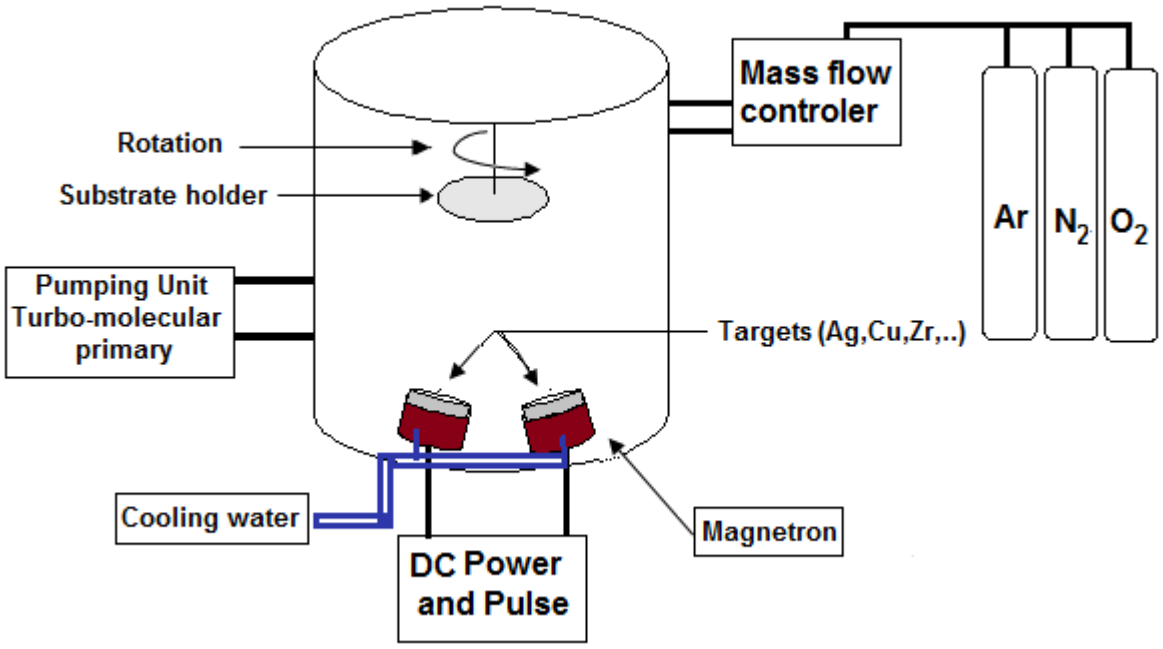

Figure (5): Schematic description of the sputtering machine used for the film deposition.

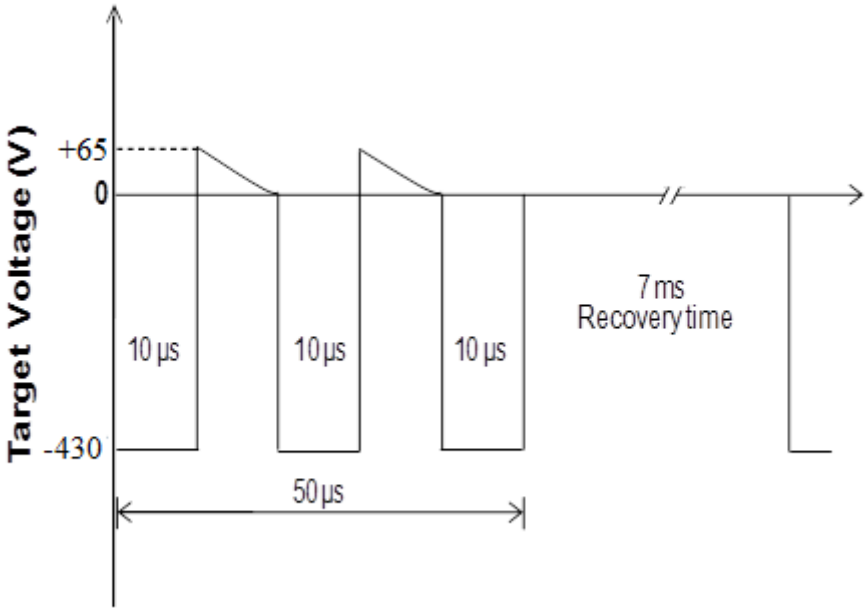

Figure (6): Asymmetric bipolar DC-magnetron pulse. For other details see text

HIPIMS deposition of Ag was carried out in a CMS-18 Vacuum system from Kurt Lesker Ltd. evacuated to 10^{-2} Pa by a turbomolecular pump [21]. Figure (7) shows a schematic of the HIPIMS chamber. The mass spectrometry measurements were carried out in a mass spectrometer PSM003 (Hiden Analytical Ltd.) to determine quantitatively the composition of the ions in the HIPIMS plasma Ar-atmosphere [174]. The HIPIMS unit was operated at 100 Hz with pulses of 100 microseconds separated by 10 μs. The substrate was unbiased, and placed on an isolated holder, thus assuming the floating potential of the plasma. The substrate-to-target distance was 15 cm. The applied power was varied between 1 and 5 amps and no glow-to-arc transition was detected during the plasma deposition. The HIPIMS power at 5 amps was of 260mA/cm^2. The HIPIMS short pulses avoid a glow-to-arc transition during plasma particle deposition [22]. The pressure was the same as the one used in the DCMS and DCMSP chamber and the substrate was not heated.

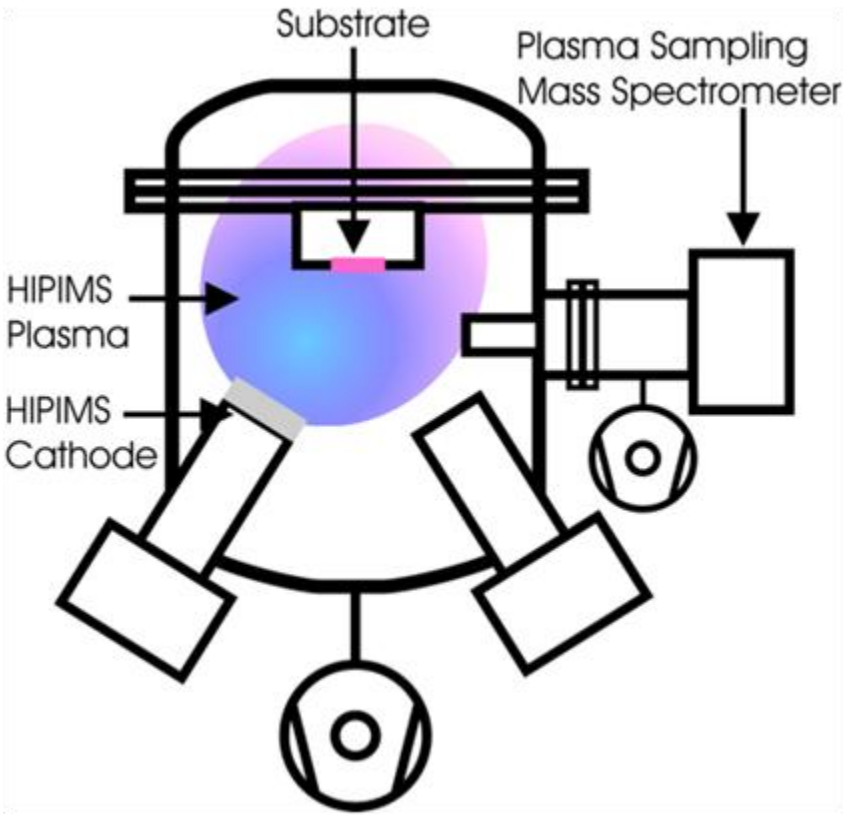

Figure (7): Schematic of the HIPIMS setup, the cathode used was Ag and the substrate polyester

1.1.2.b. Zr-Ag-N sputtering on polyester by DCMSP reactive

Zr-Ag-N deposited on polyester fibers by DCMSP (figure 5) using simultaneously targets of Ag (99.99 at.%) and Zr (99.98 at.%) in confocal configuration. The distance between the targets and the polyester substrate was 10 cm and the diameter of the targets was 5 cm. The residual pressure in the sputtering chamber was in the 5×10^{-5} Pa range. The working pressure (Ar + N_2) was 0.5 Pa and the reactive nitrogen partial pressure was fixed at 10% to obtain cubic ZrN. The deposition was performed at room temperature. The DCMSP Ag sputtering used two currents at 0.05 Amp (20 W) and 0.3 Amp (270 W) in order to change the Ag-content in the Zr-Ag-N film. The DCMSP was operated at 50 kHz with 15% reversed voltage. The current on the Zr target fixed was 290 mA (100 W) whereas that of the Ag target was varied in the range 50–300 mA (20–270 W).

1.2. Evaluation of the bacterial inactivation of Escherichia coli and irradiation procedures

1.2.a. Bacterial growth medium

The bacterial was inoculated in the LB (5 ml) solution and grown during the day (8h) in the incubator (HT INFORS AG) at 37 ^{0}C by constant agitation (180 rpm) under aerobic conditions. Aliquots of this culture (250 µl) were inoculated into fresh medium LB (25 ml) and incubated overnight (15 h) aerobically at 37 ^{0}C under agitation (180 rpm). The bacterial growth was monitored at 600 nm by optical means. At an exponential growth phase of 0.8 (as detected at λ= 600nm), bacteria cells were harvested by centrifugation at 5000 rpm for 10 min at 4 ^{0}C (type of centrifuge: HERMLE. Z 323 K). The bacterial pellet was subsequently washed three times with the saline solution (NaCl/KCl; pH=6-7). Cell suspensions were inoculated in the saline solution in a Pyrex glass bottle of 50 ml to the required cell density corresponding to 10^6 to 10^7 colony forming units per milliliter (CFU/ml). Serial dilutions were prepared if necessary in the saline solution and 100 µl samples were plated on Plate-Count-Agar (PCA, Merck, Germany). Plates were incubated at 37 ^{0}C for 48 h before the bacterial counting was carried out. The detection limit for the procedure employed was 10 CFU/ml.

1.2.b. Evaluation of the bacterial inactivation

The polyester fabrics were sterilized by autoclaving at 121°C for 2 h. 20 µL aliquot of culture with an initial concentration of $3{,}8x10^{6}$ CFU mL^{-1} in NaCl/KCl was placed on each coated and uncoated (control) polyester fabric. The samples were placed on Petri dish provided with a lid to prevent evaporation as shown in figure (5). After each determination, the fabric was transferred into a sterile 2 mL Eppendorf tube containing 1 mL autoclaved NaCl/KCl saline solution. The cell suspensions were diluted with a saline solution with 0.75% NaCl and KCl 0.08% to allow the storage of the bacteria without osmotic stress. This solution was subsequently mixed thoroughly using a Vortex for 3 min. Serial dilutions were made in NaCl/KCl solution. A 100-microliter sample of each dilution was pipetted onto a nutrient agar plate and then spread over the surface of the plate using standard plate method. Agar plates were incubated, lid down, at 37 °C for 24 h before colonies were counted. The bacterial data reported were replicated three times.

To verify that no re-growth of E. coli occurs after the total inactivation observed in the first disinfection cycle, the samples were incubated for 24 h at 37 ◦C. Replica samples were incubated at 37 ◦C for 24 h at the end of each bacterial inactivation cycle. No bacterial re-growth was observed.

The irradiation of the TiO_2-polyester samples was carried out in a cavity provided with tubular Osram Lumilux 18 W/827 actinic light source as shown in figure (8). These lamps have a visible emission spectrum between 310 and 720 nm with an integral output of 1.1 mW/cm^2 resembling the light distribution found in solar irradiation see figure (9).

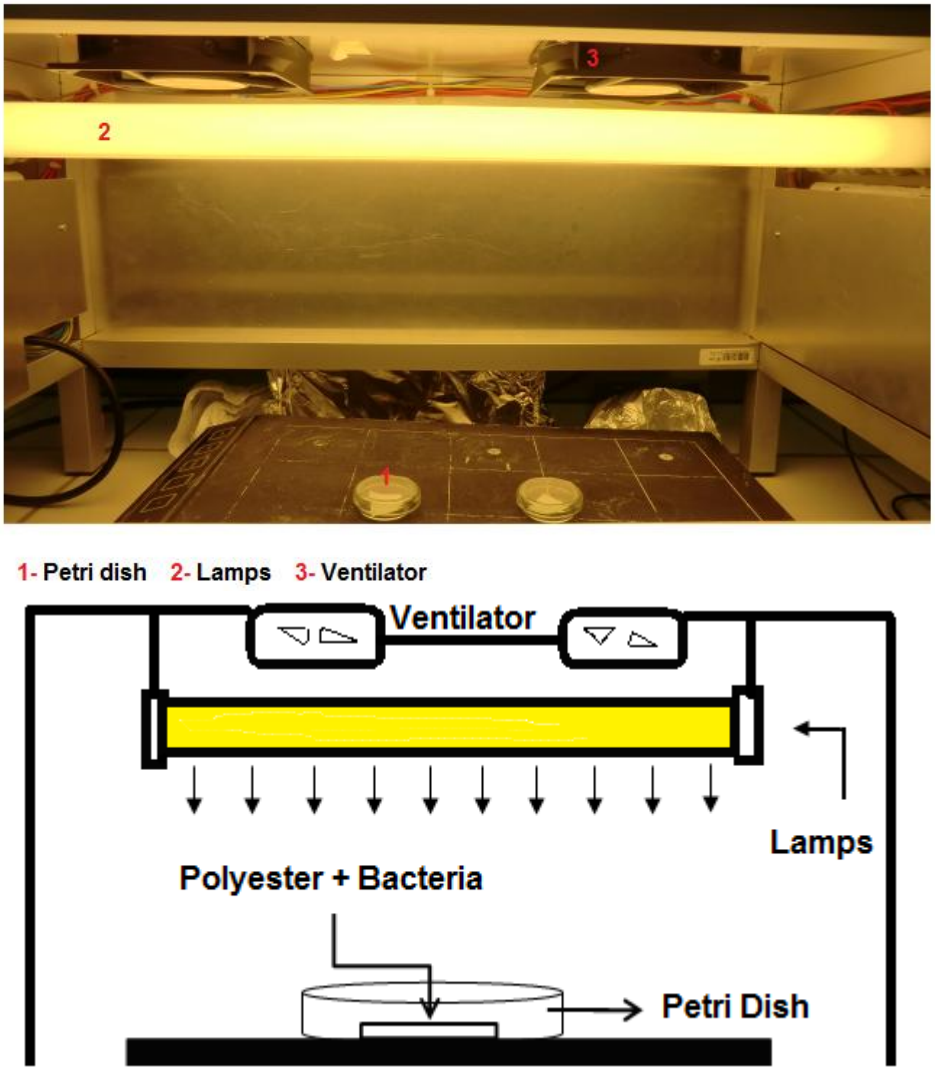

Figure (8): Scheme of the experimental to monitor the bacterial inactivation

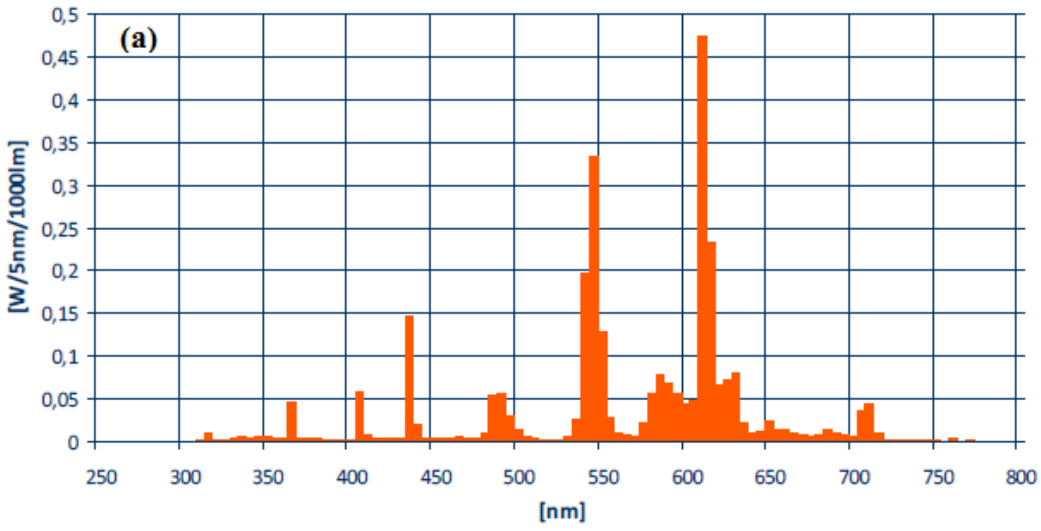

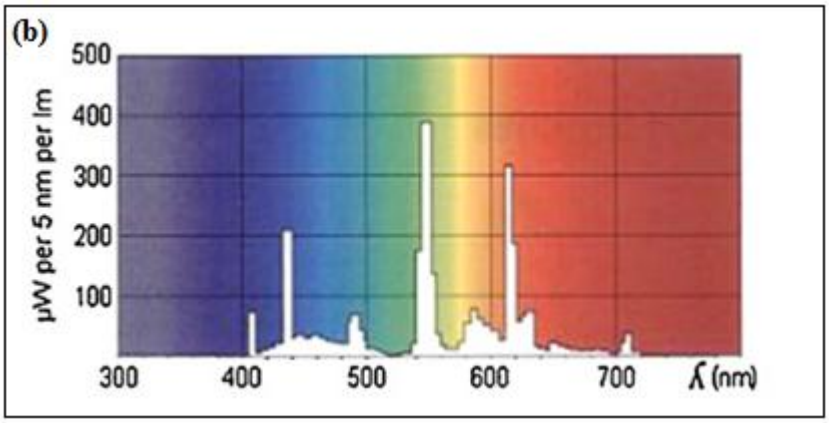

Figure (9): Spectral distribution of the light of the actinic lamp Lumilux Osram (400-720 nm) **(a):** 18W/827 (1.1 mW/cm^2), **(b):** L18W/840 (1.25 mW/cm^2)

A propos the samples of polyester prepared by Ag (DCMS, DCMSP and HIPIMS) in chapter 2, all the experiments were carried out in the dark.

2. Characterization techniques.

2.1. X-ray fluorescence determination of the Ti weight percentage and Ag-content on polyester samples (XRF)

The XRF method depends on fundamental principles that are common to several other instrumental methods involving interactions between electron beams and x-rays with samples, including: X-ray spectroscopy (e.g., SEM - EDS), X-ray diffraction (XRD), and wavelength dispersive spectroscopy (microprobe WDS). The resulting fluorescent X-rays can be used to detect the abundances of elements that are present in the sample.

The Ti-content and Ag-content on the polyester were evaluated by X-ray fluorescence (XRF) since it emits an X-ray of a certain wavelength associated with its particular atomic number in the PANalytical PW2400 spectrometer.

2.2. Diffuse reflectance UV–vis spectroscopy (DRS)

Diffuse reflectance spectroscopy was carried out using a Perkin Elmer Lambda 900 UV–vis-NIR spectrometer provided for with a PELA-1000 accessory within the wavelength range of 200–800 nm and a resolution of one nm. The Kubelka–Munk relations [175] were used to transform the reflectance data into absorption spectra. A Kodak analytical standard white reflectance coating was used as reference. Diffuse reflectance can be related to the absorbance by the K/S ratio using the Kubelka–Munk relations (F(R1)) (Eq. (1)), where the

scattering is noted as S and reflectance is noted as R. The reflectance relates to the absorption coefficient a (K/S) and this is proportional to absorbance K (Eq. (1)).

$$\frac{K}{S} = \frac{(1-R_\infty)^2}{2R_\infty} = F(R_\infty) \quad (1)$$

2.3. Transmission electron microscopy (TEM)

In transmission electron microscopy (TEM), electrons from the emission gun are transmitted through very thin sample (electron transparent), and generate an image of the internal structure of the sample. The resulting image displays structural details in the order of fractions of a nanometer [176]. A Philips CM-12 (field emission gun, 300 kV, 0.17 nm resolution) microscope at 120 kV was used to visualize the TiO_2 coating on the polyester and to measure the particles size of the Ag-nanoparticles. The textiles were embedded in epoxy resin 45359 Fluka and the fabrics were cross-sectioned with an ultramicrotome (Ultracut E) at a knife angle at 35◦. Images were taken in the Bright Field (BF) mode.

2.4. Atomic Force Microscopy

Atomic force microscopy (AFM) or scanning force microscopy (SFM) is a very high-resolution, in the nanometer range. The AFM employs an electrically conducting tip close enough to the surface of a conducting sample and a bias voltage is applied (typically between 1 mV and 4 V) to the tip a tunneling current of typically 0.1 to 10 nA can be generated. If this current is kept constant (constant current mode) the tip to surface distance must be unchanged. This allows to the detection of the topography image as the tip is scanned over the sample surface.

AFM observations in this work were done using an UHV VT SPM (Omicron) working in noncontact mode (needle sensor), with a tungsten tip and a lateral resolution of about 0.1 nm in the constant current mode.

.

2.5. Profilometry

The nominal calibration of the Ag-film thickness on the polyester was carried out on Si-wafers since this support do not present surface porosity. A profilometer (alpha-step 500 KLA Tencor Corporation) was used for the measurement of the thickness of the deposited film. The precision of the thickness measurement is within ± 5 nm. Due to the thickness inhomogeneity the accuracy of the considered value of the thickness is 10%.

2.6. X-ray diffraction (XRD)

X-ray diffraction (XRD) was used to determine the crystalline structure of the films (TiO_2-polyester and Ag-Polyester). XRD was done on a X'Pert diffractometer of the Philips, Delft, Netherland instrument using monochromatic radiation (Cu Kα) (0.6 Angström). Both configurations, grazing incidence (GI) at $\Omega = 4°$ and Bragg Brentano ($\theta/2\theta$) were used. For the first configuration GI the diffracting planes are at an angle of $1/2\ (2\theta) - \Omega$ to the normal of the surface film, whereas in the second $\theta/2\theta$ the diffracting planes are parallel to the surface film.

Using Jade 6.0 computer software the XRD patterns were fitted in order to obtain the peak position, integral breadth and the integrated peak surface (peak intensity). The width of the peak is an integral convolution of the instrumental broadening, of the broadening caused by the finite size of the crystallites and that from the random strain of the lattice. The instrumental width was removed automatically using an XRD pattern of a reference sample, powder of Y_2O_3, recorded in the suitable configuration, GI or $\theta/2\theta$.

2.7. Contact angle measurements

Water droplet contact angle is a measure of surface energy (hydrophilicity or hydrophobicity) [177]. Very smooth surfaces are, typically, harder to colonise by microbes than rough surfaces, since surface roughness is required to obtain very high contact angles.
The contact angle is defined as the angle between the solid surface and the tangent of the liquid vapor interface a sessile drop [178].

Contact angles of the polyester samples as a function of the RF-plasma pretreatment time and sputtered Ag-polyester as a function of sputtering time were measured by means of a DataPhysics OCA 35 instrument following the Sessile's method for the analysis of water droplets.

2.8. Inductively coupled plasma sector field mass spectrometry (ICPSMS)

The FinniganTM ICPS used was equipped with a double focusing reverse geometry mass spectrometer with an extremely low background signal and a high ion-transmission coefficient. The spectral signal resolution was $1.2x10^5$ cps/ppb and a detection limit of 0.2 ng/L.

2.9. X-ray photoelectron spectroscopy

In X-ray photoelectron spectroscopy (XPS) technique, an incident X-ray on a sample leads to the ejection of a core level electron. The kinetic energy KE of the photo-emitted core electron is

$$KE = h\nu - BE + \varphi$$

Where hν is the energy of the exciting radiation, BE is the binding energy of the emitted electron in the solid, and φ is the spectrometer work function [179].

In this work, An AXIS NOVA photoelectron spectrometer (Kratos Ana-lytical, Manchester, UK) equipped with monochromatic AlK _ (hν = 1486.6 eV) anode was used during the study. The electro-static charge effects on the samples were compensated by means of the low-energy electron source working in combination with a magnetic immersion lens. The carbon C1s line with position at 284.6 eV was used as a reference to correct the charging effect. The quantitative surface atomic concentration of some elements was determined from peak areas using sensitivity factors [180]. The spectrum background was subtracted according to Shirley [181]. The relative intensities of the XPS peaks depend on the spatial distribution of the emitting atoms inside the solid. Electrons with a defined energy E_o loose energy due to inelastic scattering during the XPS analysis. This distorts the peak shape, height, intensity and the background of the XPS spectrum. Any XPS spectrum can be corrected for inelastic scattering if the depth profile, the inelastic mean free path and the inelastic cross section are known. For the elements reported in this study Ti, Ag, C, O, the inelastic cross section and the sensitivity factors allow to calculate the inelastic background, since the in-depth emitter profile is known [180,181]. For each element the Ti, Ag, C, O, the background subtraction and the intrinsic element peak can be obtained and used as reference for the quantitative analysis of the element XPS spectrum. The XPS spectra for the Ag and Ti-species were analyzed by means of spectra deconvolution software (CasaXPS-Vision 2, Kratos Ana-lytical UK). The deconvolution of the XPS peaks was carried out by Gaussian–Lorentzian fitting of the peak shapes.

Chapter 4: RF-plasma pretreatment of polyester surfaces leading to TiO_2 coatings with improved optical absorption and OH-radical production

1. Surface chemistry of polyester.

A scan XPS spectrum of untreated polyester fabric is shown in figure (1a) and it essentially contains C1s and O1s peaks. The O1s peak of polyester after plasma treatment (30 min) was higher than that of untreated one and the N1s peak appeared in figure (2b). According to Table 1, the content of C1s decreases while the content of O1s increases and the O/C ratio on the surface of plasma for the pretreated polyester increased compared to the untreated sample. These results suggest that oxygen was incorporated into the surface of polyester during the pretreatment. Polar groups in polyester surface may be the main reason for the increase in hydrophilicity for pretreated samples as it is shown later by contact angle measurements below. Table 1 also shows that a very small increase in N/C atomic ratio is found. This suggests that nitrogen-containing groups are introduced in the sample surface after plasma pretreatment.

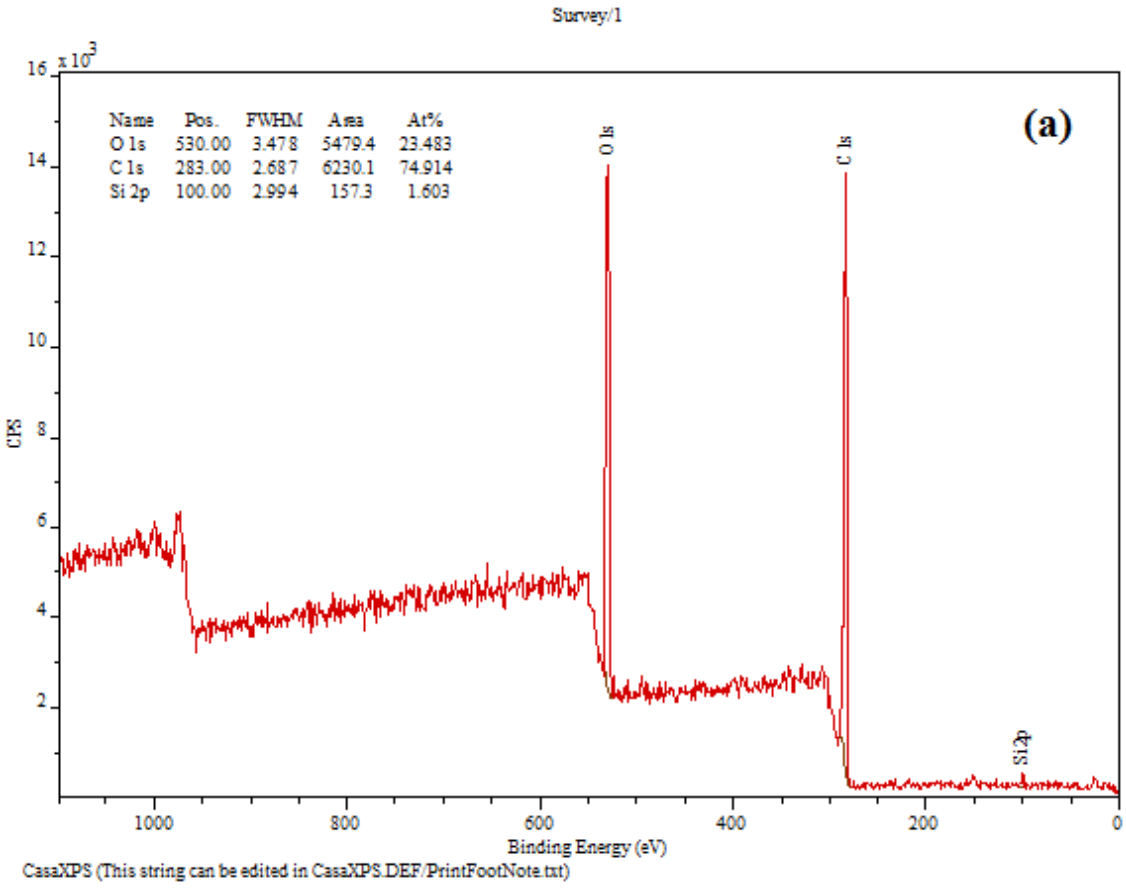

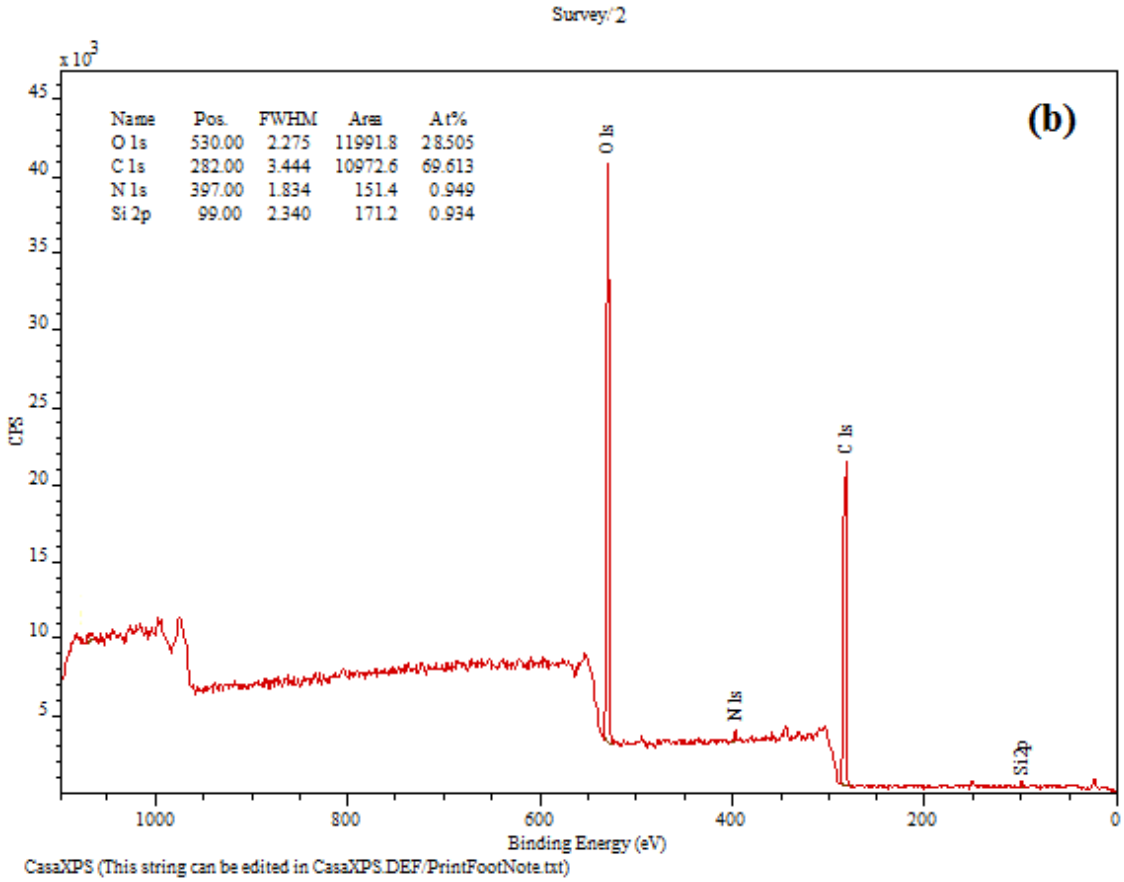

Figure (1): XPS spectra in the binding energy range 0–1100 eV of **(a)** untreated polyester and **(b)** plasma-treated polyester fabrics (30 min).

Table 1: Atomic percentage of chemical composition and atomic ratios of polyester fabrics determined by XPS

Samples	Elements	% At Conc	Atomic ratios	
			O/C	N/C
untreated	C1s	74.914	0.313	0
	O1s	23.483		
Plasma treated (30 min)	C1s	69.613	0.41	0.014
	O1s	28.505		

2. Effect of the RF-pretreatment time of polyester samples on the amount of surface oxidized functionalities detected by XPS.

XPS deconvolution analysis of the C1s and O1s peaks before and after plasma treatment were performed. Figure (2a) shows the XPS spectra for the untreated C1s signal region. As well documented in literatures [185–187], the peak of the untreated polyester is deconvoluted into components: the major peak at 284.9 eV assigned to the CH_2-functionality, and the peaks at 286.4 eV and 289.1 eV assigned the C-O and COO^- functionalities respectively.

The content of the C-species is shown in Table 2, figure (2b) after 30 min RF-plasma pretreatment. The peaks for C-O and COO^- increase for the pretreated RF-plasma samples, compared to the untreated sample and the number of CH_2- groups decreased. This indicates that some CH_2- groups have been oxidized to COOH or COH [188].

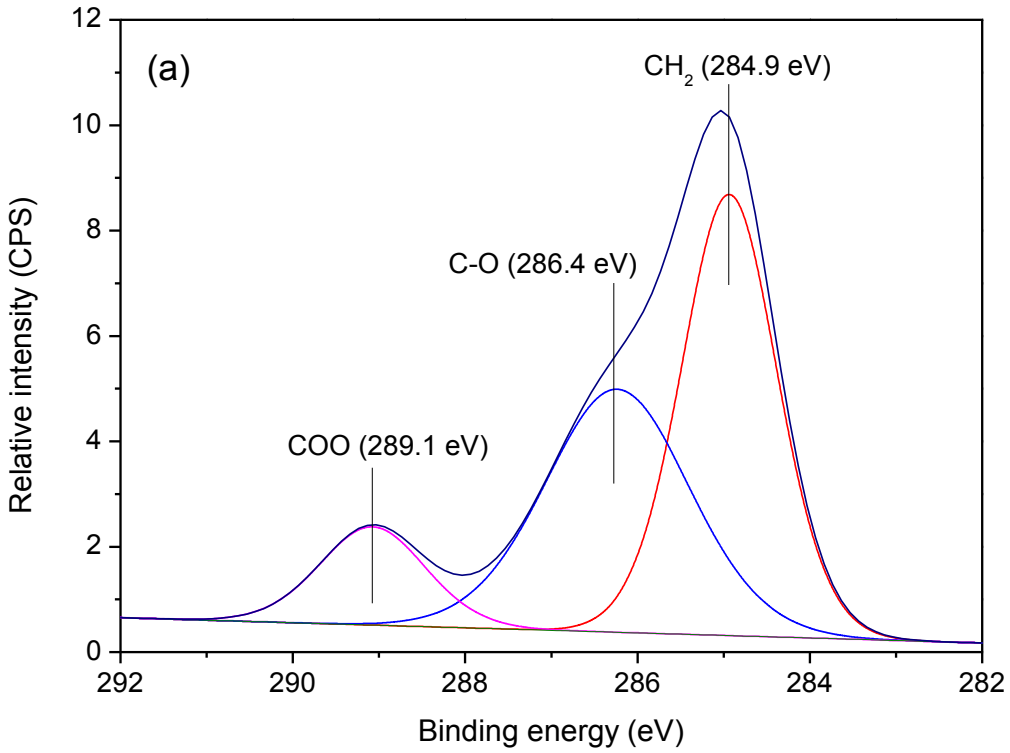

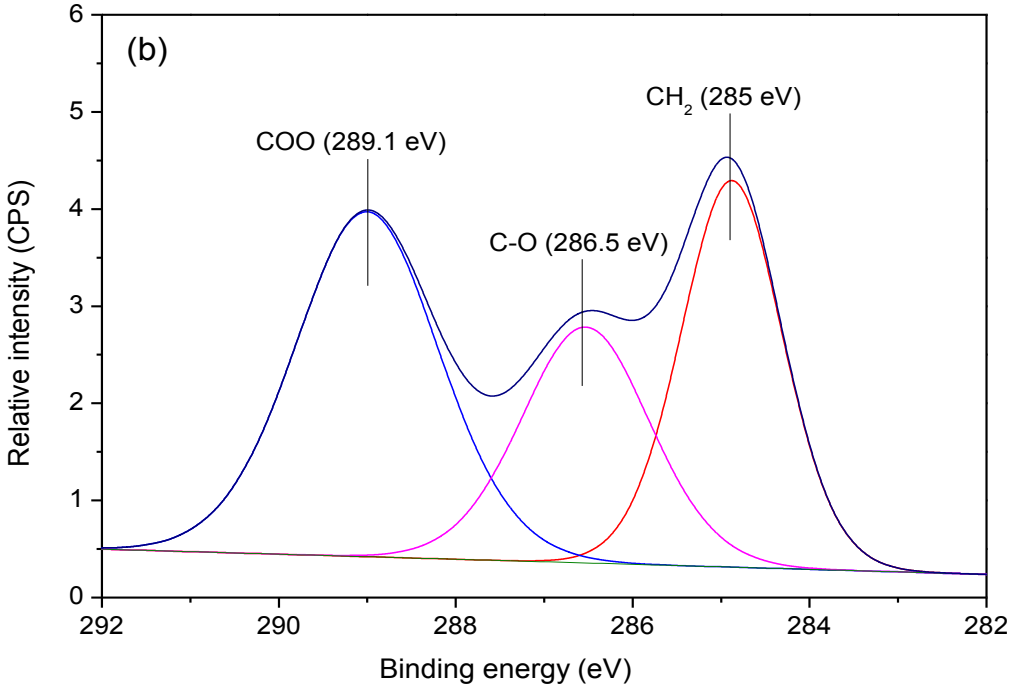

Figure (2): XPS C1s spectra of **(a)** untreated polyester and **(b)** RF-plasma pretreated polyester for 30 min.

Table 2: Percent peak area of XPS C1s signal of RF- plasma pretreated and untreated polyester

Bending Energy (eV)	Untreated (%)	Plasma treated (30 min)(%)	Functional groups
284.9	48.8	31.9	CH_2
286.5	30.3	38.5	C-O
289.1	20.9	29.6	O-C=O

Figure (3) shows the XPS spectra collected from: (a) untreated and (b) RF-plasma pretreated samples for 30 min in the O1s XPS spectral region. The two O1s peaks are fitted with two main peaks at energies of 533.6 eV and 532.0 eV. In addition, the O1s peak from the untreated sample shows a shoulder on the low energy side at 530.5 eV [51] and the O1s peak from the treated sample shows a shoulder on at 535.8 eV. The peak at 532.0 eV corresponds

to oxygen atoms attached to C- in the form of COO^- groups, while the peak at 533.5 eV corresponds to the oxygen atoms attached singly to carbon. The increased intensity of the areas under the peak at 533.5 eV and at 532 eV shows that COH increases for the RF-plasma pretreated samples. A concomitant increase of H_2O/OH_{surf} molecules on the surface was observed (data not shown) due to the high surface energy of the film in the RF-pretreated samples.

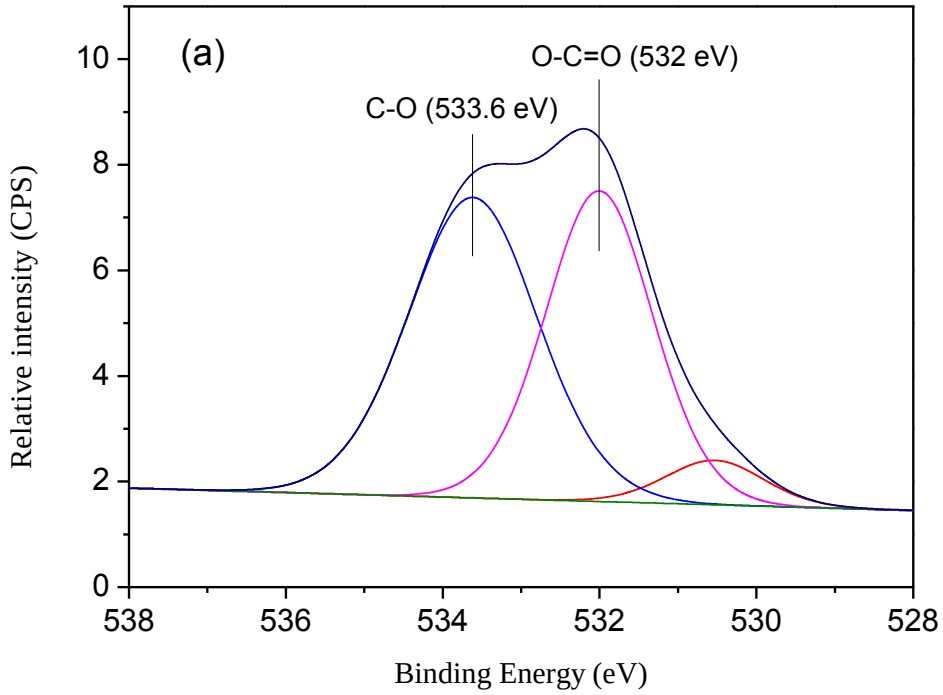

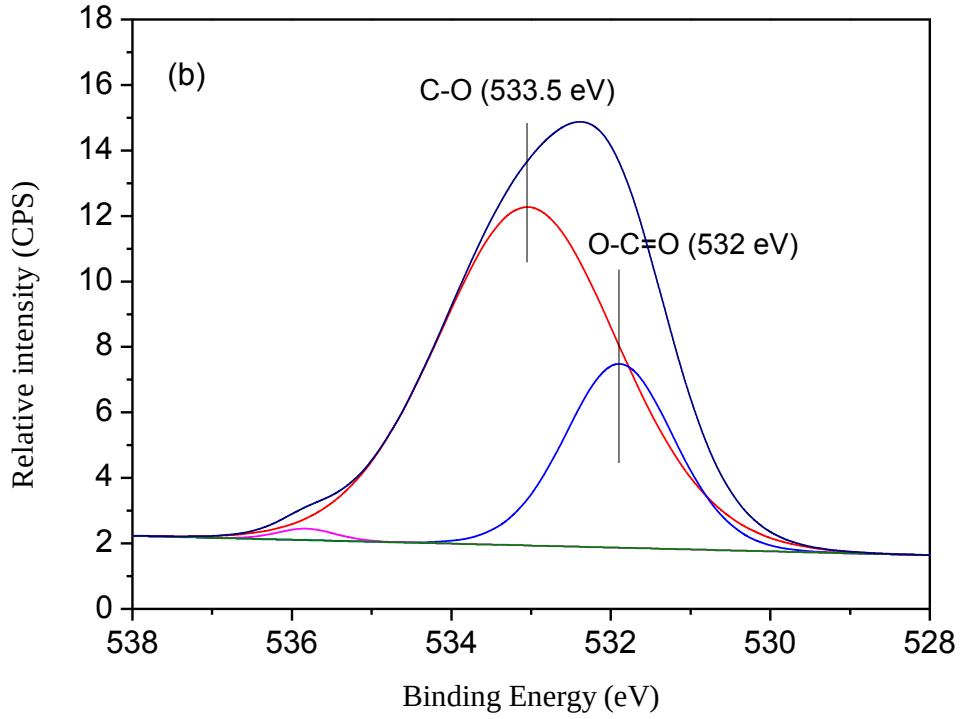

Figure (3): XPS O1s spectra of **(a)** untreated polyester and **(b)** RF-plasma pretreated polyester for 30 min.

Figure (4) shows the effect of RF-plasma pretreatment time on polyester for 10 min, 20 min, 30 min, 60 min and 120 min. The changes in the concentration of the functional groups C-OH and O=C-OH (oxidative species) and the ratio to the $-CH_2$ (reductive species) species established in each case and the ratio was plotted in Figure (4). The deconvoluted peaks centered at BE of 286.5 and 289.1 eV were ascribed respectively to the C-OH and O=C-OH functional groups according to the BE reference values found in the literature for these functionalities [7, 41, 44, 51, 180, 182-184]. The binding energy (BE) at 285.0 eV was assigned to the CH_2- to compute the ratio in the y-axis in figure (4).

The ratio of oxidized to reduced functionalities (COOH + COH / CH_2) were seen to remain constant with RF-treatment time beyond 30 min. RF-plasma activated samples for 30 min were used in the experiments reported in Figures 5 and 6 when assessing the *E. coli* inactivation kinetics. The lower trace in Figure (4) shows the ratio of surface oxidized to the reduced species when the RF-plasma was carried out at atmospheric pressure. A modest increase in the ratio oxidized surface groups/reduced groups was observed. In this case, the RF pretreatment heated the polyester breaking intermolecular H-bonds and allows the introduction of oxidative functionalities [7,43,51]. Water evaporation is introduced on the

polyester fibers by the RF-pretreatment. This allows for the diffusion of the TiO_2 inside polyester as a function of the RF-plasma pretreatment time (see Figure 4).

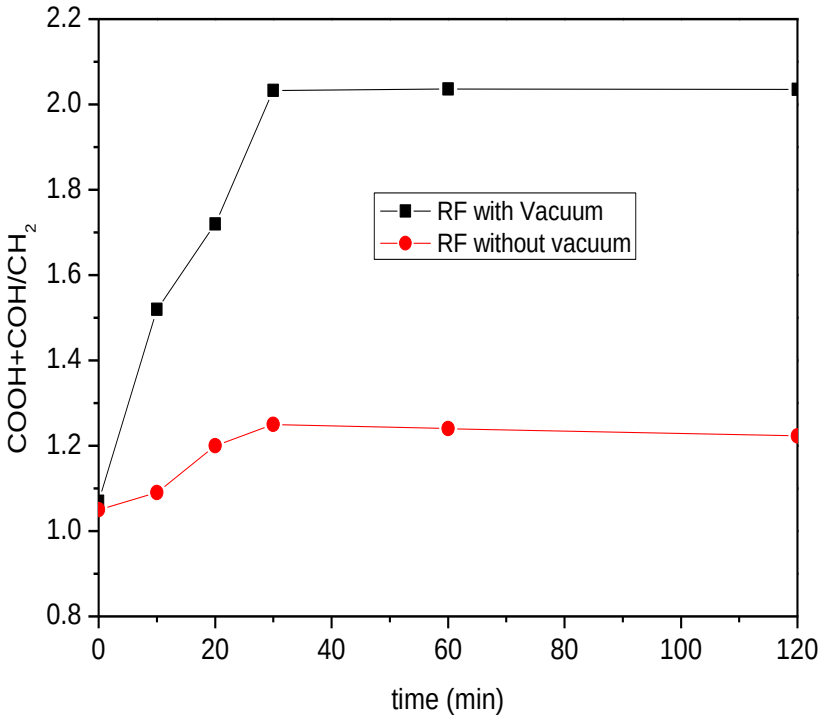

Figure (4): Ratio of oxidized to reduce functionalities (COOH + COH/CH_2) introduced by RF-plasma pretreatment on polyester as a function of time.

3. X-ray fluorescence determination of the Ti weight percentage on polyester samples (XRF)

Table 3 shows the weight percentages of Ti on the polyester samples. The wt% Ti/wt polyester shown in Table 3 provides further support of wt% TiO_2 on polyester as the RF-plasma treatment time increases.

Table 3: Percentage weight of Ti on RF-treated samples as a function of treatment time determined by X-ray fluorescence

RF pretreatment time (min)	% TiO_2 (wt/wt) polyester	% Ti (wt/wt) polyester
0	0.345	0.201
10	0.462	0.285
20	0.621	0.341
30	0.972	0.586
60	0.978	0.588
120	0.975	0.587

4. Generation of the OH-radicals on TiO_2-polyester as a function irradiation time

Figure (5a) presents the increase in fluorescence of the polyester samples P0, P1, P2, P3 (polyester RF-plasma pretreated for 10, 20 and 30 min and subsequently coated with TiO_2) as a function of irradiation time up to 120 min by means Osram Lumilux 18W/827 actinic (dose 4.1 mW/cm^2). The results presented in figure (5b) show the favorable effect of an increase RF-plasma pretreatment time up to 30 min on the polyester samples enhancing OH-radical generation upon illumination of the terephthalic acid [49,50]. Upon illumination, the terephthalic acid in NaOH solution converts on the TiO_2 coating to a highly fluorescent hydroxy-terephthalic acid. Monitoring the increase of the later compound allows the estimation of the TiO_2 surface oxidative species, mainly the OH-radicals. We can only suggest that the active sites on the RF-pretreated TiO_2 coated polyester are introduced from two sources: a) by the RF-pretreatment of the polyester generating oxidative functionalities as shown in figure (4) absorbing above 400 nm and b) by the impurities, defects and dangling bonds of the TiO_2 anatase crystallites of the colloidal coating shown in figure (10) absorbing in the visible range.

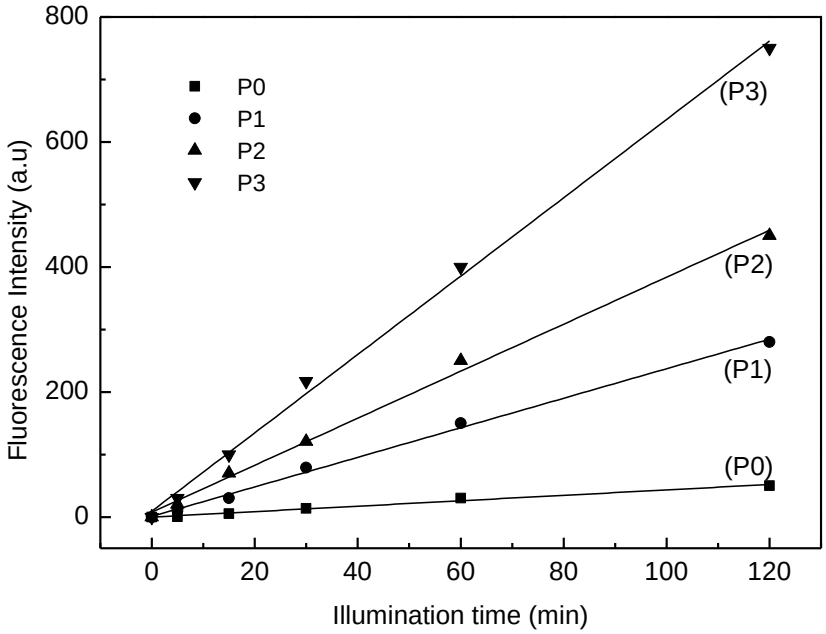

Figure (5a): Fluorescence intensity *vs* illumination up to 120 min time for samples P0, P1, P2, P3

Figure (5b) presents the fluorescence intensity of polyester samples P0, P1, P2, P3 after 30 min illumination. The actinic lamp used to activate the fluorescence had an emission between 310 and 700 nm with an integral output of 1.1 mW/cm^2. The OH-radicals may photodegrade the polyester support during the photo-induced bacterial inactivation. In figure (9) below, up to the fifth cycle or the degradation kinetics kept constant suggesting that polyester degradation did not occur during the time of sample recycling.

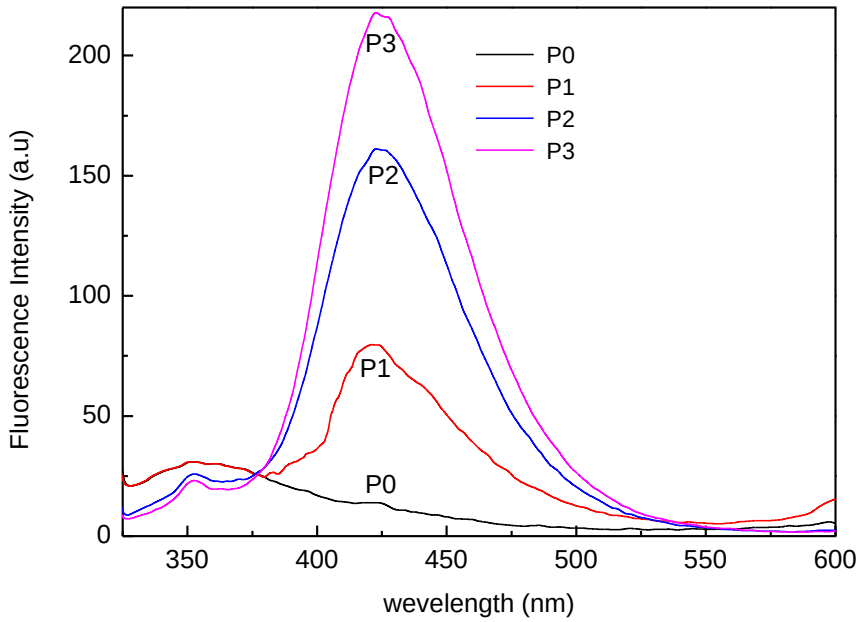

Figure (5b): Fluorescence intensity *vs* wavelength for RF-samples pretreated for: P0, P1, P2, and P3. All samples have been irradiated for 30 min by an Osram Lumilux 18W/827 lamp. For other details see text.

5. Bacterial inactivation on RF pretreated samples. About the effects of light dose, initial E. coli concentration, type of lamp and repetitive bacterial inactivation.

Figure (6) presents the *E. coli* inactivation kinetics by diverse RF pretreated polyester coated TiO_2 samples. Under Osram Lumilux 18W/827 lamp irradiation tuned at a dose 4.1 mW/cm^2. Trace 1 presents the almost negligible disinfection action of the polyester sample by itself. Trace 2) shows a TiO_2-coated polyester without pretreatment inactivating bacteria within 5 hours. Traces 3, 4 and 5 present a faster *E. coli* inactivation as the pretreatment time increases from 10 up to 30 min. Trace 6 (P12) shows that 120 min RF pretreatment period does not further shorten the bacterial inactivation kinetics beyond the one shown by a (P3) 30 min RF-pretreatment. Therefore, the capacity to produce highly oxidative radicals (mainly OH-radicals) seems to reach a maximum after 30 min RF-plasma pretreatment as shown in Figure (4) with respect to the data reported in Figures 5a/5b. Figure (6) shows the fast bacterial inactivation under light on the TiO_2 (Figures 5a and 5b).

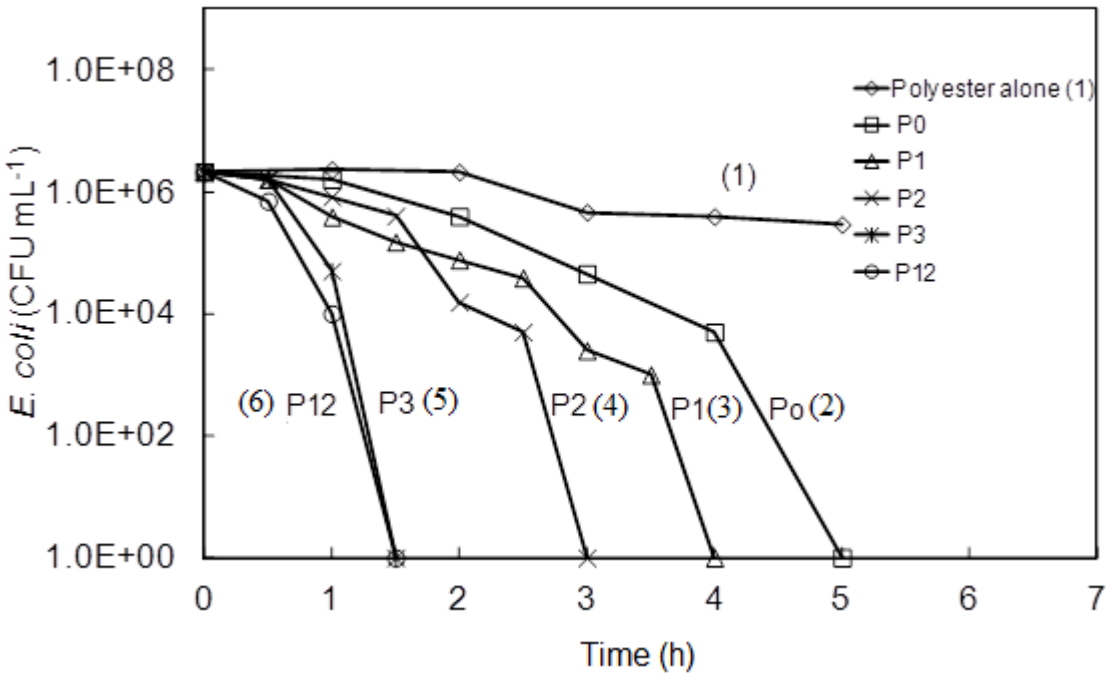

Figure (6): *E. coli* inactivation kinetics of RF-plasma pretreated samples irradiated by actinic light for different times: (1) polyester alone, (2) P0: TiO_2 coated, polyester not RF-plasma treated, (3) P1 RF-plasma treated sample for: 10 min, (4) P2: 20 min, (5) P3: 30 min and (6) P12: 120 min.

Figure (7a) presents the bacterial inactivation kinetics applying different light doses from an Osram 18 W/827. It is readily seen that the bacterial inactivation is strongly dependent on the light dose in the reactor cavity.

Figure (7b) shows the light dose dependence for the bacterial inactivation but this time using an Osram L18W/840 light source (400-720 nm), with a small modification in the spectral distribution compared to the light source used to irradiate samples in figure (7a), the time of inactivation was observed to decrease and become longer by a factor of 2. This up-to-date actinic light is currently used in hospital facilities in Switzerland and this was the reason to carry out the experiment shown in figure (7b).

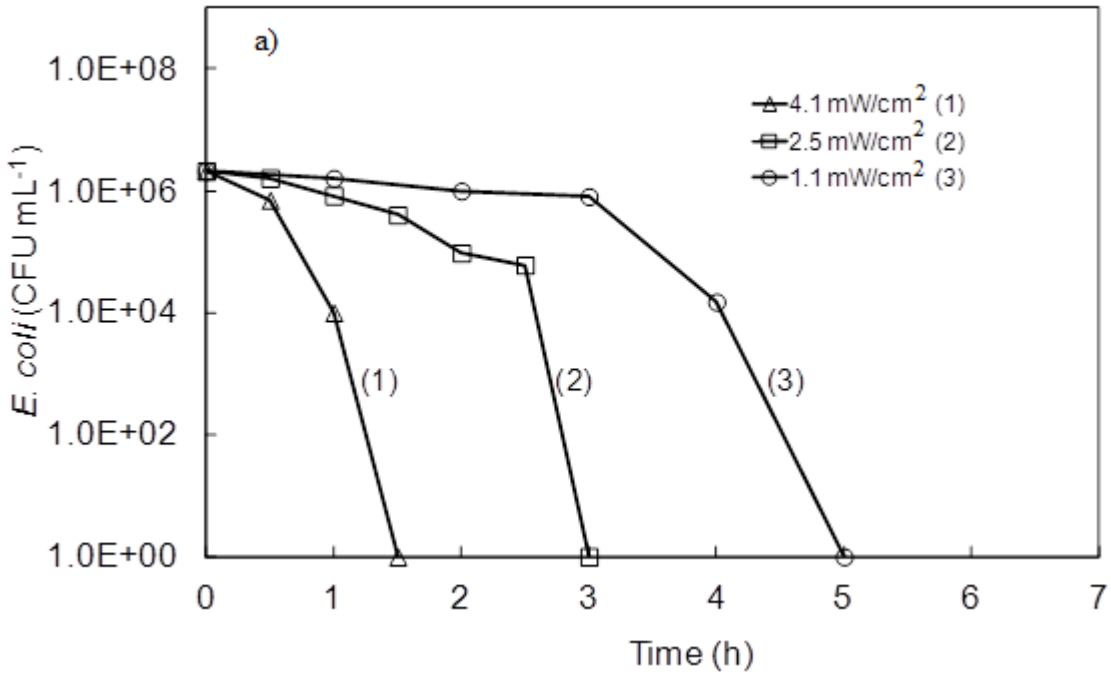

Figure (7a): Effect of light intensity on the bacterial inactivation kinetics applying light from an Osram Lumilux 18 W/827 lamp on a P3.

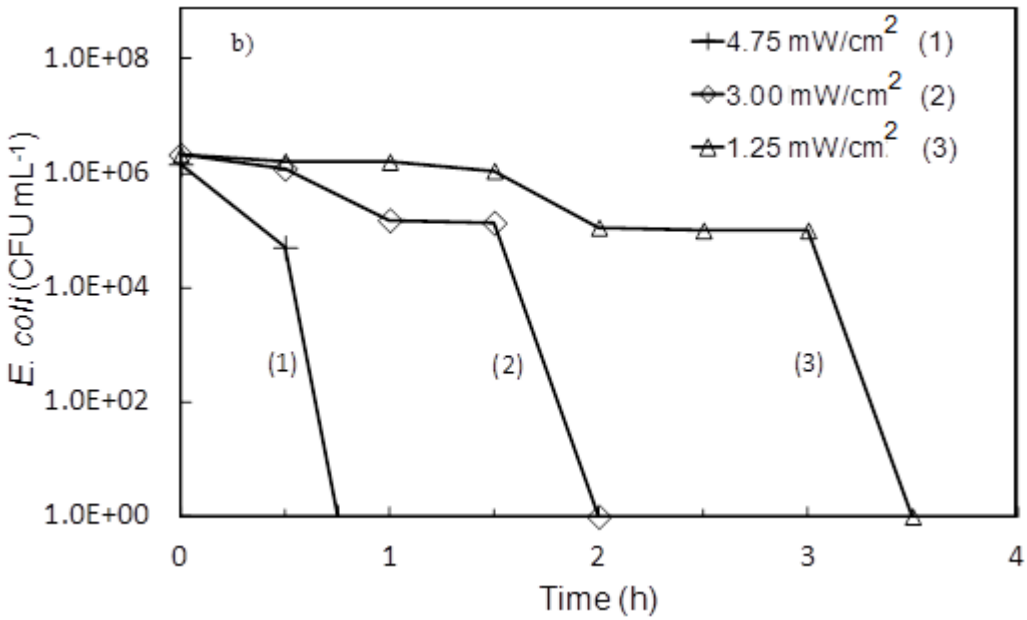

Figure (7b): Effect of light intensity on the bacterial inactivation kinetics applying light from an Osram Lumilux L18 W/840 lamp (see spectra in chapter 2) on a P3.

Figure (8) shows the effect of the initial *E. coli* concentration on the bacterial inactivation kinetics. The time of inactivation as a function of the initial E. coli concentration was explored for the concentrations noted in the caption to figure (8). The time of inactivation became longer by a factor of almost three when the initial bacterial concentration was increased by ~3 orders of magnitude. This experiment was carried out to ensure that the present photocatalyst follows a normal inactivation behavior when interacting with *E. coli*, taken longer times to inactivate a higher initial CFU concentration.

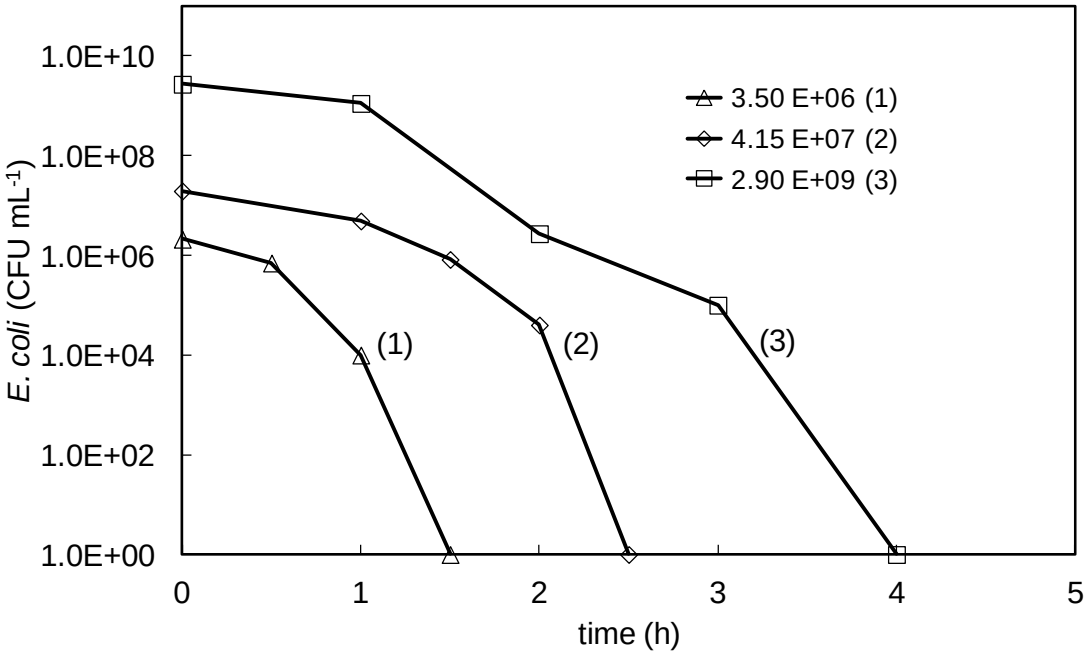

Figure (8): Effect of the initial concentration of E. coli on the inactivation kinetics under light irradiation from an Osram Lumilux 18 W/827 lamp using a P3

Figure (9) presents the repetitive E. *coli* inactivation by recycling an RF-plasma pretreated for 30 min polyester-TiO_2 sample. Complete inactivation of a bacterial ~7log10 concentration was observed under actinic light up to the 5th cycle within 1.5 h. The constant bacterial inactivation time shows the stable nature of the TiO_2 photocatalyst.

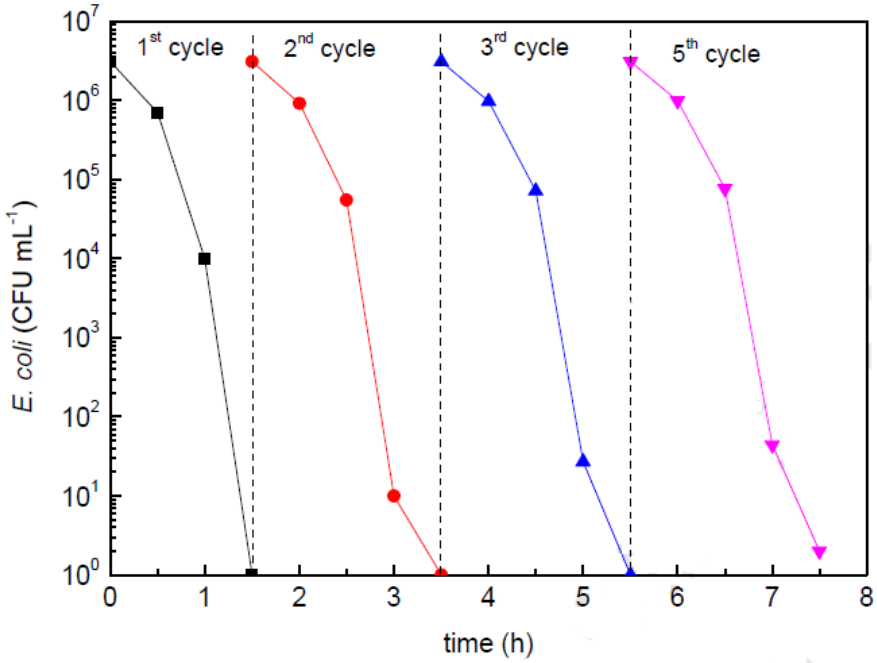

Figure (9): Recycling of an RF-plasma 30 min pretreated sample loaded with TiO_2 (P3) under an Osram Lumilux 827/18 W lamp up to the 5th cycle.

6. Diffuse reflectance spectroscopy and visual perception of TiO_2-polyester coated samples.

The diffuse reflectance spectroscopy (DRS) of the P0, P1, P2, P3 samples and of the control sample is shown in figure (10). The spectra in figure (10) show the relation between the light absorption in Kubelka–Munk units and the RF-plasma pretreatment time. The rough UV–Vis reflectance data cannot be used directly to assess the absorption coefficient of the RF-pretreated polyester samples because of the large scattering contribution to the reflectance spectra. Normally, a weak dependence is assumed for the scattering coefficient S on the wavelength. In figure (10), the scattering coefficient S is a function of the spectral wavelength in the DRS spectrum. The KM/S values for the samples in figure (10) follow the bacterial inactivation kinetics reported in figure (6). The wt% Ti / wt polyester shown in Table 3 lends further support to the increased absorption of the samples as the Ti-content of the polyester increases. The absorption for the polyester alone is due to the TiO_2 used as whitener during the fabrication of the polyester described in Section 2.

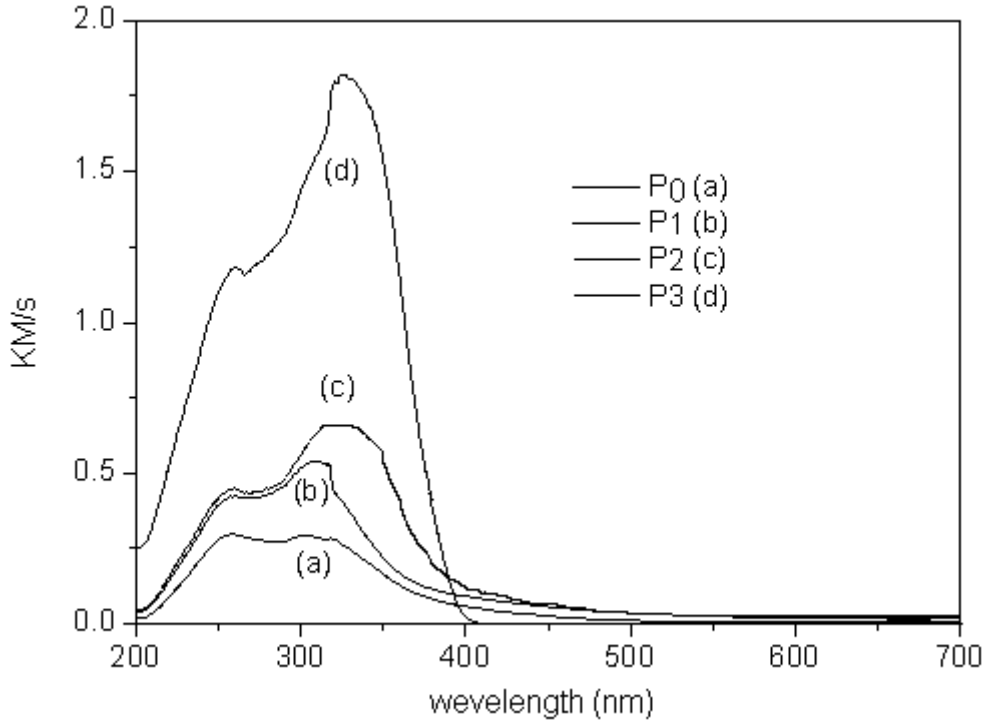

Figure (10): Diffuse reflectance spectra (DRS) of P0 (a), P1 (b), P2 (c), P3 (d)

7. Electron microscopy of samples (TEM) of TiO_2-polyester coated samples

Figure (11) presents the TEM of (a) the polyester sample and (b) of the TiO_2 nano particles layers on polyester being 25 an 80 nm thick on a RF-plasma pretreated (P3) sample. The TiO_2 P-25 Degussa particles present sizes between 20 and 30 nm. This means that the coating in figure (11) comprise between one and four TiO_2 layers.

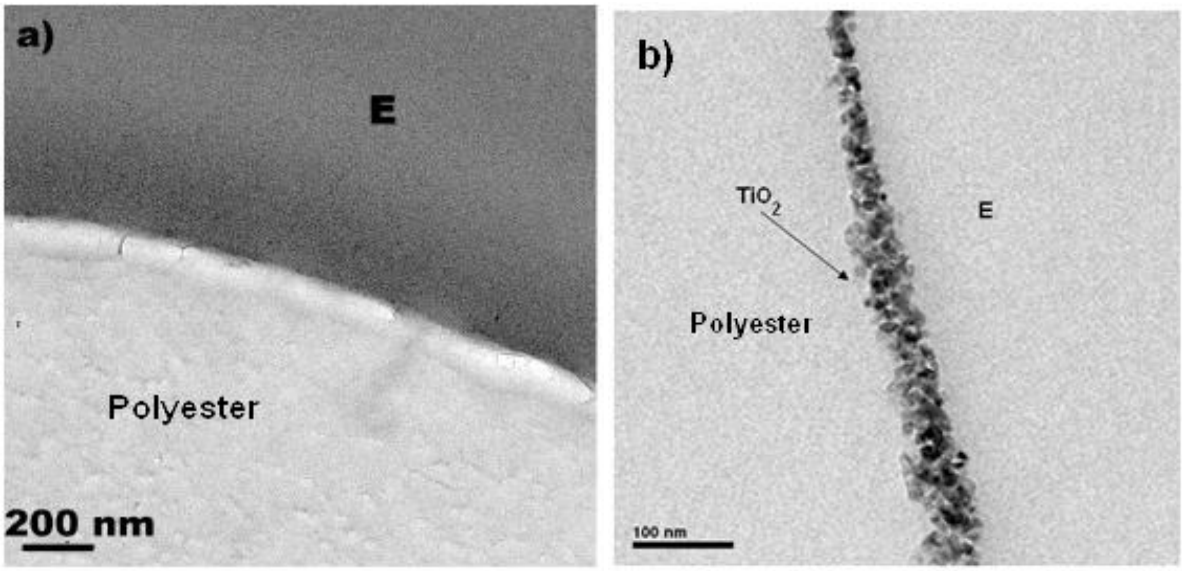

Figure (11): Transmission electron microscopy of (a) polyester sample and (b) TiO_2-polyester RF-plasma pretreated for 30 min (P3). E stands for epoxide used in the preparation of the sample.

8. X-ray diffraction (XRD) of TiO_2 polyester samples

Figure (12) shows the XRD for polyester and for TiO_2-polyester sample RF-plasma pretreated for 30 min (P3). The strong signal for anatase at 25.2◦ makes up 80% of the TiO_2 Degussa P25 and the smaller anatase satellite peaks are seen in figure (12).

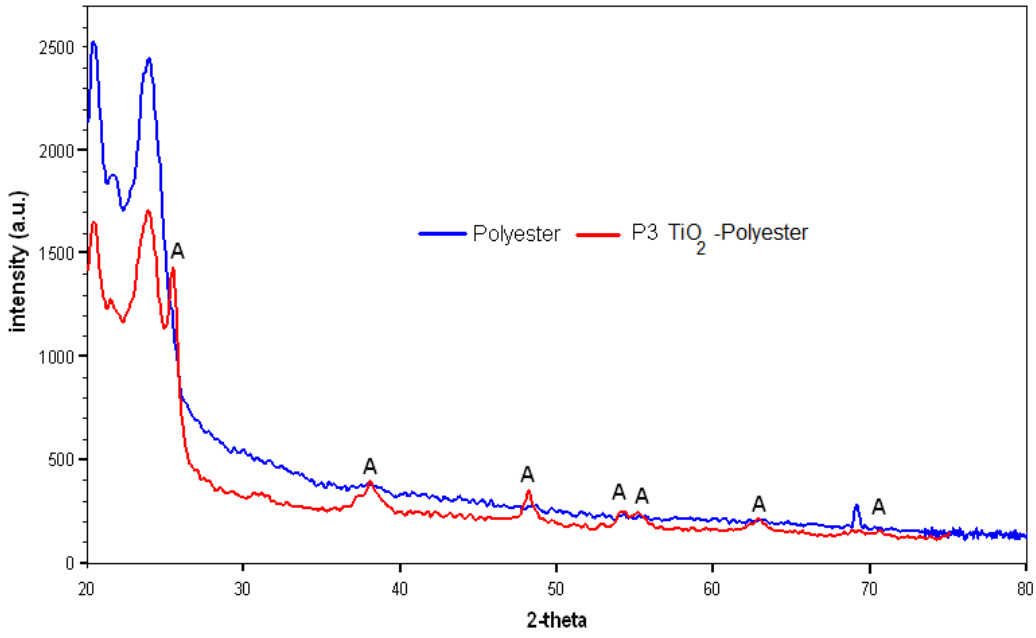

Figure (12): X-ray diffraction of polyester alone sample used as reference (lower trace) and an RF-plasma sample pretreated for 30 min coated with TiO_2 (P3). For more details see text.

9. Contact angle (CA) determination of polyester and TiO_2 polyester samples

The contact angle (CA) was measured before and after the plasma treatment (30 min). Figure (13a) shows that the contact angle of untreated polyester film was about 95°. After plasma treatment, the contact angle decreased dramatically. It is too small to be measured directly by goniometer because the water spreads on the surface, as figure (13b) shows. The surface after plasma treatment is super-hydrophilic (i.e., practically near 0°). The hydrophilicity is induced by the progressive formation of polar functional groups such as -OH and –COOH

a) Untreated polyester film

b) Superhydrophilic polyester film after plasma treatment (30 min)

Figure (13): Contact angle measurements for untreated and pretreated polyester films.

Figure (14) shows the contact angle (CA) for the water droplet on polyester surface for the samples as noted in the caption to figure (14). The sessile water drop disappears with time faster in the case of polyester than when the polyester has been RF-treated and subsequently coated with TiO_2. Although the polyester is hydrophobic, contact with water droplets shows the later effect due to high porosity (void areas, 20 μm pore sizes) of the polyester allowing for water penetration through the polyester microstructure. The void areas are reduced by the addition of TiO_2 since it decreases the water penetration and concomitantly increasing the sample hydrophobicity.

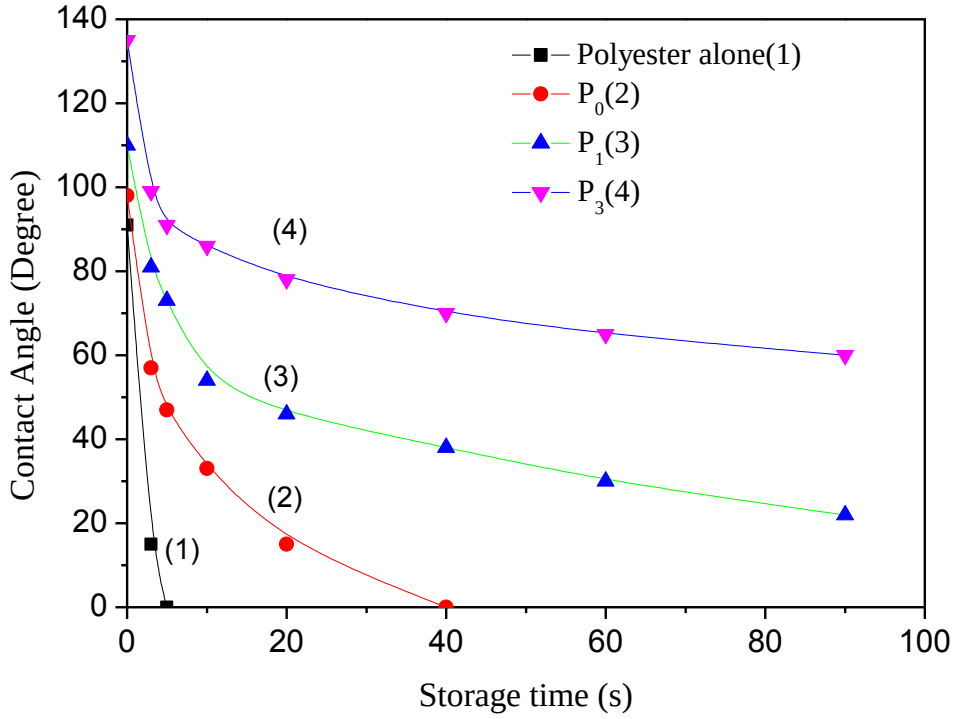

Figure (14): Contact angle as a function of time for (1) polyester alone, (2) RF-plasma pretreated samples for 10 min, (3) RF-plasma pretreated samples for 20 min and (4) RF-plasma pretreated samples for 30 min.

10. X-ray photoelectron spectroscopy (XPS) of TiO_2 polyester sample (P3)

Figure (15a- trace 1) presents the $Ti2p_{2/3}$ peak at time zero 457.85 eV due to the TiO_2 particles deposited on the polyester. Figure (15a traces 2 and 3) shows that after 60 and 90 min as the inactivation bacterial progress. The 457.85 eV line signal shifted significantly during the bacterial inactivation to 458.25 eV. This is the evidence for a Ti^{4+}/Ti^{3+} redox reactions taking place on the TiO_2 polyester surface in contact with surface bacteria. Shifts in the XPS peaks ≥ 0.2 eV reflect the changes in the oxidation states of the elements [180].

Table 4 shows the surface atomic concentration % on an RF-plasma pretreated sample of 30 min (P3) during bacterial inactivation under actinic light irradiation. The rapid destruction of C- due to the bacterial destruction is shown by the sample C-concentration after the 3 s. The O, N and Ti are seen to remain constant up to 120 min.

Table 4: Surface percentage atomic concentration of TiO_2-coated polyester during *E*. coli inactivation as determined by XPS. The first row refers to a sample not contacted with bacteria.

Sample identifier	% C	% O	% N	% Ti
0	28.51	51.23	0.36	19.9
3s	48.06	37.68	1.02	13.24
30min	50.32	36.59	1.05	12.04
60min	52.14	36.95	0.37	10.46
120min	52.85	36.42	0.39	10.34

Figure (15b) shows the deconvoluted spectrum of a RF-plasma pretreated polyester sample TiO_2 coated showing the OH-group at 531.0 eV [35] and the Ti-O at 529.8 eV [180] and the Ti-O-C peak at 532.8 eV [53]. A large amount of adsorbed/chemisorbed water was introduced in the sample during the sol–gel coating at temperatures no higher than 100 ◦C. The amount of surface OH_{surf} radical adsorbed on the sample is higher after the RF-plasma pretreatment (data no shown) due to the increased hydrophilicity of the O- polar groups due to the RF-plasma pretreatment.

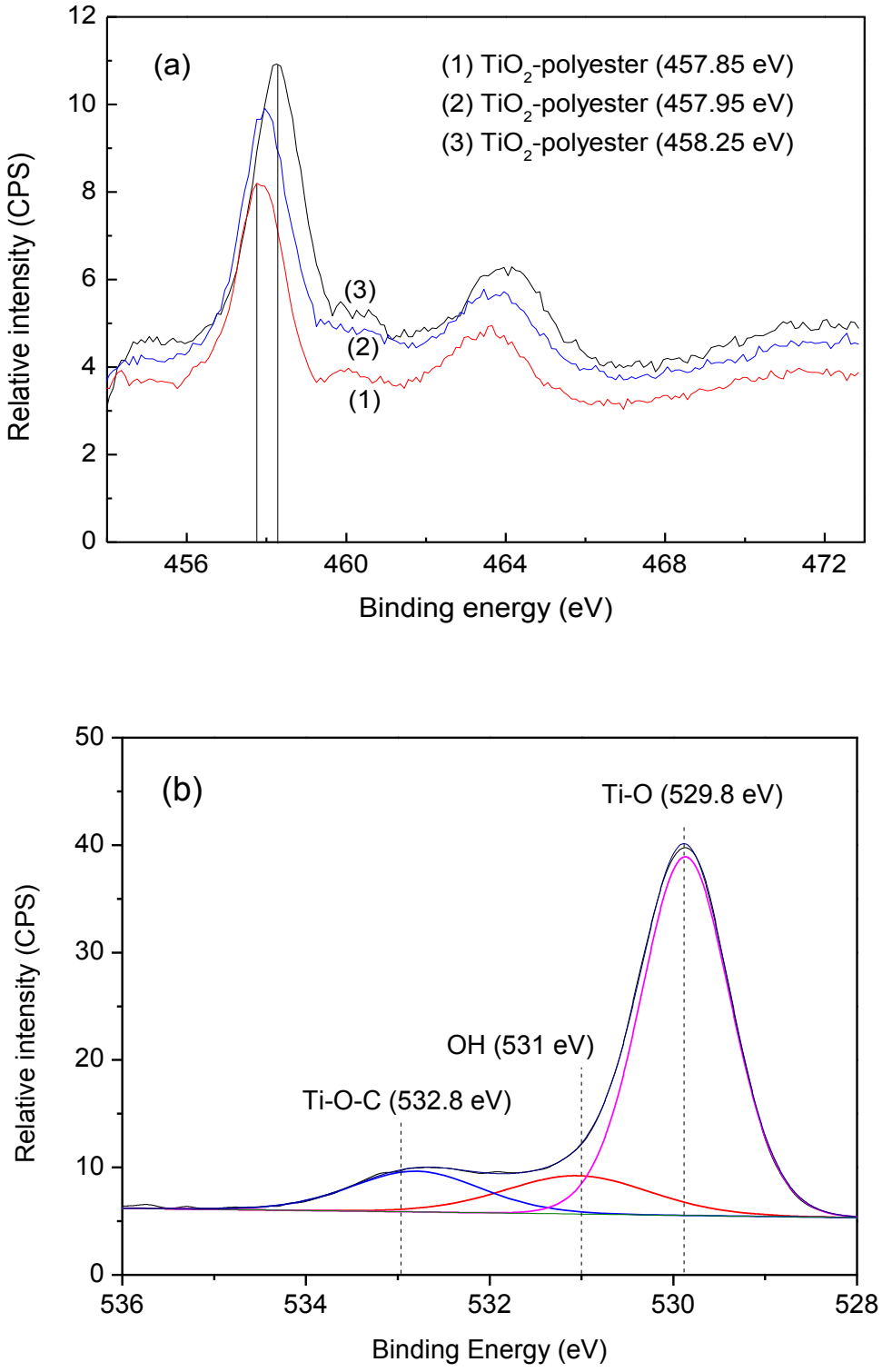

Figure (15): (a) XPS Ti2$p_{3/2}$ peak shift in a sample RF-plasma pretreated for 30 min during E. coli inactivation: (1) at time zero, (2) at time 30 min and (3) at time 90 min. **(b)** XPS O1s spectra of RF-pretreated polyester loaded TiO_2 showing the Ti-O and T-O-C and the OH_{surf} surface groups.

11. Conclusion.

RF-plasma is shown to be a useful pretreatment method to increase the number of active sites and bondability on the polyester surface allowing for a much higher TiO_2 loading on the textile compared to non-pretreated samples. The pretreated samples accelerate significantly *E. coli* inactivation reducing by a factor of >3 the bacterial inactivation time compared to non-pretreated polyester TiO_2 samples. The polyester RF-plasma pretreatment induced modifications of the surface ratio of oxidative and reductive species in the polyester surface as detected by XPS. Oxidative species (mainly OH-radicals) were identified on the light irradiated polyester-TiO_2 samples and a higher amount of oxidative species lead to a faster bacterial inactivation. TEM of the RF-plasma pretreated polyester shows a continuous microstructure for the TiO_2 coating on the polyester surface. By XPS, self-cleaning of the bacterial inactivation residues on the polyester-TiO_2 was confirmed which enables the sample to inactivate a new bacterial charge at the end of each separate disinfection cycle.

Chapter 5: Ag-surfaces sputtered by DC, pulsed DC-magnetron sputtering and HIPIMS effective in bacterial inactivation: Testing and characterization

1. Thickness of the Ag-sputtered films by DCMS, DCMSP and HIPIMS on polyester

The nominal calibration of the Ag-film thickness was carried out for DCMS, DCMS Pulsed and HIPIMS Ag-deposition at different current intensities (A) on Si wafers. The thicknesses of the Ag-film as well as the weight percent of Ag for diverse sputtering times using DCMS, DCMSP and HIPIMS at 0.05, 0.3, 1, 2 and 5 Amps are shown in Table 1 up to 160 s. The calibration traces in Figure (1a), (1b) and (1c) presented a ±10% range of experimental error.

Figure (1a) indicates for 0.3 Amp DCMS or DCMSP that a thickness of 102 and 105 nm successively was attained after 80 s the thickness for both Ag-films sputtered by DCMS and DCMSP is seen to be similar in figure (1a) and the rate of deposition is 78 nm/min. Taking a 0.3 nm lattice distance between the Ag-atoms, about 10^{15} atoms/cm^2 can be estimated leading to the deposition rate of Ag-deposition of 6×10^{15} atoms/cm^2 s. Therefore, in one second a 1.2–1.25 nm Ag-layer was deposited equivalent to ~6 layers of 0.2 nm thick.

Figure (1b) shows that DCMS sputtering of Ag at a higher current of 0.3 Amp (rate 78 nm/min) increases the Ag-deposition rate by a factor of 8 with respect to Ag deposition at a lower current of 0.05 Amp (rate 12 nm/min). Figure (1c) shows that a thinner Ag-coating is deposited within the same times by HIPIMS compared to DCMS or DCMSP sputtering shown previously in figure (1a). Which means that the rate of deposition in HIPIMIS at 5 Amps (rate 30 nm/min) is lower compared to DCMS and DCMSP at 0.3 Amp (78 nm/min) in agreement with results recently reported by Hosokawa and Vlček [72, 101].

Table 1: Relation between the sputtering time used during DCMS, DCMSP and HIPIMS, the % Ag wt/wt and the film thickness

DCMS	Time(s)	% Ag wt/wt	Thickness nm
0.05Amp	10	0.0012	2
	20	0.0025	4.5
	80	0.0081	18
	160	0.0172	36
0.3 Amp	20	0.0282	26
	40	0.0520	52
	80	0.1180	105
	160	0.1780	208
DCMSP	Time(s)	% Ag wt/wt	Thickness nm
0.3 Amp	20	0.0259	25
	40	0.0430	50
	80	0.0870	102
	160	0.2050	204
HIPIMS	Time(s)	% Ag wt/wt	Thickness nm
1 Amp	2	0.002	2
	13	0.003	4
2 Amps	3	0.014	7
	10	0.021	15
5 Amps	13	0.0029	7
	37	0.0086	20
	75	0.0315	40
	150	0.0630	80

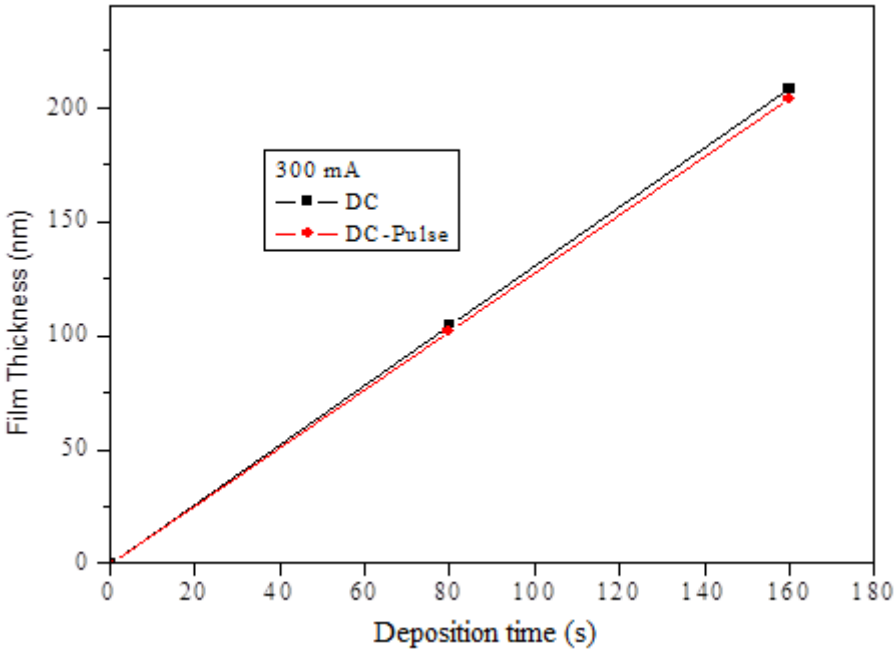

Figure (1a): Calibration of the Ag-layer thickness sputtered at 0.3 Amp by DCMS and DCMSP as a function of time on Si-wafers.

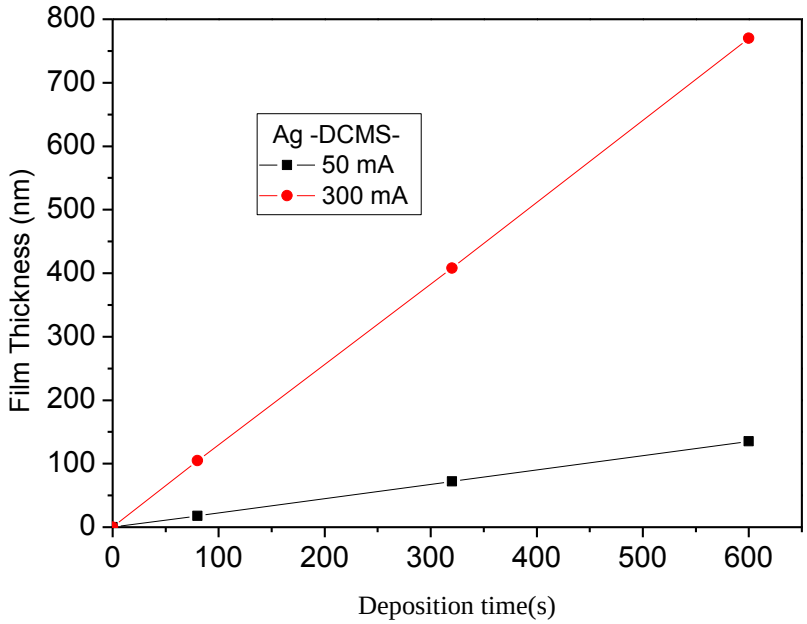

Figure (1b): Nominal calibration of the Ag-thickness obtained by DCMS sputtering at 0.05 Amp and 0.3 Amp

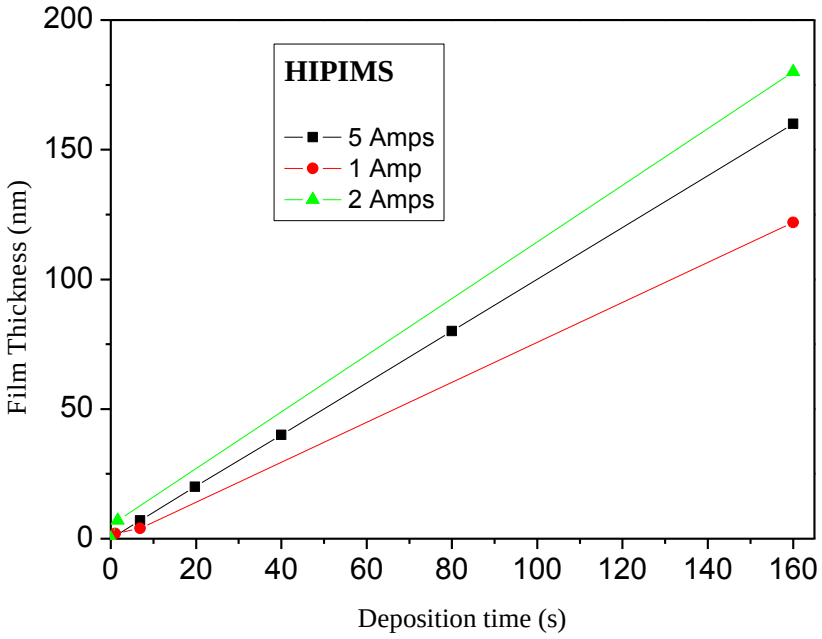

Figure (1c): Nominal calibration of the Ag-layer thickness obtained by HIPIMS sputtering with currents of 1, 2 and 5 A.

2. X-ray fluorescence of Ag-polyester sputtered samples

The Ag-content of the polyester sputtered samples was determined by X-ray fluorescence. The % Ag wt/wt polyester sputtering by DCMS at 0.3 A is a function of the sputtering times between 20 and 160 s as shown in the upper half of Table 1. The Ag-film thickness increases concomitantly with the Ag-deposited on the polyester. The lower half of Table 1 shows the results for the Ag-amount on the polyester for DCMSP sputtered samples for times between 20 and 160 s. The thickness for both Ag-films sputtered by DCMS and DCMS pulsed is seen to be similar in Table 1.

The most effective *E. coli* inactivation by a DCMS and DCMSP sputtered sample during 160 s presented Ag-loadings of 0.178 and 0.205 Ag wt%/ wt polyester reached Ag-loadings ~3 times higher than the loading obtained by HIPIMS after 150s sputtering (0.0630 % Ag wt/wt). The nominal thickness of the 160 s layer sputtered by DCMS and DCMSP layer was 208 and 204 nm and the thickness observed for the HIPIMS sputtered layers for 75 s was 40 nm. This explains the lower content in Ag in the HIPIMS-sputtered sample compared to the DCMS and DCMSP-sputtered sample. Both samples were of interest since they led to complete *E. coli* inactivation within 5h for DCMS and within a similar time of ~2 h by DCMSP and HIPIMS sputtered samples as shown in figures (4a), (4b) and (5b).

3. Nanoparticles Ag-films as a function of sputtering time

Photograph (2.1-a) shows the polyester sample alone. Photograph (2.1-b) shows DCMS sputtered Ag-polyester sample for 20 s at 0.05 A and finally Figure (2.1-c) polyester sputtered for 160 s at 0.3 A. The polyester alone in Photograph (2.1-a) shows no color in the absence of Ag. Photograph (2.1-b) shows color due to Ag-deposition. Ag nanoparticles are formed when the plasma containing the Ag condense on the polyester surface (insulator). Ag atoms have been reported to have a strong preference to bind to other Ag-atoms rather than to the polyester surface. This leads to the production of Ag-near spherical clusters that are not necessarily crystallographic [93,189]. The association of Ag-atoms at the polyester surface into nanoparticles corresponds to Ag-metal clusters that are initially not crystallographic [174,190]. The Ag-sputtered nanoparticles for longer times in Photograph (2.1-c) grow into bigger agglomerates leading to a darker film that is a function of the applied current. A current of 0.3 Amp in Figure (2.1-c) compared with 0.05 A in Photograph (2.1-b) produces a nanoparticles film. The same results have been obtained with DCMSP. The Ag-atoms diffuse anisotropically on the textile surface and the subsequent migration/aggregation of the Ag-particle is driven by the high energy given to the Ag-ions leading to thermodynamically stable agglomerates [180, 181]. But the high energy given to the Ag-ions can also be released when the Ag-ions arrive at the polyester surface recombining with surface electrons or bonding with the textile surface.

Photograph (2.2) presents the Ag-nanoparticle films sputtered by HIPIMS for different times. The samples (2-a) polyester alone shows no color in the absence of Ag. A light brown grey-color appears in sample (2-b) shows dark-grey metallic Ag-color due to HIPIMS sputtered for 13 s at 5 A. The darker film on the polyester in Photograph (2.2-c) is due to the longer sputtering time of 75 s at 5 A.

The energy of Ag-ions is up to 30 eV and the average energy is 2 eV. In DCMS these energies are significantly lower and lie between 1-5 eV. Although DCMSP energies can reach more than 100 eV this energy delivered to the gas ions, which settle on the polyester surface forming Ag-films. In HIPIMS the % ionization of Ag-ions reach 50-90 %. This results in denser films, with less porosity or voids. We are not set-up to measure the energy of the Ag-ions during DCMS, DCMSP and HIPIMS sputtering.

The color in photographs (2.1) and (2.2) corresponds to the composite Ag/Ag_2O. The Ag_2O has been reported to have a band-gap (bg) 0.7–1.0 eV vs SCE and an absorption edge of 1000 nm [189]. Photograph (2.2) presents two Ag-nanoparticle films deposited by HIPIMS

for 13 s coating of 7 Ag-layers with an Ag %wt/polyester wt loading of 0.0029 as shown in Table 1. The HIPIMS sputtered sample for 75 s shows a darker color compared to the HIPIMS sputtered layers due to the thicker Ag-nanoparticle films of 40 nm with a loading of 0.0315 Ag % wt/polyester wt. We use the term Ag-nanoparticle films since the films are continuous and composed of nano-sized grains.

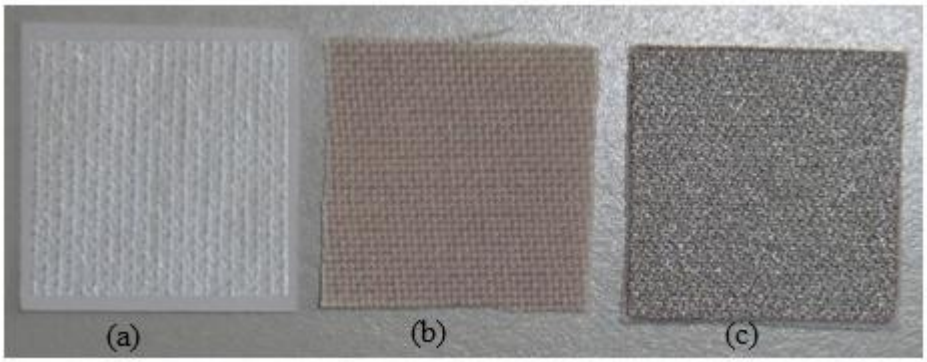

Photographs (2.1): Samples prepared by DCMS pulsed: (a) polyester alone; (b) Ag-DCMS 20 s, 0.05 A, and (c) Ag-DCMS 160 s, 0.3 A

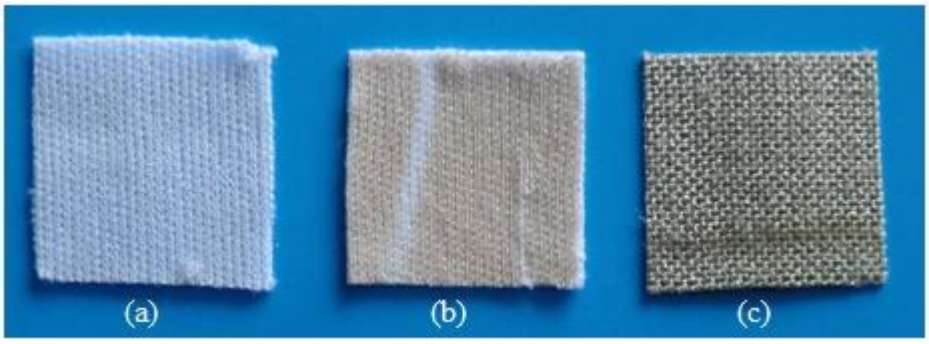

Photographs (2.2): Samples prepared by HIPIMS: (a) polyester alone, (b) Ag-HIPIMS 13 s, 5 A, and(c) Ag-HIMIMS 75 s, 5 A.

4. Inactivation kinetics of E. coli on Ag-polyester sputtered by DCMS and DCMSP with different times and energies (Amps)

Figure (3a) presents the results of the *E. coli* inactivation by Ag DCMS-sputtered samples at 0.05 A and also the experimental setup for the bacterial determination. Practically no *E. coli* inactivation was observed by polyester alone (Fig. 3a, trace1). The samples sputtered for 20 s, 80 s and 160 s showed an increased bactericide activity leading at longer

sputtering times to bacterial inactivation within 7 h. In figure (3b) a short *E. coli* inactivation kinetics within 3 h was found for DCMSP using 0.05 Amp up to 160 s (trace 5).

Figure (4a) presents the *E. coli* inactivation kinetics by Ag DCMS-sputtered at 0.3 Amp, the highest current possible in our magnetron-sputtering unit. The samples sputtered for 20 s, 80 s and 160 s showed that complete *E. coli* inactivation was attained within 5 h for the 80 s (trace 3) sputtered sample. This is a shorter *E. coli* inactivation compared to samples sputtered for 160 s sputtered at 0.05 A. Figure (4b) presents a faster *E. coli* inactivation kinetics for DCMS Pulsed applying 0.3 A. Samples sputtered for 160 s (trace 5) inactivated *E. coli* within 2 h. The threshold Ag-loading for polyester by DCMSP sputtered samples in figure (4b) was attained after sputtering for 20 s (trace 2) and led to inactivation of *E. coli* after 9 h. After 20 s, a coating of ~25 nm Ag is deposited which is equivalent to a coating growth rate of 78 nm/min as shown previously in Figure (1a). The term threshold refers to the minimal polyester Ag-loading able to induce complete bacterial inactivation. If the coating would be continuous and homogeneous, it would made-up of 125 layers since one layer is ~0.2 nm thick. This approximation does not take into account the film voids and grain boundaries. This gives an equivalent threshold loading of the polyester of 1.2×10^{17} atoms/cm^2. Sputtering for 160 s leads to *E. coli* inactivation within 2 h with an equivalent loading of ~10^{18} atoms/cm^2. The atomic rate of deposition with DCMSP was 1.6×10^{16} atoms Ag/cm^{2}s. Since the thickness of the Ag-film was observed to be about the same for the DCMS and DCMS Pulsed Ag deposition on polyester as shown in Figure (1a) and Table 1, show similar amounts ofvAg/cm^2 on the polyester. But the different structure/coverage Ag on the polyester fibers by DCMSP compared to DCMS seems to be the cause for the shorter *E. coli* inactivation kinetics. Evidence will be presented in the EM and XPS sections below in Figure (6) and figure (9) for these 2 samples. The *E. coli* inactivation process has been described to proceed by Ag-ionic states in air due to ambient humidity and leads to the high oxidative radicals $HO_2^{\bullet}$ and $OH^{\bullet}$ necessary for *E. coli* inactivation [8,10,16,17,114]. The Ag-crystals in air are covered by layer(s) of AgOH due to the room temperature kT potential energy [191]. Therefore, the films can oxidize after the deposition when exposed to air and during the sterilization process (autoclaving at 121^0).

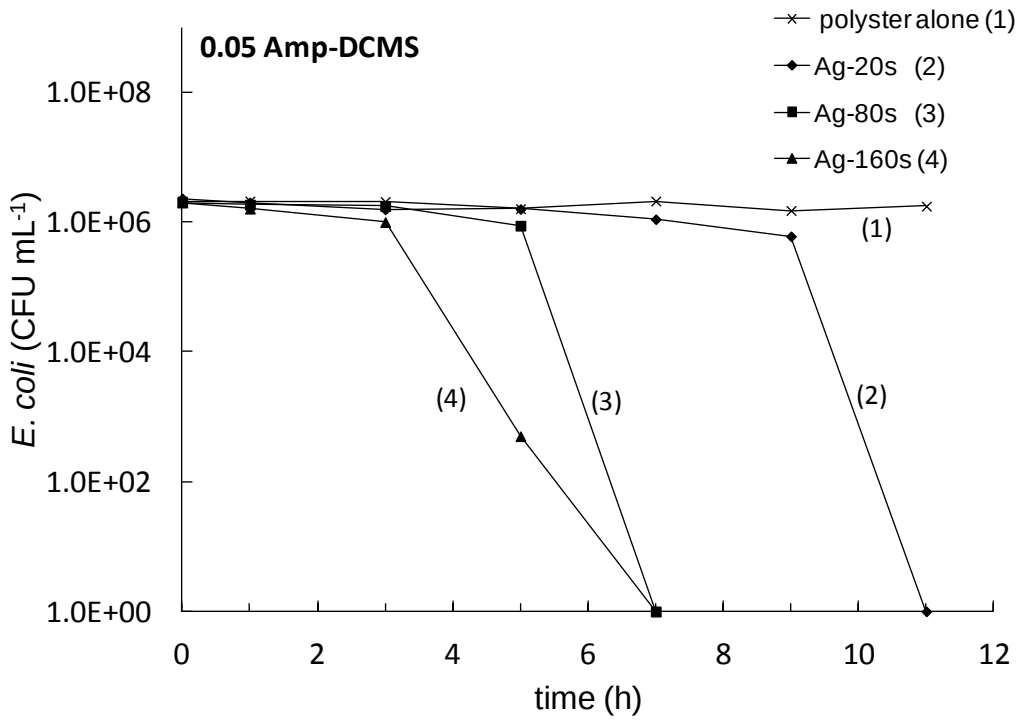

Figure (3a): *E. coli* inactivation kinetics as a function of time on Ag-polyester DCMS-sputtered at different times applying currents of 0.05 A.

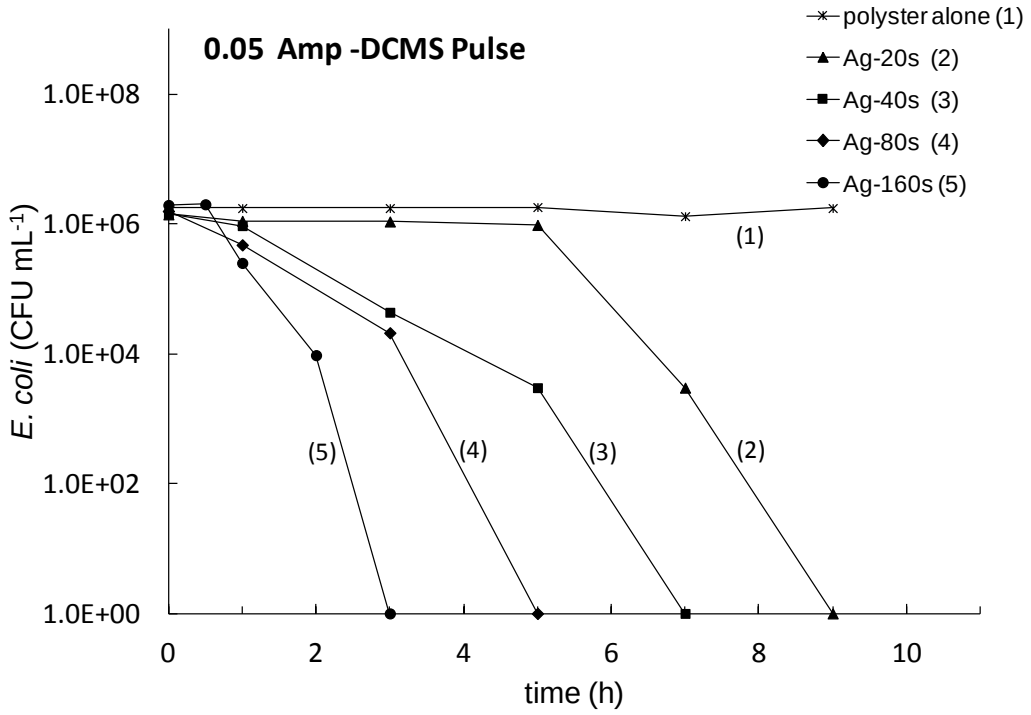

Figure (3b): *E. coli* inactivation kinetics as a function of time on Ag-polyester DCMSP-sputtered at different times applying currents of 0.05 A

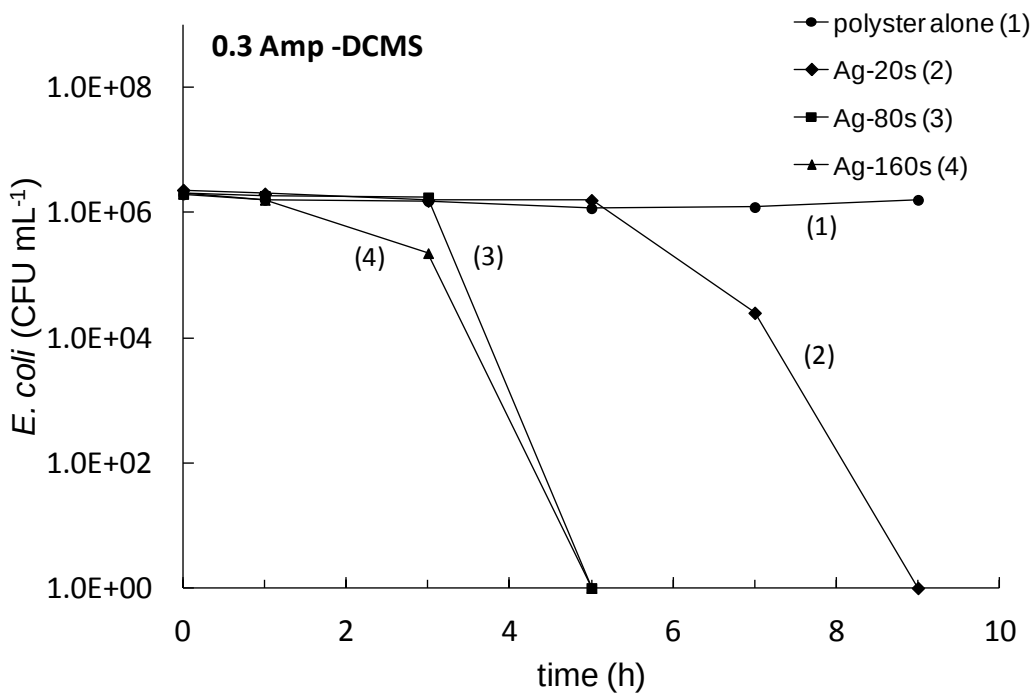

Figure (4a): *E. coli* inactivation kinetics as a function of time on Ag-polyester DCMS-sputtered at different times applying currents of 0.3 A.

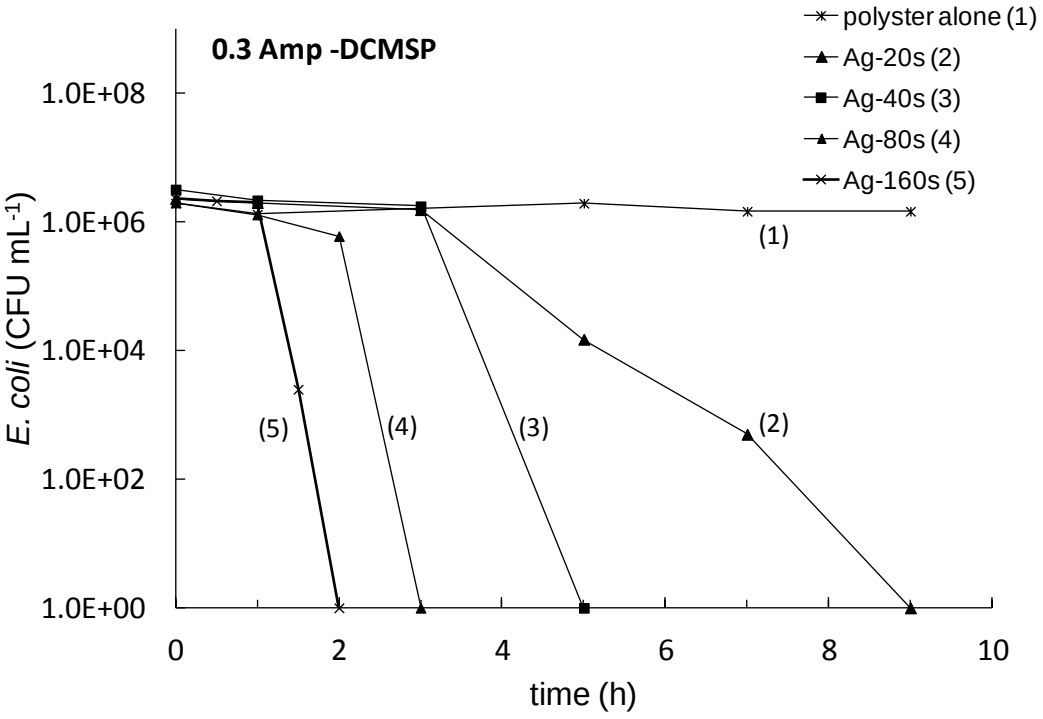

Figure (4b): *E. coli* inactivation kinetics as a function of time on Ag-polyester DCMSP-sputtered at different times applying currents of 0.3 A

5. *E. coli* Inactivation kinetics mediated by HIPIMS sputtered polyester at different times and currents

Figure (5a) presents the results for HIPIMS sputtering at 1 and 2A. HIPIMS sputtering for 3 s at 2 A lead to the most effective Ag-layer in E. coli inactivation having a relatively low Ag-content (Fig. 5a). The initial CFU decrease in figure (5a) for Ag–polyester at time zero with respect to polyester alone is due to redox processes taking place between Ag and *E. coli* as reported recently for Cu-nanoparticles [180]. By inspection of Table 1, a reduction of about 10 times is observed in the Ag-layer thickness and also in the % Ag wt /wt polyester for the samples prepared by HIPIMS at 1 A or 2 A with respect to DCMS and DCMSP samples sputtered for 160s.

Figure (5b) presents the results for the *E. coli* inactivation with HIPIMS. Trace (2) shows that sputtering for 13 s at 5A leads to Ag-samples able to perform bacterial inactivation within 5 h. The threshold polyester Ag-loading was 0.0029% wt Ag/wt polyester (Table 1) was able to induce bacterial inactivation within 5 h. Sputtering times shorter than 13 s did not lead to complete bacterial inactivation. The threshold Ag-coating of 7 nm (see Table 1) is equivalent to 35 layers with a content of 3.5×10^{16} atoms Ag/cm^2. The atomic rate of deposition with HIPIMS therefore is 2.7×10^{15} atoms Ag/cm^{2}s. HIPIMS sputtering for 37 s lead to an Ag-film 20 nm thick with 0.0086 Ag wt.% / wt polyester able to inactivate E. coli within 4 h. DCMS sputtering for 80 s (trace 3) in figure (4a) lead to *E. coli* inactivation within 5 h (and DCMSP only for 40 s). In this case the Ag wt.% / wt polyester was 0.1180 (0.043 DCMSP) and the Ag-layers were 105 nm thick (50 nm DCMSP). DCMS-sputtering required >10 times (>5 times DCMSP) higher loading and led to Ag-layers >5 times thicker (>2.5 times thicker DCMSP) compared to the HIPIMS sputtered samples shown in Figure (5b) inactivating *E. coli* within similar times. This shows the significant saving in Ag-metal and sputtering time introduced by HIPIMS compared to the more traditional DCMS and DCMSP sputtering.

On the other hand, the different structure of Ag on the polyester obtained by different techniques DCMS, DCMSP and HIPIMS at different currents seems to induce the different *E. coli* inactivation kinetics reported in Figure (3a,b), (4a,b) and (5a,b). When applying DCMS, DCMSP and HIPIMS current a different layer-by-layer growth takes place. This involves a different alignment and orientation of the growing crystallites and the crystal defects and the size momentum of the Ag-particles arriving on the polyester surface [65].

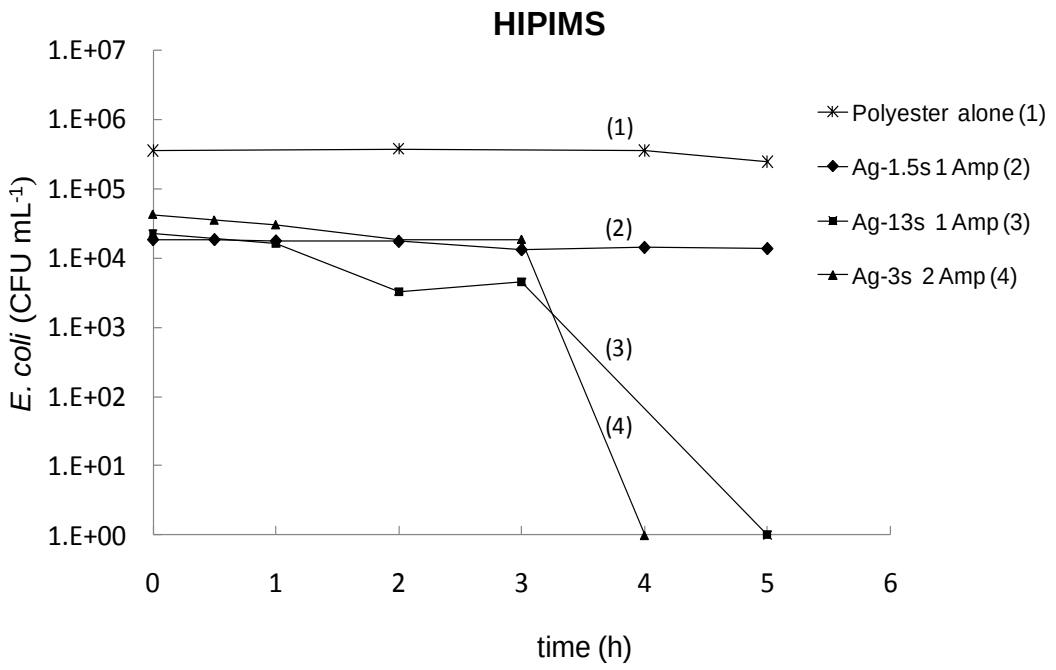

Figure (5a): *E. Coli* inactivation kinetics as a function of time for HIPIMS sputtered Ag-polyester at 1 and 2 Amps

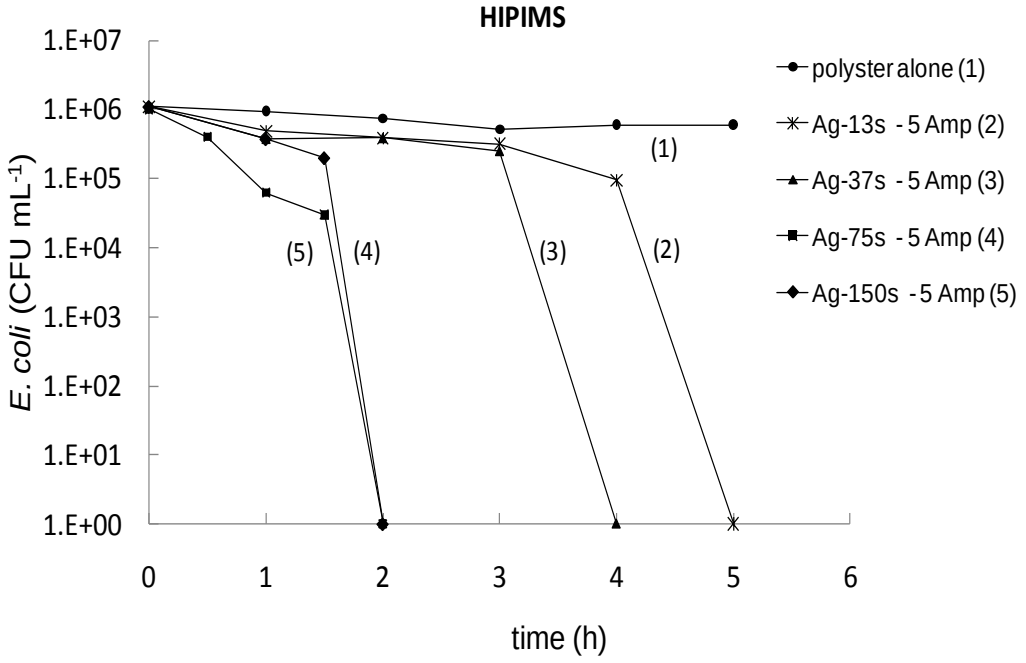

Figure (5b): *E. Coli* inactivation kinetics as a function of time for HIPIMS sputtered Ag-polyester at 5 Amps.

The Ag-polyester samples are shown to lead to significant bacterial inactivation a shown in Figures (3a, b), (4a, b) and (5a, b). We suggest that the ROS of *E. coli* is modified by interaction with Ag^{+}/Ag^{o} by the reactions (1), (2) below:

$$Ag^{o} + O_2 \longrightarrow Ag^{+} + O_2^{\cdot -} \quad (1)$$

$$Ag^{+} + O_2^{\cdot -} \longrightarrow Ag^{o} + O_2 \quad (2)$$

Since H_2O_2 adsorbs on Ag/Ag_2O, peroxide decomposition may take place [8,17]:

$$H_2O_2 + Ag^{o} \longrightarrow HO^{-} + OH^{o} + Ag^{+} \quad (3)$$

$$H_2O_2 + Ag^{+} \longrightarrow HO^{-} + OH^{o} + Ag^{2+} \quad (4)$$

The Ag^{+} as Fe^{3+} is able to enhance the ROS formation via Fenton like reactions (4,5). The Ag^{2+} sputtered by HIPIMS is reported below in figure (8) as detected by 1) mass spectrometry in plasma and 2) XPS in Ag-polyester full fibers, and it will react:

$$Ag^{2+} + e\text{-}_{cb} \longrightarrow Ag^{+} \quad (5)$$

or by a two electron transfer mechanism from Ag^{2+} leading to Ag^{o} atoms:

$$Ag^{2+} + 2e^{-} \longrightarrow Ag^{o} \quad (6)$$

The Ag^{+} coalesce into the Ag^{o}-network with $E_{redox} = -0.79$ V vs. NHE. Reactions 3, 4 and 5 suggest electron transfer from the Ag to *E. coli* involving different Ag-structures and spatial separation of the surface redox sites due to the DCMS, DCMSP and HIPIMS with a different range of sputtering energies [23,62].

6. Inactivation time of *E. coli vs* nominal thickness of Ag-layers deposited by DMCS, DCMSP and HIPIMS-sputtering

Figure (5c) presents the trends for the complete inactivation time of *E. coli* vs the nominal thicknesses of Ag-layers deposited by DCMS, DCMSP and HIPIMS sputtering. This trend shows a significant reduction of the Ag-layers thickness required to inactive *E. coli* deposited by HIPIMS compared to Ag-layers deposited by DMCS and DCMSP.

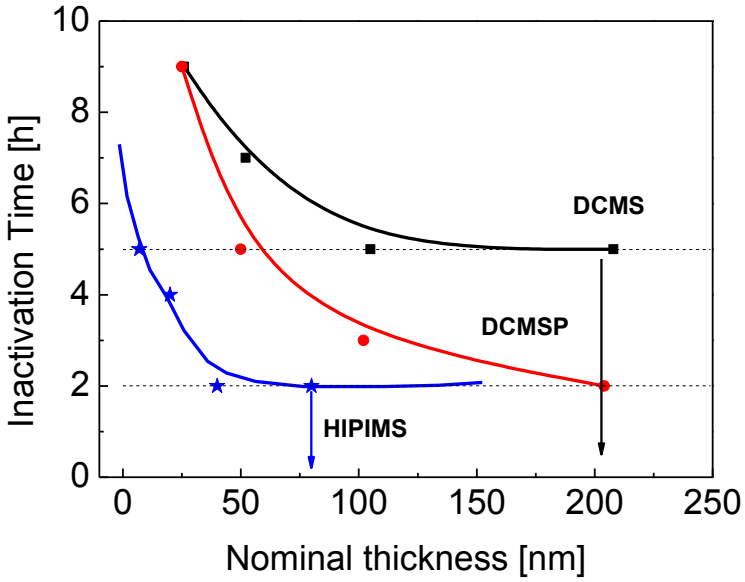

Figure (5c): Comparison of inactivation time of E. coli as a function of nominal thickness of Ag-layers deposited by DCMS, DCMSP and HIPIMS.

7. Diffuse reflectance spectroscopy of polyester coated samples by DCMSP

The rough UV-Vis reflectance data cannot be used directly to assess the absorption coefficient of the loaded polyester because of the large scattering contribution to the reflectance spectra. Normally a weak dependence is assumed for the scattering coefficient S on the wavelength. The values of KM/S for each sample in figure 6 are proportional to the absorption coefficient and parallel the bacterial inactivation kinetics for each sample shown previously in figure (4b).

In figure (6), the increase in Ag-sputtering time when going from 20s to 160s leads to an increase in the absorption peak around 400nm. This is due to localized surface plasmon resonance [192-194]. Sputtering for 160s introduces the most suitable Ag-level of 0.205 wt% /wt polyester. Sputtering for 20s loads the polyester with 0.0259 wt% /Ag/wt polyester. By XRD, as will be shown latter, no metallic Ag was found on polyester by due to the low amount of Ag-deposited on the polyester. Figure (6) presents in the inset the values of KM/S for Ag-sputtered by DCMS and DCMSP polyester samples for 160s. Since the Ag-absorption is similar in both DCMS and DCMSP, it is not the light absorption by Ag the determinant parameter for the bacterial inactivation kinetics but the different interfacial microstructure and species of Ag on polyester. These parameters will be reported by TEM and XPS in figures 8 and 11.

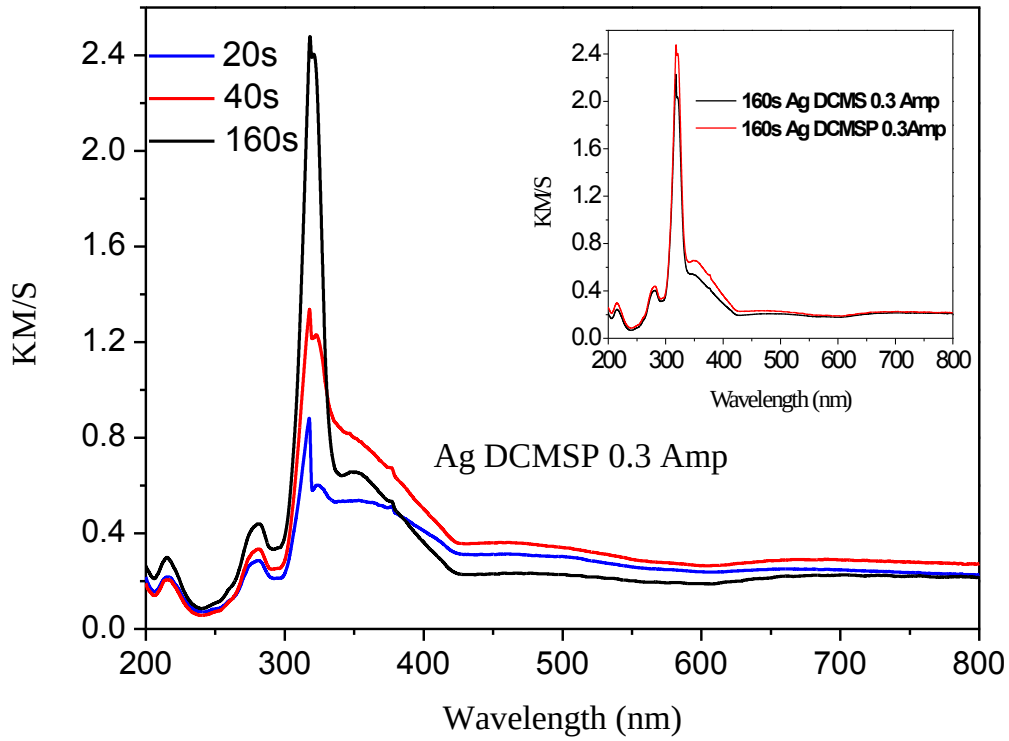

Figure (6): Diffuse reflectance spectra of Ag-sputtered on polyester for different deposition times.

8. Electron microscopy of the Ag-polyester full fiber sputtered by DCMS, DCMSP and HIPIMS

Figure (7a) presents the composite TEM results for Ag-polyester full fiber sputtered by DCMS for 160 s showing Ag-nanoparticles with sizes between 5 and 10 nm. The arrow on the right hand side indicates the direction of incidence from the Ag-target of the Ag-particles on the polyester. A continuous Ag-deposit 60–90 nm thick was observed. On the left hand side in figure (7a) a deposit comprising Ag-particles 5–15 nm was observed. E in figure (7a) stands for the Epoxide (glue) used during the preparation of the samples for TEM analysis. In figure (7a) about 40–50% of the perimeter of the full polyester fiber was covered by a 60–90 nm thick Ag-deposit. DCMS ion-energies have been reported between 10 and 20 eV and electron densities of ~10^{14}(e^{-}/m^{3}) [25].

Figure (7b) shows the composite TEM results for Ag-polyester full fiber sputtered by DCMSP for 160 s. The arrow on the lower side in figure (7b) indicates the direction of incidence of the Ag-particles on the polyester in the sputtering chamber. A dark continuous

Ag-deposit of 80–90 nm thick was observed. But only a 5–15 nm thick Ag-layer was found on the other end of the fiber figure (7b). About 65–70% of the full polyester fiber perimeter was covered by a 50–90 nm thick Ag-deposit. The DCMS Pulsed ion energies are much higher than the DCMS energies and DCMSP sputtering ion-energies of 10–100 eV have been recently reported with a small number of ions exceeding 100 eV and electron densities of~$10^{16}(e^{-}/m^{3})$ [25].

The electron microscopy (EM) results indicated that DCMSP-sputtering covered 65–70% of the perimeter of a polyester fiber with Ag compared to the coverage of 40–50% when sputtering with DCMS and this may explain in part the more favorable bacterial inactivation kinetics reported in figure (7b) compared with figure (7a) applying a 0.3 A current in both cases on the Ag 2-inches target. A larger Ag-coverage on the polyester fiber allows for: a) an increased transfer of electron/charges between DCMSP Ag polyester and the *E. coli* and b) a higher mobility of the Ag^{0}/Ag-ions on the fiber due to the higher energy applied compared to DCMS-sputtered fibers.

Figure (7c) shows the HIPIMS sputtered Ag-fiber at 5 A. The thick Ag-layer 80-120 nm coverage reaches up to 85-90% of the total fiber. In the bottom of the fiber a thin layer of Ag was observed. In the HIPIMS chamber, the Ag/Ag-ions reach the polyester fiber from all directions in the plasma chamber with ion-energies of ~30 eV and electron densities of ~10^{18} (e^{-}/m^{3}). HIPIMS is able to provide for a much higher number of Ag^{o} and Ag-ions compared to DCMS and DCMSP [21-23]. The increased kinetic energy of the Ag-ions and ion-flux in the plasma is due to the much higher power as compared to DCMS and DCMSP leading to an increase in the Ag-adatom mobility. This explains the results shown for *E. coli* inactivation in Figure (7b), that with lower Ag-polyester % Ag wt/wt polyester obtained by HIPIMS compared with DCMS and DCMSP, the *E. coli* inactivation was already complete within 2 hours.

In the magnetron sputtering chamber the reaction (1) lead in a subsequent step to the collision of the electron with Ag^{0} (2):

$$Ar \longrightarrow Ar^{+} + e^{-} \quad (1)$$

$$e^{-} + Ag^{0} \longrightarrow Ag^{+} + 2e^{-} \quad (2)$$

The high speed electron colliding with the Ag kicks off a second electron. The metal ionization is more favorable when higher currents (Amp) were applied during the DCMS or DCMSP sputtering. The ratio of Ag^{+}/Ag^{0} is higher for the DCMSP samples than in the case of the DCMS (Ag^{+}/ 1%-5% of Ag^{0}) samples [25, 63]. In the case of HIPIMS sputtering, the

electrons/ions in the chamber exists in the whole gas phase volume making it more likely to reach the entire polyester fiber and then leads high the Ag-coverage of polyester compared to the case of DCMS and DCMSP and the Ag^{+}/ 50%-90% of Ag^{0}) samples. The higher Ag-coverage by HIPIMS lead to a faster inactivation of *E. coli* as shown in figure (5c) compared to the samples sputtered by DCMS and DCMSP.

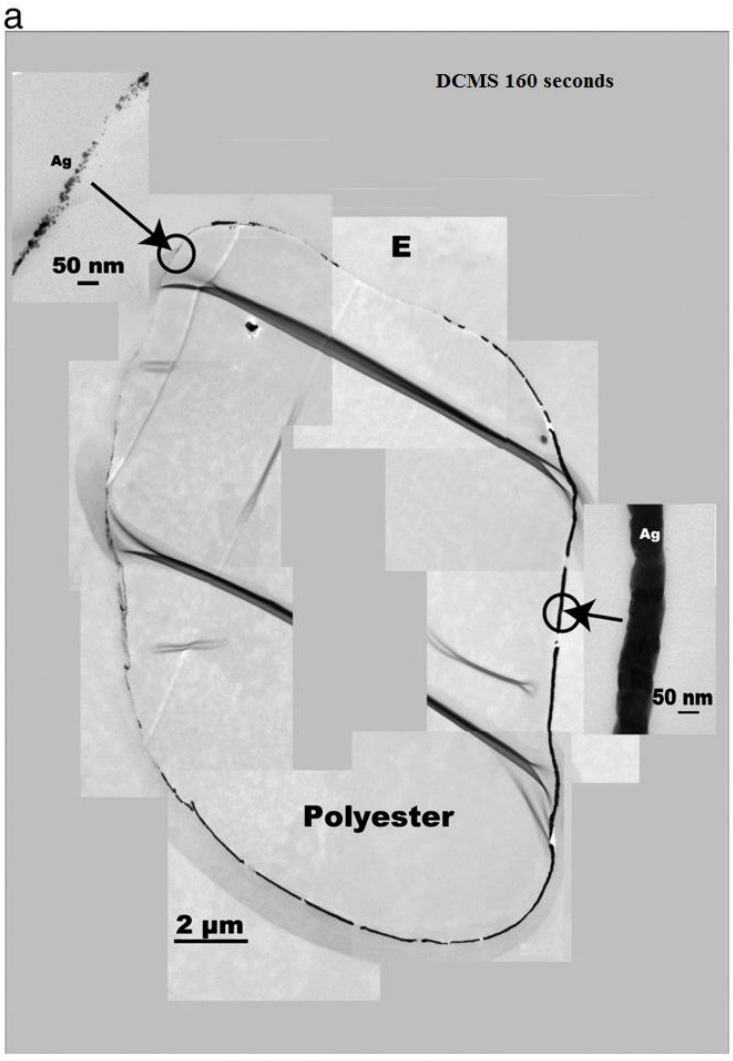

Figure (7 a): Electron microscopy (TEM) of Ag-polyester fiber DCMS sputtered for 160 s at 0.3 Amp

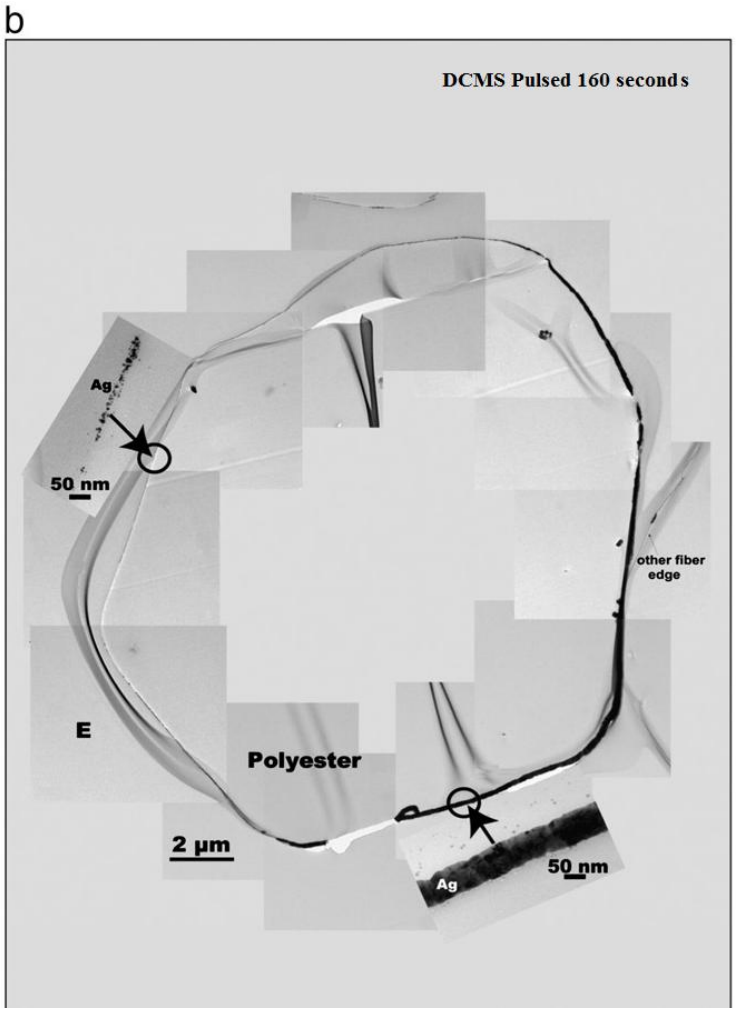

Figure (7 b): Electron microscopy of Ag-polyester fiber DCMSP sputtered for 160 s at 0.3Amp

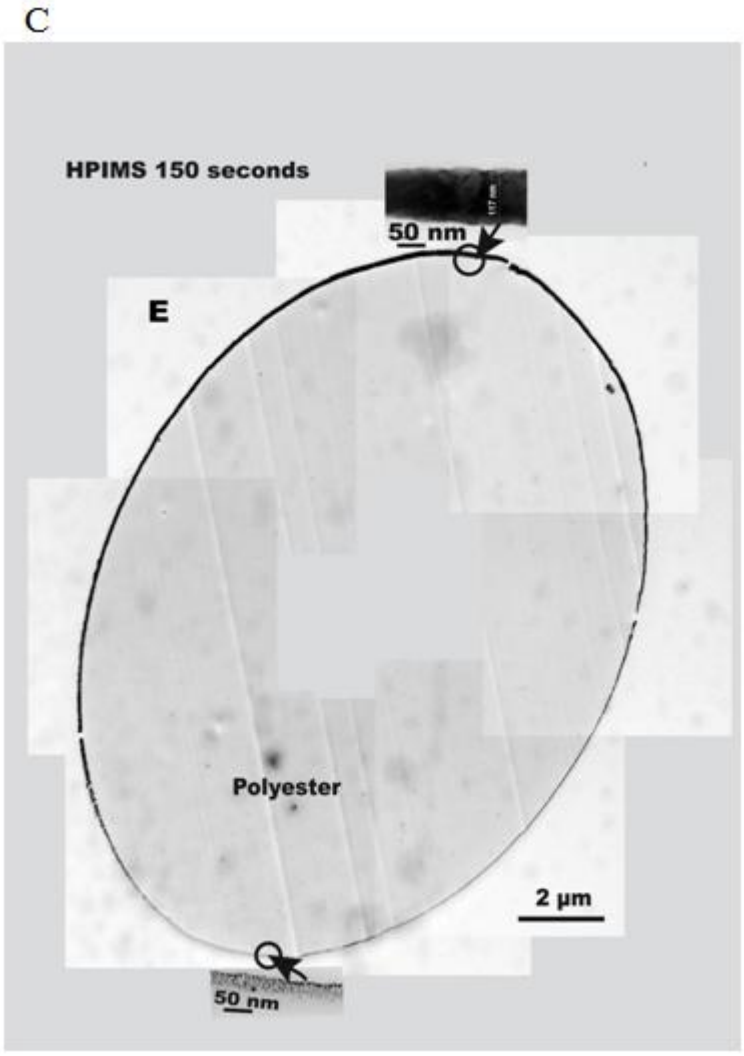

Figure (7c): Electron microscopy of Ag-polyester fibers sputtered by HIPIMS at 5Amps for 75s

9. Ag-ion and Ar-ion composition sputtered by HIPIMS and DCMS sputtering derived from mass spectroscopy analysis

Figure (8) presents the ion-composition when sputtering from the same Ag-target by DCMS and HIPIMS in Ar, derived from mass spectroscopy analysis. By inspection of figure (8), it is readily seen that the composition of the ions in the DCMS chamber gas phase was: 85% Ar^{+}, 8% Ar^{2+} and 4% Ag^{+}. The lowest % of Ag^{+}-ions was found for DCMS. The HIPIMS runs show that with increasing current the Ar^{+} decreases and the Ag^{+} gas phase increases. The amount of Ag-ions increased with peak HIPIMS discharge current. At discharge currents greater than 5 Amps, Ag^{+}-ions exceeded the amount of Ar^{+}-ions. The most interesting

result is that HIPIMS discharges at 5 and 10 Amps peak current produced high quantities of Ag^{+}- along a small amount of Ag^{2+}-ions.

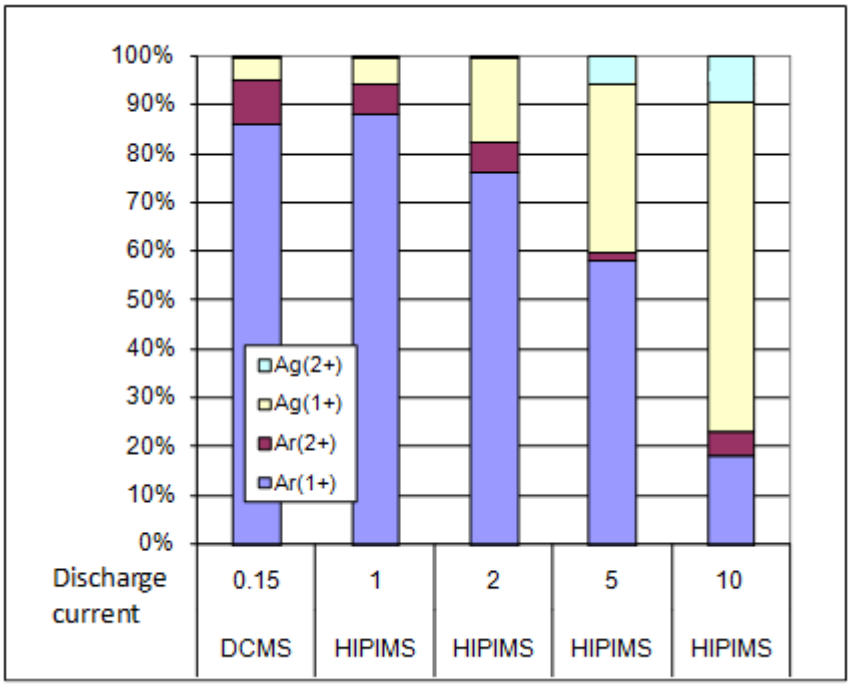

Figure (8): Plasma ion-composition analysis of HIPIMS and DCMS sputtering in Argon, derived from mass spectroscopy analysis. HIPIMS is applied at different currents as indicated in the Figure

10. X-ray diffraction of DCMS, DCMSP and HIPIMS sputtered Ag–polyester (XRD)

Figure (9a) shows the Ag-metallic peak at 2θ of 38° for Ag-nanoparticles on polyester sputtered by DCMS and DCMSP after 160 s at 0.3 A. Figure (9a) also shows that DCMS and DCMSP sputtering at 0.3 A for 20 s did not lead to Ag-metal formation.

Figure (9b) shows the XRD for Ag-nanoparticle films on polyester sputtered by DCMSP for 20 s and 160 s. The cluster formation occurs when Ag-atoms bind to other metal-atoms rather than to polyester. The growth of Ag-adatoms into clusters in the case of the 20 s sample leads to near spherical but not necessarily crystallography Ag-clusters. At a longer sputtering time of 160 s, a steep peak is observed in figure (9b) assigned to the Ag-metal peak at θ = 38°. Ag-metal nanoparticles have been reported with dimensions >1 nm [174].

HIPIMS sputtering for 13 s at 1 A indicate in the insert a low Ag-cluster formation. These clusters grow into bigger aggregates when sputtered for 75 s at 5 A, but did not lead to Ag-metal formation. More details describing the relation between the nano-crystallite particle

size and lattice parameters of silver clusters have been recently reported [190]. We have not looked in a detailed way into the effect of the microstructure changes introduced in the Ag-HIPIMS sputtered Ag-particles for 75 s at 5 A leading to the formation of a thick 40 nm film compared to a thin 4 nm film sputtered for 13 s at 1 A.

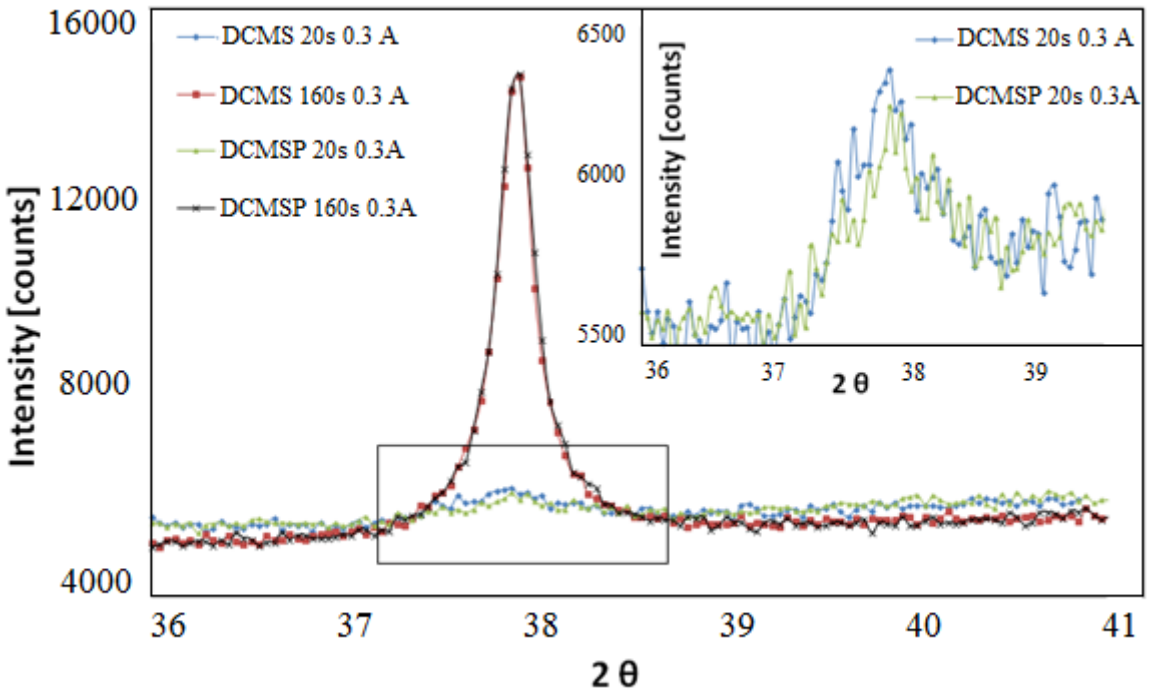

Figure (9a): X-ray diffraction of Ag polyester sputtered by DCMS and DCMSP at 0.3 Amp for 160 s and 20 s. For other experimental details see text.

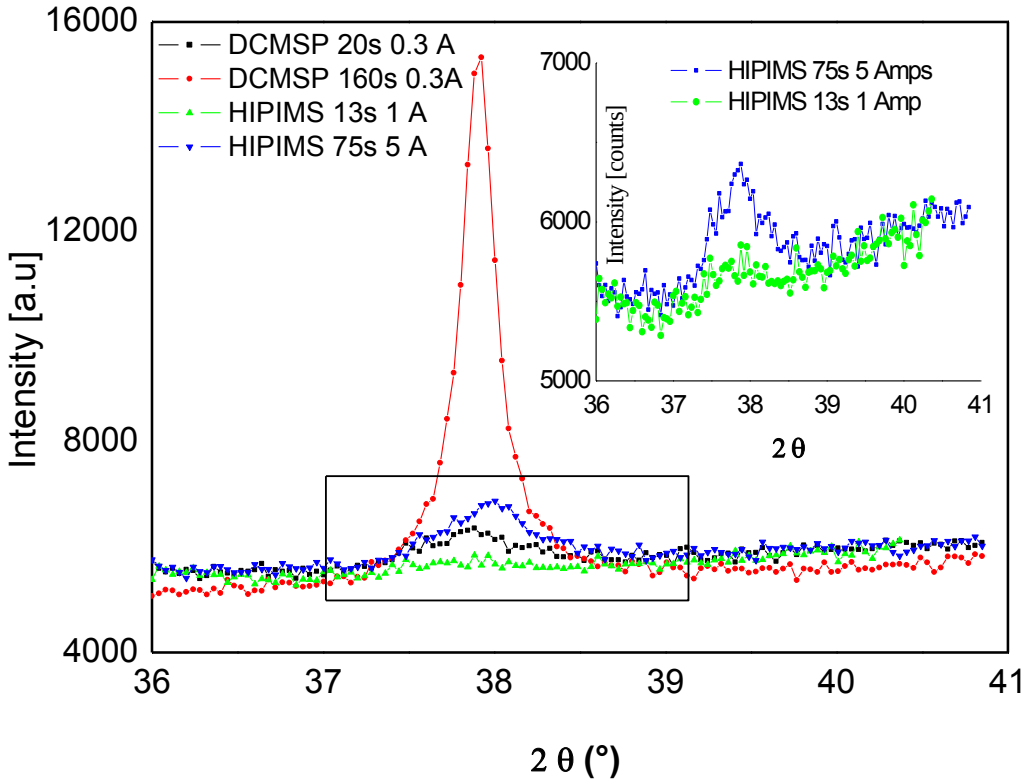

Figure (9b): X-ray diffraction of DCMS and HIPIMS sputtered Ag–polyester fibers sputtered under different conditions.

11. X-ray photoelectron spectroscopy of Ag-polyester samples (XPS)

Table 2 shows the variation of the surface atomic concentration percentage of O, Ag and C for polyester DCMS and DCMSP sputtered samples at times of 80 s and 160 s. The Ag increase with sputtering time induces a concomitant decrease in the C-loading and the O-loading on the sample due to coverage Ag-polyester. Table 3 shows the percentage atomic composition for samples etched with 5 keV Ar-ions reporting that Ag-penetrates up to 15 nm in the polyester fiber during the sputtering process. For the 20 s sputtered 0.05 A DCMS-sample, the deeper we go into the fiber, the less Ag was found, and more C was found as the main polyester component. This pattern was not observed for the samples 20 s, 0.3 A DCMSP. A variable amount of Ag was observed as a function of sputtering depth and still a 39.6% Ag-loading was present at 15 nm. A higher percentage of Ag was observed as a function of sputtering depth for the DCMSP-samples 160 s, 0.3 A and in this case the percentage Ag-concentration was seen to increase drastically as function of fiber depth reaching values up to 90.4%. This last sample intervened kinetically fast in *E. coli*

inactivation. This may due to the large amount of exposed Ag-catalytic sites on the Ag-nanoparticles able to interact effectively with *E. coli.*

Table 4 shows the composition of the main elements within the upper layers (~2 nm) of the Ag-polyester for the 160 s DCMSP-samples sputtered at 0.3 A. The surface Ag % is seen to drastically decrease as function of the *E. coli* inactivation time at the expense of an increase in the C-content. This is due to C-residues left by the dead bacteria during the *E. coli* inactivation process. C-residues left by the dead bacteria have to be eliminated on the Ag-polyester surface to be able to attain repetitive destruction of microbes since we need a clean surface before a new inactivation cycle. On the other hand, the antimicrobial activity of Ag is dependent on the Ag^{+}-cation strongly binding to the electron donor groups S, O and N of the bacterial cell wall.

The information for the X-ray photoelectron spectroscopy for HIPIMS sputtered Ag–polyester is shown next in Tables 5 and 6. Table 5 shows the atomic surface concentration of O, C and Ag for the HIPIMS sputtered sample for 75 s at 5 A. The increase of the surface O is due to the appearance C–OH, C–O–C and carboxyl species as shown quantitatively in Table 6. This observation confirms the growth of oxygen functionalities as the bacterial inactivation times become longer [51, 195]. Figure (7c) of the Ag-HIPIMS sputtered fiber shows that no homogeneous coverage of the polyester by Ag occurs. The O and C atoms of the polyester contribute therefore significantly to the atomic % concentration determined by XPS as presented in Table 5. Concomitantly, the C-content increases with reaction time and the Ag on the topmost 10 surface layers (~2 nm) is seen to decrease due to the C-residues left by the inactivated bacteria on the polyester surface.

Table 6 shows the peaks area of the C–C species (including the reduced C-forms C=C, C–H) with (BE) of 285 eV and the deconvoluted oxidized C-forms: C–OH, C–O–C and carboxyl functionalities with BE at 286.1 eV, 287.0 eV and 289.1 eV [196]. The increase in the ratio of the (C–OH+C–O–C+carboxyl peak areas) to the C–C concentration as shown in figure (10) was: 0.62 at zero time polyester contact with bacteria: 0.68 (at 30 min), 0.76 (at 60 min), 1.22 (at 90 min) and 1.33 (at 120 min) within the E. coli inactivation time [197]. The bacterial destruction process induces a progressive decrease of the C–C species in the polyester within time the bacterial inactivation since the oxidation of the *E. coli* gives raise to formaldehyde and short-chain organic acids that spontaneously decarboxylate generating CO_2. This has been known for the last 40 years [3, 8,16] and references therein.

Table 2: Atomic percentage composition of Ag-polyester sputtered by DCMS and DCMSP as function of sputtering time

Sample Identifier	Name	Position (eV)	% at Conc
zero s	O 1s	530.2	24.07
	Ag 3d	373.4	0.04
	C 1s	282.9	75.2
80 s DCMS	O 1s	531.4	9.2
	Ag 3d	368.4	27.2
	C 1s	284.9	63.6
160 s DCMS	O 1s	530.7	5.6
	Ag 3d	368.5	38.1
	C 1s	285.0	56.2
80 s DCMSP	O 1s	530.6	6.0
	Ag 3d	368.5	35.8
	C 1s	285.0	58.2
160 s DCMSP	O 1s	530.7	4.9
	Ag 3d	368.6	38.6
	C 1s	285.1	56.5

Table 3: Atomic percentage concentration of Ag-polyester etched by 5 keV Ar-ions as a function of etching time and depth by DCMS/DCMSP sputtering.

Etching time (s) And depth (nm)	Name	% at Conc 20 s, 0.05 Amp DCMS	% at Conc 20 s, 0.3 Amp DCMSP	% at Conc 160 s, 0.3 Amp DCMSP
zero	O 1s	15.5	7.4	6.4
	Ag 3d	21.1	36.2	41.9
	C 1s	63.5	56.4	51.6
60 (3 nm)	O 1s	7.8	4.4	0.9
	Ag 3d	14.8	65.6	87.7
	C 1s	77.4	30.1	11.5
180 (9 nm)	O 1s	4.8	3.1	0.5
	Ag 3d	9.4	48.0	92.9
	C 1s	85.8	48.9	6.6
300 (15 nm)	O 1s	4.6	1.9	0.7
	Ag 3d	8.0	39.6	90.4
	C 1s	87.4	58.5	8.9

Table 4: Evolution of the surface percentage atomic concentration of Ag polyester during the *E. coli* inactivation for DCMSP 0.3 A sputtered sample

Sample Identifier 160s, 300mA DC Pulse	Name	% At Conc
0 min	Ag 3d	38.6
	O 1s	4.9
	C 1s	56.5
30 min	Ag 3d	15
	O 1s	17
	C 1s	68
60 min	Ag 3d	12
	O 1s	18
	C 1s	70
120 min	Ag 3d	7
	O 1s	21
	C 1s	72

Table 5: Atomic percentage surface concentration of Ag, O, and C on HIPIMS sputtered polyester as a function of time during *E. coli* inactivation.

	time	element	% At Conc
HIPIMS 75 s, 5Amps	0 min	O 1s	14
		C 1s	52
		Ag 3d6	34
	30 min	O 1s	19
		C 1s	56
		Ag 3d6	25
	120 min	O 1s	25
		C 1s	72
		Ag 3d6	3

Table 6: Evolution of the C-C species and the oxidized species (C-OH, C-OC, carboxyl) on Ag–polyester sputtered for 75 s at 5 A with HIPIMS.

	time	functionality	Peak Position (eV)	Area	% Conc.
HIPIMS 75 s 5Amps	0 min	C-C	285.0	2902.5	61.7
		C-OH	286.1	786.4	16.7
		C-O-C	287.0	543.2	11.5
		carboxyl	289.1	474.0	10.1
	30 min	C-C	285.0	2553.5	59.9
		C-OH	286.1	779.25	17.9
		C-O-C	287.0	443.3	10.3
		carboxyl	289.1	520	12.5
	60 min	C-C	285.2	2211.1	56.8
		C-OH	286.3	772.1	19.8
		C-O-C	287.1	343.4	8.8
		carboxyl	289.0	566.0	14.5
	90 min	C-C	285.0	1690.6	38.5
		C-OH	286.8	911.2	20.8
		C-O-C	288.1	532.3	12.1
		carboxyl	289.3	616.9	14.1
	120 min	C-C	285.0	1470.2	32.7
		C-OH	286.1	970.3	21.1
		C-O-C	287.3	290.5	6.7
		carboxyl	289.2	550.2	14.3

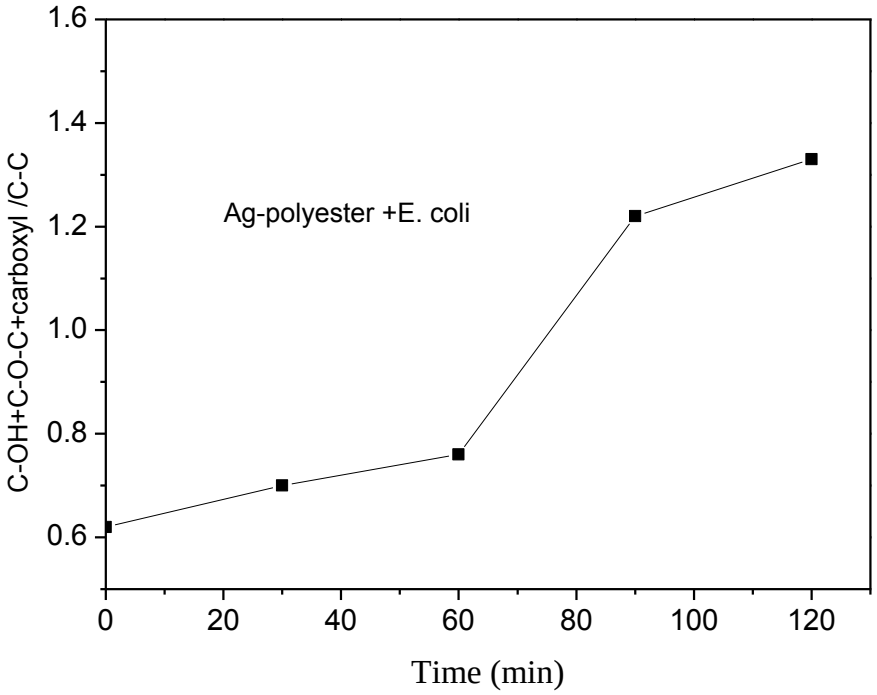

Figure (10): Ratio of oxidized carbon and reduced carbon (C-O+C-O-C+carboxyl/C-C) on Ag-polyester (HIPIMS 75s, 5A) samples in presence of *E*. coli

11.a. XPS spectra investigation

A survey scan XPS spectrum of Ag- nanoparticles sputtered on the polyester a) DCMS (160s, 0.3 Amp), b) DCMSP (160s, 0.3 Amp) and c) HIPIMS (150s, 5 Amps) in the range of binding energies 0–1100 eV is shown in figure (11). Original single peaks of Ag 3d high-resolution XPS spectra are doubled, and these peak positions change a little with elapsed time. The shift of the ordinary peaks is calibrated with respect to the C 1s peak position set at 284.6 eV.

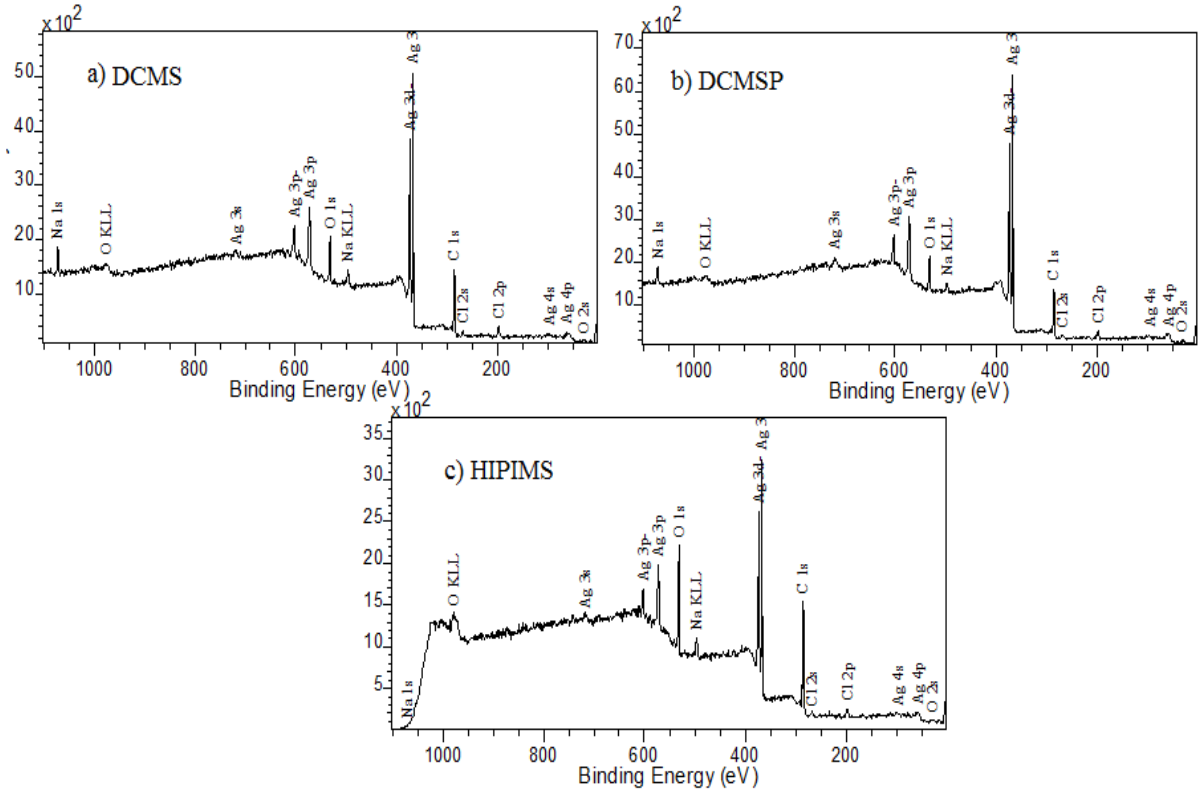

Figure (11): (a) Survey scan XPS spectra in the binding energy range 0–1100 eV (O 2s; Ag 4p; Ag 4s; C1 2p; C1 2s; C 1s; Ag 3d; Ag 3p; O 1s; Ag 3s, O KLL), where KLL represent the Auger transition

Two types of Ag were deposited by the DCMS, DCMSP and three types by HIPIMS as shown in figure (11) with Auger parameters at 725.15, 725.53 and 725.65 eV and are assigned to Ag^{0}, Ag^{+1} and Ag^{+2}, in sequential order. While the presence of Ag^{0} and Ag^{+2} seems to be documented, the assignment to Ag^{+2} is less clear.

Figures (11a), (11b) and (11c) show the high resolution XPS spectra, of Ag DCMS, DCMSP (160s, 0.3 A) and HIPIMS sputtered polyester (150s, 5 A), of the deconvoluted Ag-doublet analyzed in terms of the Ag^{0}, Ag^{+} and Ag^{2+}components. The binding energies (BE) of Ag $3d_{5/2}$ and Ag $3d_{3/2}$ for silver NPs are shown in figures (10a, b and c). The Ag 3d spectrum exhibits peaks at 368.2 eV (3d5/2) and 374.3 eV (3d3/2), which correspond to that of silver in the zero valence state Ag^{0} [198, 199] for all DCMS, DCMSP and HIPIMS.

The Ag^{+} peak is noted in figure (11b, c) at 367.5 eV and 367.7 eV successively, and the small Ag^{2+} peak at the right hand side in figure (10c) at 367.3 eV have been assigned according to Abe [198], Weaver [200, 201] and Chiu [202]. The various redox potentials available at the Ag- surface are due to the different oxidation states for Ag. More important, the amount of Ag for the 160 s DCMS and DCMS Pulsed sample seem to be close in values

(0.178% w/w and 0.205%w/w successively) as said before but the bacterial inactivation kinetics in DCMSP show faster than DCMS. Nevertheless, by checking in figure (5c), in the same Ag-layers thickness sputtered by HIPIMS, DCMSP and DCMS, the kinetics of inactivation bacterial in the case HIPIMS show more faster than DCMSP and DCMS successively. Therefore, Ag^0 is not the main active responsible for the *E. coli* inactivation but the ionic species seem to be the species leading to bacterial deactivation as described in figures (11b, c).

The bacterial inactivation of *E. coli* may be due to: (a) surface polyester Ag-clusters and (b) protected Ag-clusters inside the polyester fabric. The top most surface Ag-layers in the open structure of the polyester fabric would protect the interior lying Ag-layers with ionic species interacting with *E. coli*. This provides additional stability for the internal Ag-clusters during the E. coli inactivation process. The overall charge of the *E. coli* is negative between pH 3 and 9, due to the predominant carboxylic external groups of the bacterial cell wall. These carboxylic and other negative functional groups upon dissociation in aqueous solution make the cell wall negative. The opposite charge on the bacteria and the Ag positive-ions as shown in figures (11b, c) seem to induce to a tight binding of the Ag-clusters to the bacterial surface.

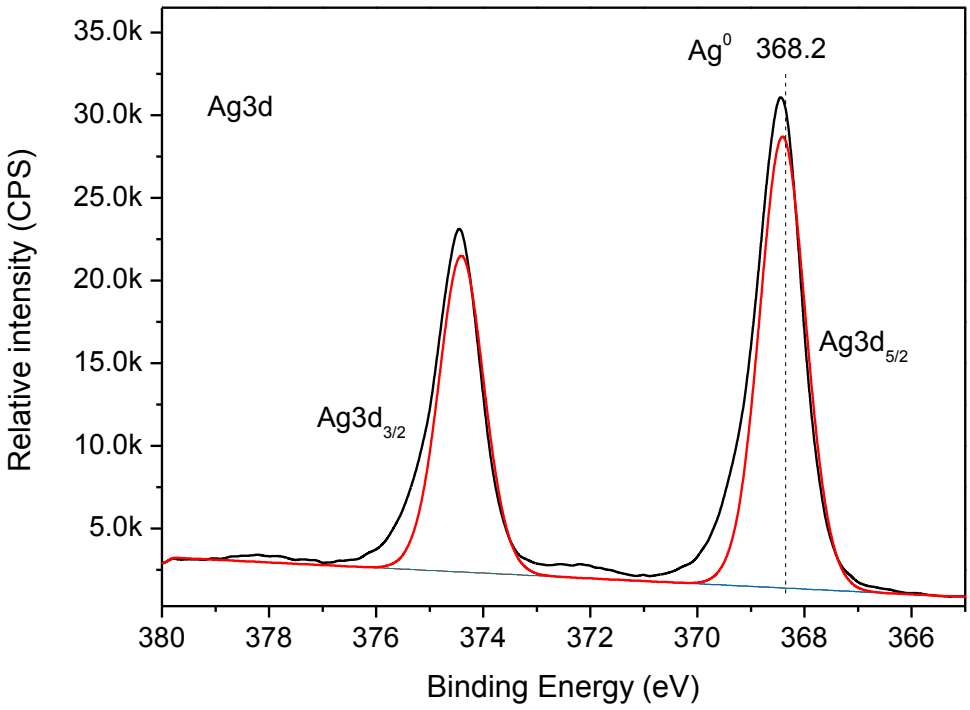

Figure (11a): High resolution XPS spectra of Ag DCMS sputtered polyester (160s, 0.3 A) showing the deconvoluted peaks for the Ag species.

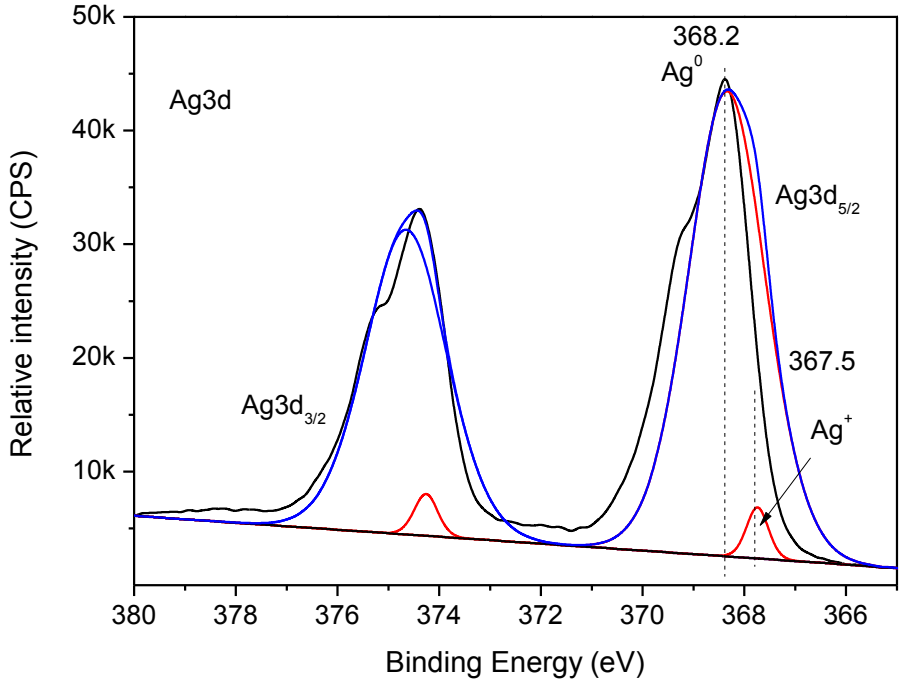

Figure (11b): High resolution XPS spectra of Ag DCMS Pulsed sputtered polyester (160s, 0.3 Amp) showing the deconvoluted peaks for the Ag-ionic species (Ag^{+}).

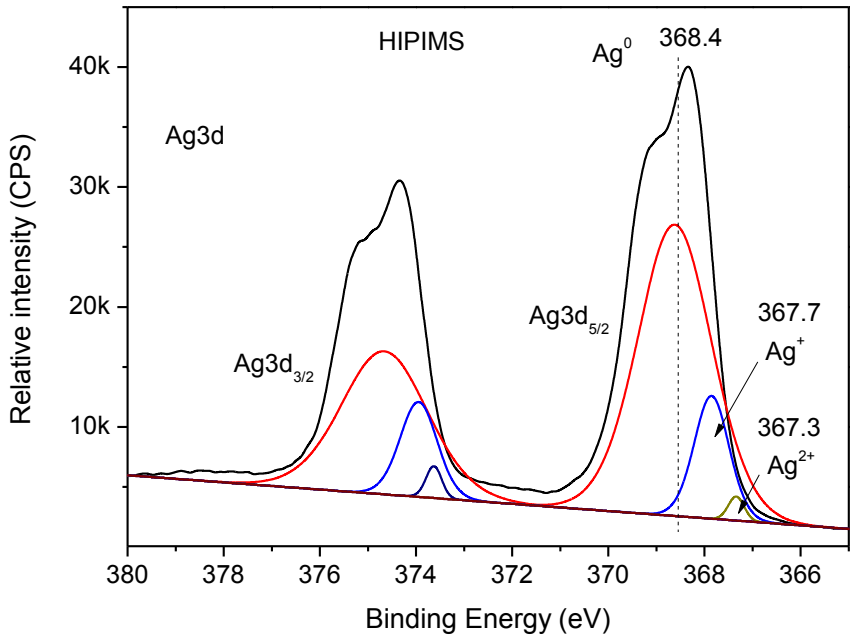

Figure (11c): High resolution XPS spectra of Ag HIPIMS sputtered polyester (150s, 5 A) showing the deconvoluted peaks for the Ag-ionic species (Ag^{+}, Ag^{2+})

Figure (12) shows the $Ag3d_{5/2}$ peak stepwise shift from 368.1 eV to 368.8 eV assigned to the shift from Ag^{o} to $Ag^{1+/2+}$ ionic species within 120 min during *E. coli* inactivation on a Ag-polyester sputtered 150s (HIPIMS, 5 A) sample [8,181]. The XPS shift lies in the region related to the oxidation states between Ag^{o} and Ag^{2+}. Since these shifts were negatively observed by XPS on the upper polyester modified layers this is indicative for the presence of Ag ions layers located mainly at the Ag-interface.

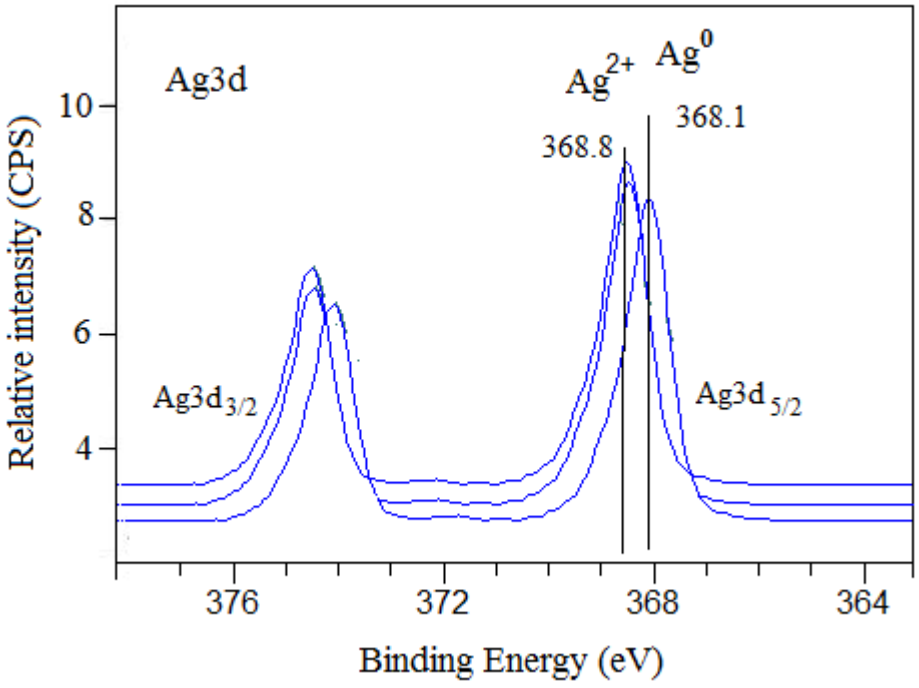

Figure (12): Ag3d5/2 shift between times zero and 120 min during *E. coli* inactivation on Ag-polyester sputtered 150s (HIPIMS, 5 A).

12. Contact angle measurements and droplet adsorption times (CA)

Figure (13) presents in the upper row the contact angle of polyester of 179.9° for polyester alone (void areas, 10 μm pore sizes) due the hydrophobic nature of polyester. The DCMSP-sputtered samples for 80 s show a hydrophobic contact angle of 108.5°. But this is a lower hydrophobicity compared to the contacted angle for polyester alone was due to the Ag-ions sputtered by DCMSP sample as identified by infrared spectroscopy [203,204] and by XPS [51]. At 160 s DCMSP-sputtering an increase in the hydrophobicity is related to the 2 times increase in the Ag-loading (Table 1) introducing a high amount of hydrophobic Ag^{0}.

The void area due to the polyester fabric porosity is reduced during the Ag-sputtering decreasing the water contact at longer sputtering times. The same trend for the contact angle was observed in the second row in figure (13) for the HIPIMS-sputtered samples. But comparing the contact angle of HIPIMS-sputtered samples to DCMSP, a lower hydrophobicity is induced by HIPIMS due to the higher amount of Ag ions identified by XPS.

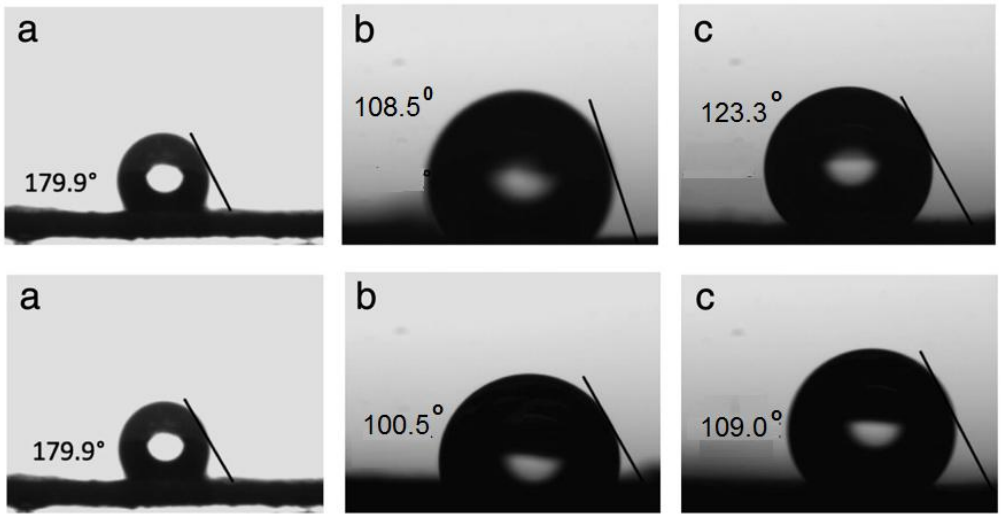

Figure (13): Contact angle for DCMSP-sputtered Ag-polyester samples

Upper row: a) polyester alone, b) DCMSP-sputtered samples for 80s and c) DCMSP-sputtered samples for 160 s. at 0.3 A.

Lower row: a) polyester alone, b) HIPIMS-sputtered samples for 75s and c) DCMSP-sputtered for 150 s. at 5 A.

13. Conclusions

• The most effective *E. coli* inactivation by DCMS and DCMSP sputtered for 160s had Ag-loadings ~3 times higher than the loading obtained by HIPIMS after 150s of 0.0630 %Ag wt/wt polyester.

• Low Ag-content in the films sputtered by HIPIMS gives more effective *E. coli* inactivation compared to those sputtered by DCMS and DCMSP. The material saving of non-renewable Ag is shown in this study.

• HIPIMS sputtered Ag-nanoparticles provide a high polyester fiber surface coverage. This allows for a greater interaction surface which accelerates the bacterial inactivation compared to DCMS and DCMPS-sputtered polyester.

• The HIPIMS deposited Ag-nanoparticle fibers present a different microstructure compared to DCMS and DCMSP sputtering. This allows the bacterial inactivation to proceed in similar times compared to DCMS and DCMPS-samples in spite of having a much lower loading of Ag/cm^2.

• By HIPIMS an important material savings for nonrenewable resources of industrial importance like Ag was possible.

• The Ag-films obtained by DCMS and DCMSP on the polyester show a narrow size distribution and metallic character as determined by XRD. The Ag-ion deposition with HIPIMS proceeds with a higher percentage of single and double Ag ions compared to deposition by DCMS and DCMSP.

Chapter 6 :Antibacterial Zr-Ag-N surfaces promoted by Subnanometric ZrN-clusters deposited by reactive pulsed magnetron sputtering

1. Sputtering of ZrN under layers and Zr-Ag-N films.

The calibration of the ZrN and Zr-Ag-N film thickness deposited by DCMSP on Si-wafers are shown in figure (1). The film thickness was determined with a profilometer (Alphastep500, TENCOR) and the values presented an error of ±10%. The layers of ZrN were sputtered by DCMSP and taking 10^{15} atoms/layer/cm^2 being each layer 0.2 nm thick [189], makes within 5 min in figure (1), a thickness of 110 nm with 5.5× 10^{17} atoms/cm^2. This data allows the estimation of a deposition rate of 1.8×10^{15} ZrN/cm^2 s. The Ag was then co-sputtered with the Zr under layers by DCMSP reactive since recent work in our laboratory and in previous chapter 5 showed a faster bacterial inactivation of *E. coli* by DCMSP compared with DCMS-deposition [68]. The values of the thicknesses of the Ag-film as a function of DCMSP sputtering time at 0.3 A is shown previously (in Table 1, chapter 5 up to 160 s). Figure (1) indicates that using a current of 0.3 A a thickness of 180 nm was attained after 80 s. The standard deviation in figure (1) for the Zr-Ag-N layers calibrated on Si-wafers was ±10%. Within 1 s 1.2–1.25 nm film Ag was deposited equivalent to ~6 layers of 0.2 nm each leading to a rate of Ag deposition of 6 $\times10^{15}$ atoms/cm^{2}s if taking in the lattice distance of 0.3 nm between Ag-atoms [23]. A film obtained by sputtering is always less dense than the bulk material, so probably the indicated thickness is lower than the real thickness.

A ZrN-coating thickness of 220 nm was sputtered within 600 s at 290 mA. The co-sputtered Zr-Ag-N layers leads to a 1200 nm thickness within 600 s. This film is thinner than the film obtained by co-sputtering sequentially Ag- with ZrN on polyester indicating the formation of hybrid composite Zr-Ag-N layers.

The Ag- and Zr-content of the polyester sputtered samples was determined by X-ray fluorescence. Table 1 shows that the Ag content as a function of sputtering time at 0.05 Awas low for Ag and only increased toward 20 s. For Zr, the values found were almost constant or below the detection level of the instrument of 0.0010% Zr wt/w polyester. An increased Ag-deposition was attained sputtering at 0.3 A up to 20 s, depositing about 8 times more Ag 20 s than when 0.05 A was used. This is not surprising since at higher energies (currents) as applied by DCMSP a higher density flux of metal-ions/metal nanoparticles with energies >10 eV and up to 100 eV has been reported recently by Lin et al. [25].

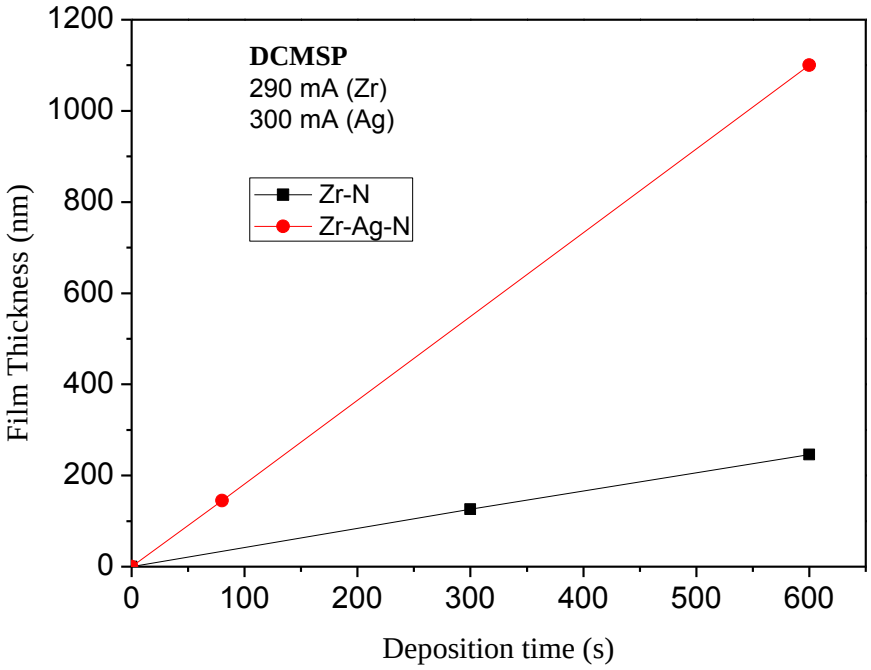

Figure (1): Calibration of Zr-N and Ag in the Ag–ZrN film sputtered at 300 mA for Ag and 290 mA for Zr on Si-wafers.

Table 1: X-ray fluorescence determination of percentage weight Zr and Ag per weight polyester in DCMSP sputtered Zr- Ag-N polyester.

Sample Zr- Ag-N-Polyster -DCMSP-	time (s)	% Ag wt/wt polyester	% Zr wt/wt polyester
50 mA (0.05Amp)	2	0.0010	0.0010
	5	0.0010	0.0010
	10	0.0010	0.0010
	20	0.0012	0.0010
300 mA (0.3 Amp)	2	0.0018	0.0010
	5	0.0020	0.0010
	10	0.0067	0.0011
	20	0.0105	0.0012

2. Ag-films visual appearance as a function of sputtering time

The polyester in Photograph (2a) shows no color in the absence of Zr-Ag-N. A light gray-color appears in sample (b) indicative of Ag clusters/nanoparticles deposited at 0.05 A for 10 s, (c) shows a darker gray Ag-color due DCMSP applied 2 s at 0.3 A and finally (d) shows a dark mostly Ag-deposit on the Ag–ZrN-polyester sputtered for 20 s at 0.3 Amp. The Ag- migration/aggregation of the Ag-particles is driven by the sputtering energy leading to thermodynamically stable agglomerates [93]. The color in Photograph (2d) corresponds to the Ag_2O/Ag^o with a band-gap (bg) 0.7–1.0 eV. This allows for an absorption edge up to about 1000 nm for the silver deposited on the polyester [205] as shown in Figure (2)

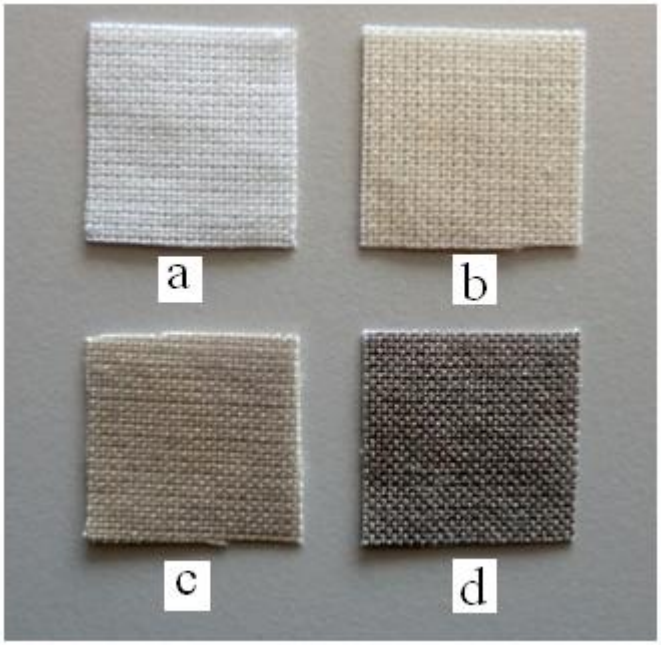

Photograph (2): Visual appearance of Zr-Ag-N polyester sputtered under different experimental conditions: (a) polyester alone, (b) DCMSP Zr-Ag-N films 10 s at 50 mA, (c) DCMSP Zr-Ag-N films 2 s at 300 mA, and (d) DCMSP Zr-Ag-N films 20 s at 300 mA.

3. *E*. coli bacterial inactivation kinetics

Figure (3a) presents the *E. coli* inactivation kinetics when Zr was sputtered in an Ar + N_2 (0.5 Pa) atmosphere on polyester in the dark. When applying sputtering times of a few seconds no the bacterial inactivation was observed and by TEM analysis revealed no Zr-particles. These Zr-particles therefore had sizes <1 nm. Sub-nanometric particles of Fe and

other metals presenting catalytic effects have been reported by our laboratory as being effective in the degradation of organic compounds [206,207]. Only the ZrN samples sputtered for 15 min presented bactericide properties. This observation will be discussed in the context of the results presented for the inactivation of *E*. coli by the Zr-Ag-N-polyester in figures (3b–d).

The formation of ZrO_2 can be understood in terms of: a) the partial oxidation of ZrN takes place in the presence of an oxygen source due to the residual H_2O vapor in the sputtering chamber at the residual pressure $Pr=10^{-4}$ Pa. This pressure is equivalent to 10^{15} molecules/cm^2s; there are sufficient O-radicals available to induce partial oxidation of ZrN films [68,208] and b) the films can oxidize after the deposition when exposed to air and during the sterilization process (autoclaving at 121 °C).

Figure (3b) presents the experimental results for polyester coated by Zr and Ag confocal sputtering in Ar + N_2 atmosphere for 2 s, 5 s, 10 s and 20 s with at 50 mA (0.05 A). It is readily seen that polyester alone has no bactericide action and that the *E. coli* inactivation kinetics becomes faster at longer sputtering time due to the increased Ag-particle density attained with longer sputtering times. Trace (6) shows that when Ag is sputtered alone for 20 s, 9 h were necessary to inactivate *E. coli* compared to a 2.5 h inactivation period observed when Ag and Zr were sputtered simultaneously for 20 s at 0.05 A. Figure (3b) shows that Zr-Ag-N polyester samples containing a ZrN nanocomposite with Ag are more effective in *E. coli* inactivation compared to the Ag-nanoparticles by themselves.

Figure (3c) presents the faster inactivation kinetics attained by Ag/Zr targets applying currents of 0.3 A. Figure (3c) shows an E. coli inactivation time of 1.5 h on Ag/Zr polyester sputtered for 20 s. Trace (5) in Fig. 3c indicates that *E. coli* inactivation is a complex process. We suggest that this sample had the optimal ratio of Ag-loading/Ag cluster size with the highest amount of Ag-sites held in exposed positions active in the *E*. coli inactivation process. Table 1 indicates that the amount of Ag sputtered at 20 s was ~8 times higher applying 0.3 Amp compared to 0.05 A. Ag sputtered alone as a control experiment in figure (3c) indicates an *E*. coli inactivation time of ~9 h. This shows the favorable effect of the ZrN during on the Ag-clusters during bacterial inactivation process.

Figure (3d) shows that for samples sputtered under and above 20 s, the *E*. coli inactivation kinetics became slower compared to samples sputtered for 20 s. The Ag-

agglomerates becomes bigger but the catalytic activity per exposed atom decreased due to the Ag-agglomeration process [209]. At times below 20 s, there was not enough Ag on the polyester to mediate the *E*. coli inactivation as shown in Table 1 by the X-ray fluorescence data.

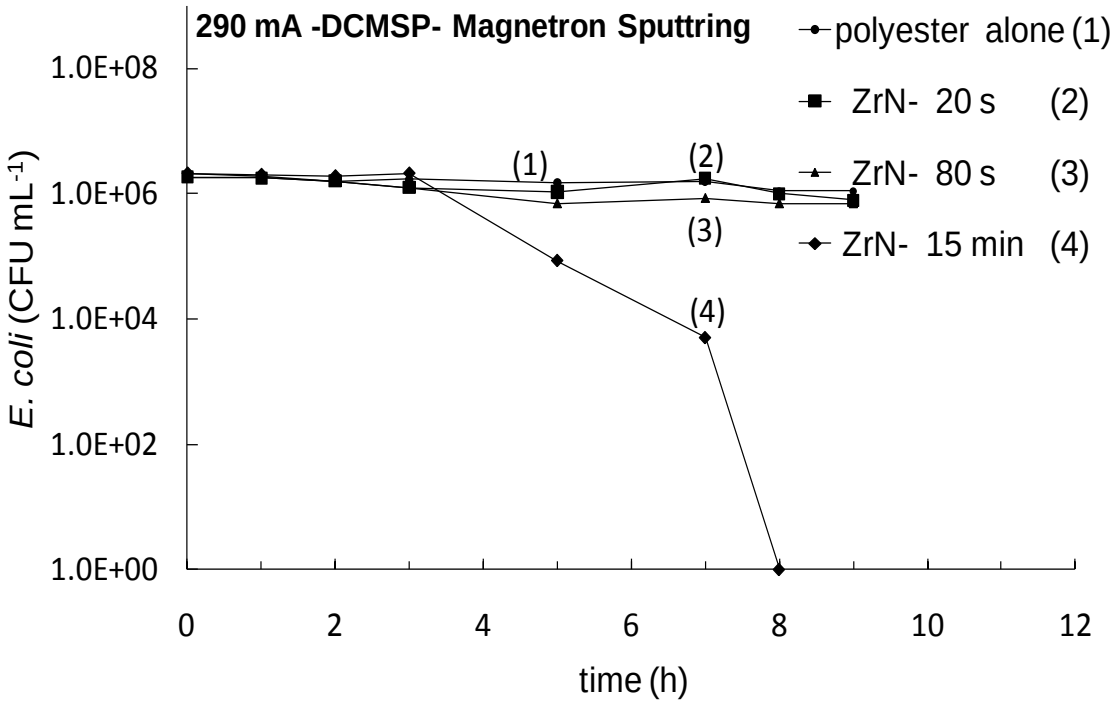

Figure (3a): *E*. coli inactivation prepared by polyester by direct current magnetron sputtering (pulsed) for different times with Zr in (Ar + 10% N_2 0.5 Pa) atmosphere at 290 mA.

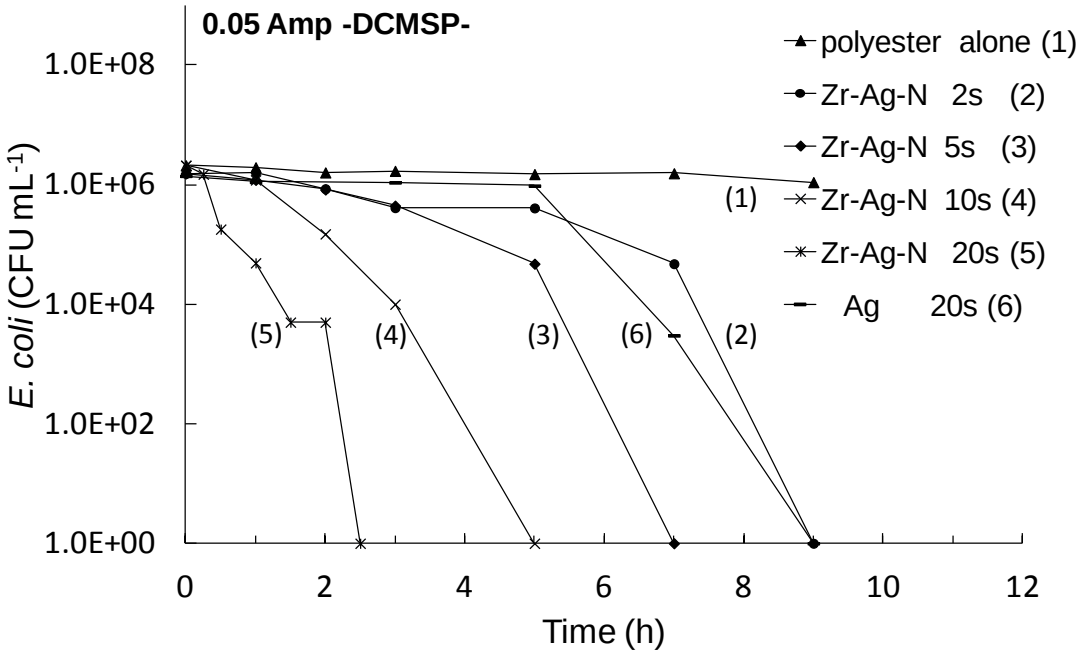

Figure (3b): *E*. coli inactivation prepared by polyester confocal direct current magnetron sputtering (pulsed) for different times using an Ag- and Zr-target in (Ar + 10% N_2 0.5 Pa) atmosphere at 0.05 A.

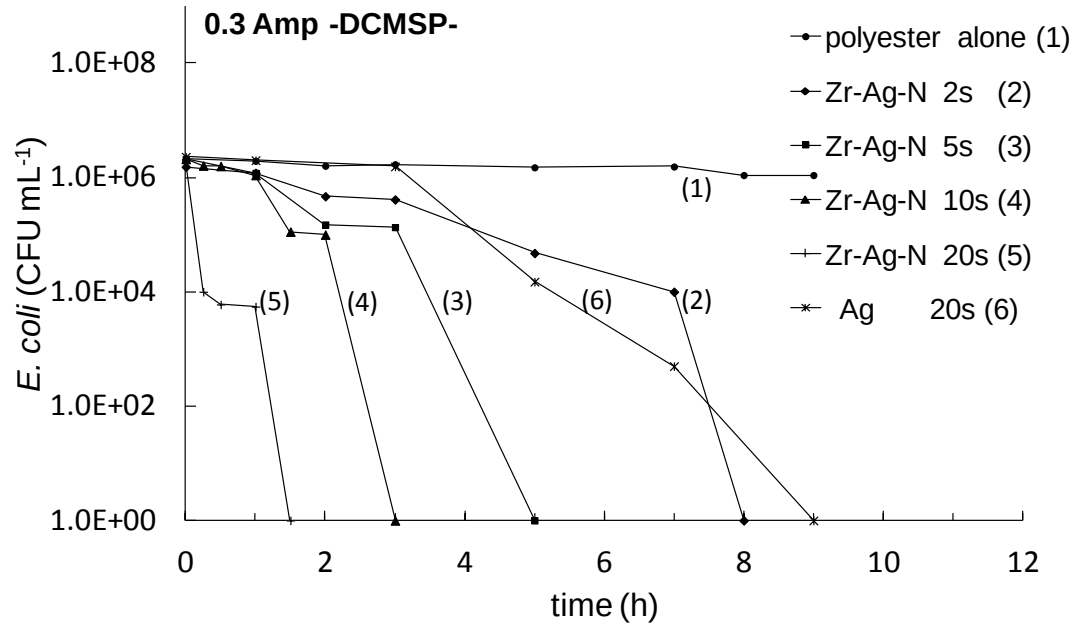

Figure (3c): *E*. coli inactivation on polyester sputtered by DCMSP at different times using an Ag- and Zr-target in (Ar + 10% N_2 0.5 Pa) atmosphere at 0.3 A

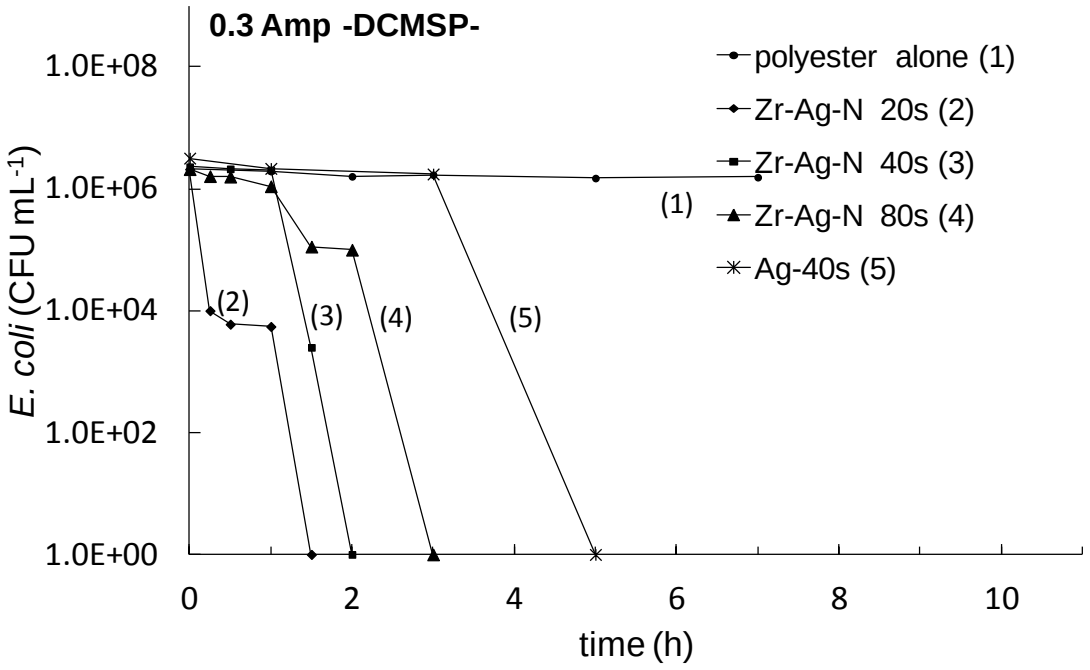

Figure (3d): *E*. coli inactivation on polyester sputtered by DCMSP at different times using an Ag- and Zr-target in (Ar + 10% N_2 0.5 Pa)

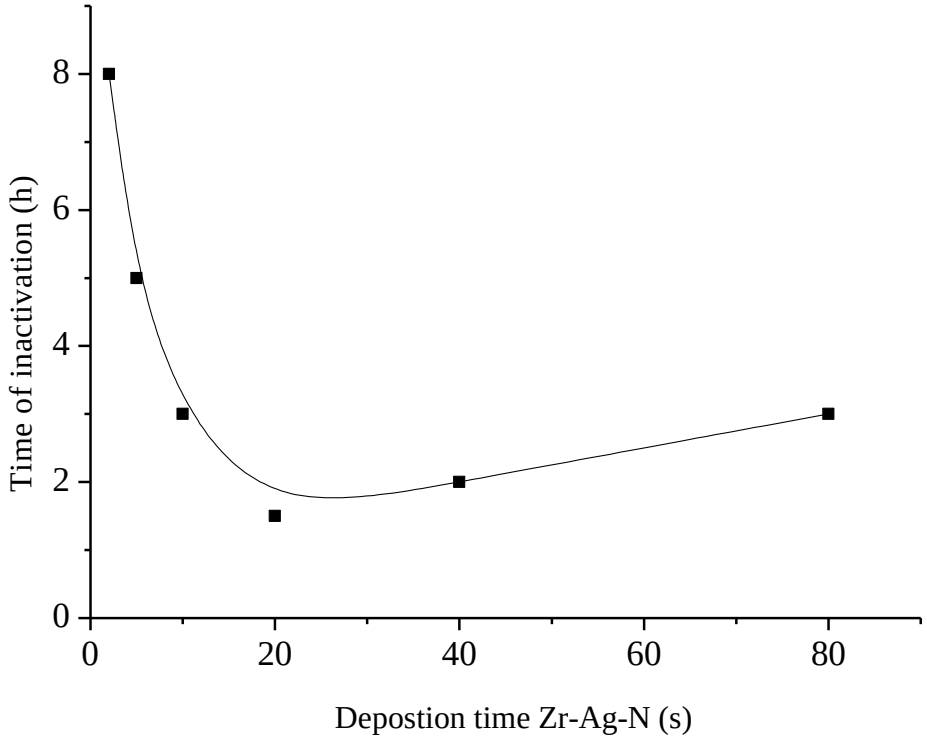

Figure (3d): Inactivation time of *E*. coli on Zr-Ag-N polyester as a function of the deposition time by DCMSP sputtered at 0.3 A in the dark.

3.1 Survival kinetics as a function of the initial concentration

Figure (3e) shows the bacterial inactivation kinetics of *E. coli* on the co-sputtered Zr-Ag-N (20 s) sample with an initial CFU concentration of: $6.8x10^6$, $5.5x10^7$ and$1.2x10^8$ $CFU.ml^{-1}$. It is readily seen that the inactivation of higher bacterial concentrations need longer time. This observation makes it possible to exclude a strong absorption of *E. coli* K12 on the co- sputtered Zr-Ag-N (20 s) sample. Adsorption of *E. coli* on the 30 nm particles is not possible since the size of the ellipsoidal shape *E. coli* K12 is ~1 micron [29]

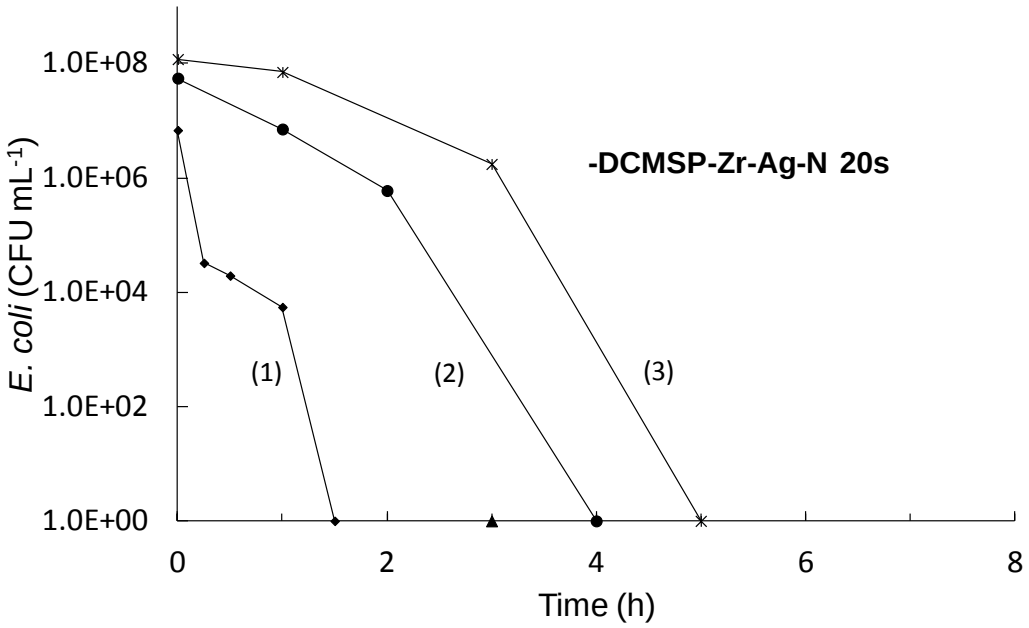

Figure (3e): Effect of the initial concentration on the loss of viability of *E. coli* on a co-sputtered Zr-Ag-N (20 s)

4. Transmission electron microscopy of Zr-Ag-N polyester samples

Figure (4a) presents the electron microscopy (TEM) of polyester. A 0.8 cm bar denotes the 20 nm scale in the insert. No nanoparticles were observed on the polyester fiber.

Figure (4b) shows the TEM of an Zr-Ag-N polyester sample sputtered for 5 s at 0.3 Amp. In figure (4b), the Ag-particles were 10–20 nm in diameters. Silver metallic particles have been reported to form above one nm [174]. The arrow in the upper right hand side in figure (4b) shows the Ag^o/Ag-ions flux direction reaching the polyester fiber. Coverage of 60–70% of the polyester fiber was observed in the direction of the flux of the Ag^o/Ag-ions arriving from the Ag-target.

Figure (4c) shows the EM of an Zr-Ag-N polyester sample sputtered for 20 s at 0.3 Amp. The Ag-particles presented diameter sizes of 15–40 nm and were appreciably bigger compared to the Ag-nanoparticles sputtered for 5 s a shown in figure (4b). This shows that Ag-aggregates are formed in a process due to Ag growing on other Ag-particles rather than interacting with ZrN. This suggests immiscibility of the Ag-particles with small ZrN crystallites on the polyester surface. A continuous deposit 30–45 nm thick of metallic Ag-particles were observed and a silver coverage of ~60–70% of the polyester fiber in the direction of the Ag^{o}/Ag-ion-flux from the Ag-target.

Figure (4d) presents the electron diffuse spectroscopy (EDS) for the Zr-Ag-N polyester sample sputtered for 20 s at 0.3 Amp. The Cu-signals originate from the Cu-grid used as a support the EM sample. The Ag-peaks are seen to be more significant than the Zr-peaks, since its abundance of this element is much higher than Zr as shown in Table 1.

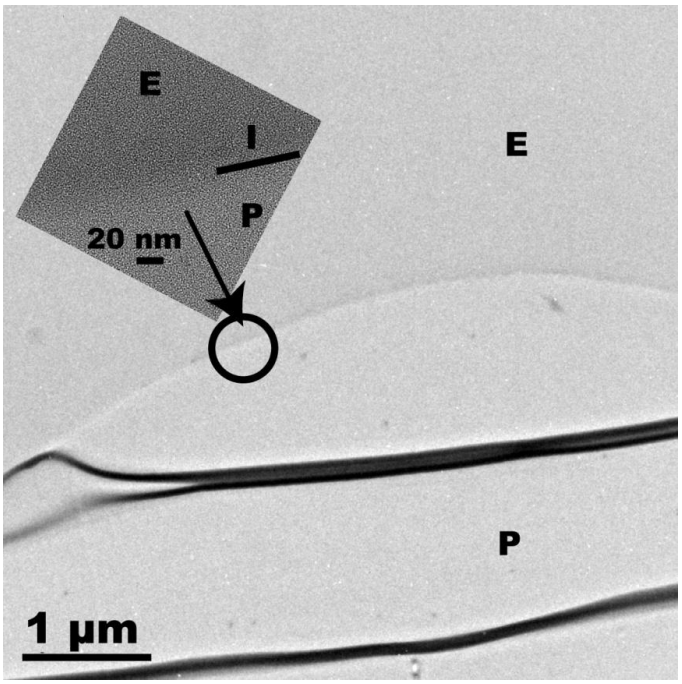

Figure (4a): TEM of polyester fiber. E stands for the epoxide used to enrobe the fiber during the sample preparation and P stands for polyester. For other details see text.

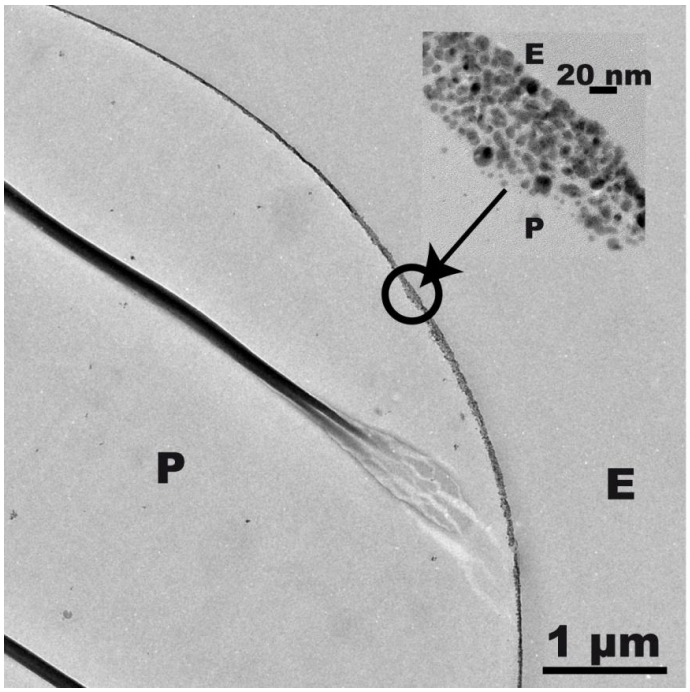

Figure (4b): TEM of a polyester P fiber cut at an angle of 35° embedded in an epoxy resin, sputtered confocally for 5 s with Ag and Zr in an Ar + 10% N_2 0.5 Pa atmosphere.

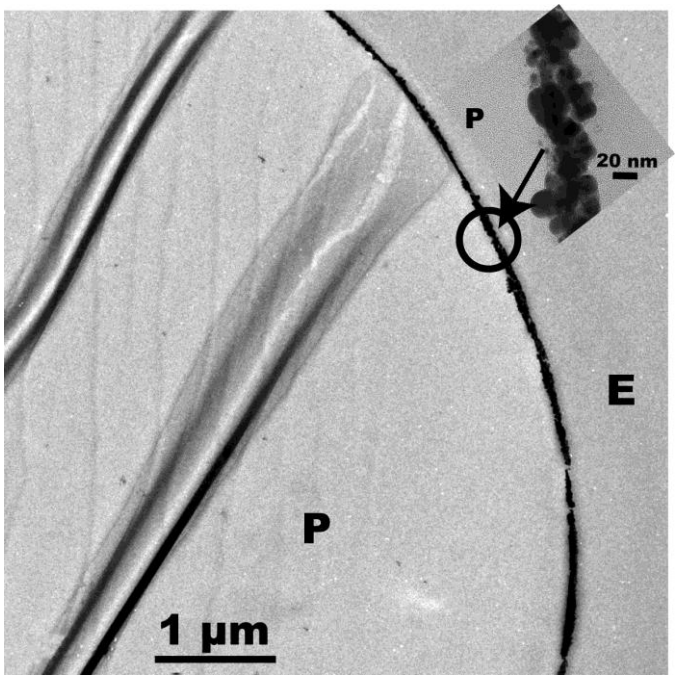

Figure (4c): TEM of a polyester (P) fiber cut at an angle of 35° embedded in an epoxy resin, sputtered confocally for 20 s with Ag and Zr in an Ar + 10% N_2 0.5 Pa atmosphere

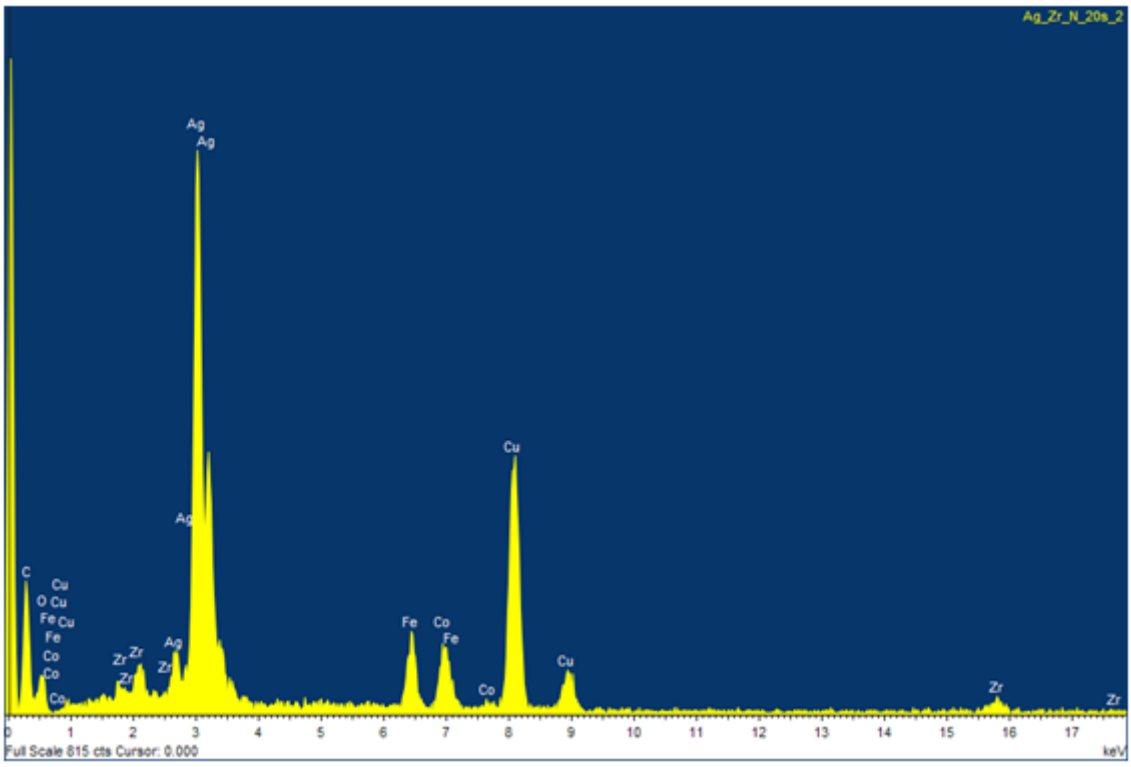

Figure (4d): Energy dispersive spectra (EDS) spectra of Zr-Ag-N polyester for a sample sputtered 20 s at 0.3 A.

5. Atomic force microscopy of Zr-Ag-N polyester sputtered at different times (AFM)

Figure (5) shows 600 nm×600 nm AFM images recorded on Zr-Ag-N films sputtered on Si-substrates for 2 s and 20 s with 0.3 Amp. The surface of the 2 s sputtered Zr-Ag-N film in figure (5a) is characterized by the presence of dispersed crystallites of <20 nm in diameter and some large clusters >20 nm. The surface morphology of the 20 s sputtered Zr-Ag-N film shown in figure (5b) is qualitatively different from the film sputtered for 2 s. Irregular crystallites of different sizes (20–60 nm) are observed. These crystallites are well separated each other and the surface coverage is not homogenous as it is noticed from the large contrast in the z-scale. The crystallites are assigned to Ag, as the amount of ZrN is low and their size <1 nm as described in figure (4). The ZrN films on polyester are amorphous.

With increasing the deposition time, the film thickness was seen to increase (Table 1). The increase in thickness brings an increase in the surface roughness. The root mean square (rms) values changes with increasing sputtering times 1.8 μm at 5 s to 2.8 μm at 20 s and 3.2 μm at 80 s.

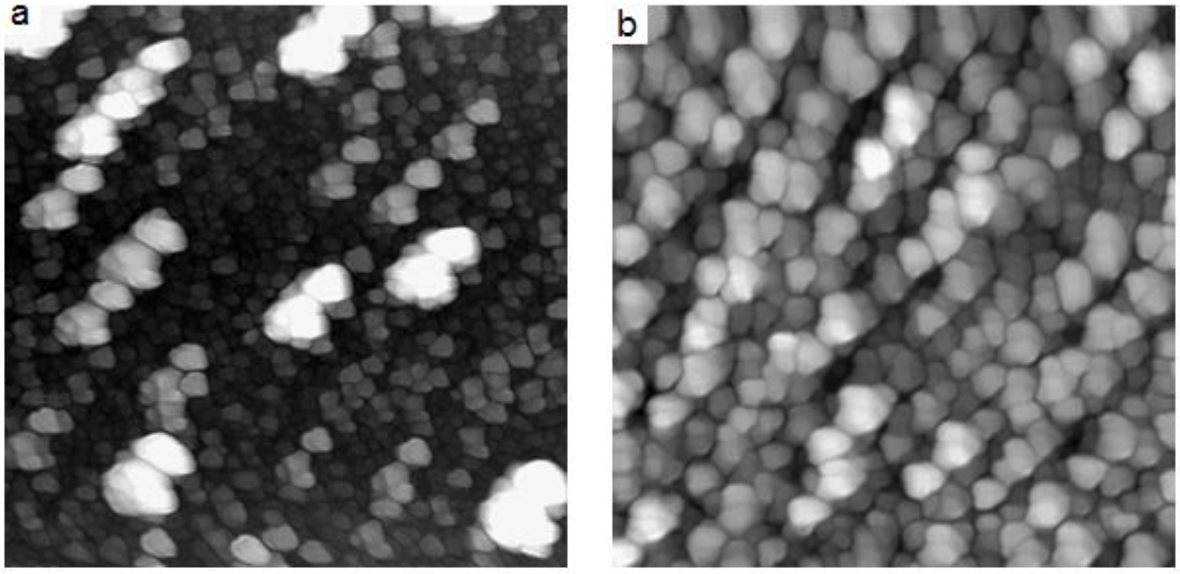

Figure (5): (a) AFM image 600 nm×600 nm of Zr-Ag-N on Si-wafers sputtered at 0.3 Amp for 2 s. (b) AFM image 600 nm×600 nm of Zr-Ag-N on Si-wafers sputtered at 0.3 A for 20 s.

6. Contact angle measurements (CA)

Figure (6) presents the contact angle for different Zr-Ag-N samples. Samples sputtered for 5 s at 0.3 Amp presented a contact angle of 64.4° at time zero. This contact angle decreased with the contact time on the Zr-Ag-N polyester surface due to high porosity (void areas, 20 μm pore sizes) of the polyester allowing for water penetration through the polyester microstructure. The Zr-Ag-N sputtered polyester become more hydrophobic after 20 s sputtering time as seen in the second rows showing an initial contact angle of 77.3°. Finally a contact angle of 101° was observed at time zero for 80 s sputtered samples. These samples were more hydrophobic due to the higher amount of Ag on the polyester.

The increase in surface layer thickness and droplet contact angle or hydrophobicity is concomitant with an increase of surface layer roughness of the sputtered Ag-layers. We have recently identified the active Ag-ions active on Ag-layers responsible for *E. coli* inactivation [8,18,208]. A 20 s DCMSP sputtered sample presented a higher number of Ag-layers with a concomitant higher rugosity compared to samples sputtered for 5 s. This leads to a faster *E. coli* inactivation time as shown in figure (3b and c).

Zr-Ag-N, sputtered for 5 s

0 min: 64.4^{o} 10 min: 43.8^{o} 15 min: 36.7^{o}

Zr-Ag-N, sputtered for 20 s

0 min: 77.3^{o} 10min: 46.2^{o} 15min: 25.9^{o}

Zr-Ag-N, sputtered for 80 s

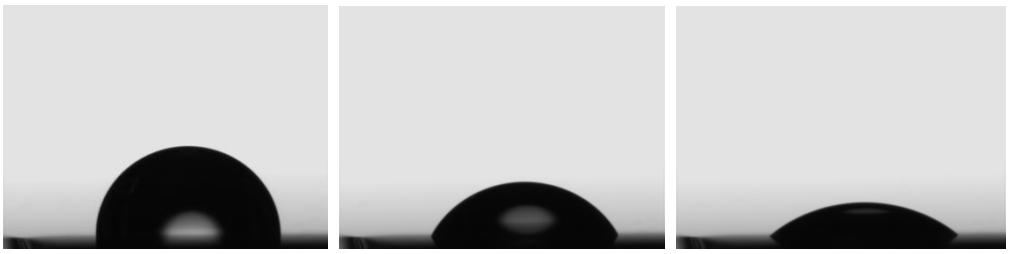

0min: 101.0^{o} 10min: 63.6^{o} 15min: 42.1^{o}

Figure (6): Contact angle (CA) for Zr-Ag-N polyester sputtered at 0.3 A for 5, 20 and 80 s. For other details see text.

7. X-ray photoelectronic spectroscopy of Zr-Ag-N polyester surfaces (XPS)

The surface atomic concentrations of the Zr-Ag-N polyester films from the XPS spectra are presented in the Table 2. The percentage atomic concentrations at time zero for polyester alone were: C 1s 76.4% and for O 1s 23.6%. Due to the DCSMP sputtered Ag and Zr after 2 s the percentage atomic concentration changed to C 1s 60.6%, O 1s 23.6%, Ag 3d 13.6% and Zr 3d 2.1%. At 20 s sputtering, the percentage atomic concentration showed a significant increase in the Ag topmost 10 layers, with values: C 1s 23.4%, O 1s 10.6%, Ag 3d 63.6% and Zr 3d 2.5%. From Table 2, it can be seen that Zr represents only about 2.1-3% of the total composition of the topmost layers.

The information for the X-ray photoelectron spectroscopy for Zr-Ag-N (20 s) polyester films within the E. coli inactivation time is shown next in Tables 3.

Table 2: Atomic percentage composition of Ag- and Zr-polyester sputtered by DCMSP as function of sputtering time

Sample Identifier	Name	Position (eV)	% at Conc
zero s	C 1s	282.9	76.4
	O 1s	530.2	23.6
	Ag 3d	-	-
	Zr 3d	-	-
2 s DCMSP	C 1s	284.9	60.6
	O 1s	531.4	23.6
	Ag 3d	368.4	13.6
	Zr 3d	182	2.10
20 s DCMSP	C 1s	285.0	23.4
	O 1s	530.7	10.6
	Ag 3d	368.5	63.1
	Zr 3d	182	3.00

Table 3: Evolution of the surface percentage atomic concentration of Zr-Ag-N polyester during the E. coli inactivation for DCMSP 20s sputtered sample

Sample Identifier	Name	Position (eV)	% at Conc
3 s	C 1s	282.9	37.1
	O 1s	530.2	09.6
	Ag 3d	368.5	50.5
	Zr 3d	181.9	2.8
60 min	C 1s	284.9	40.1
	O 1s	531.4	13.6
	Ag 3d	368.4	44.2

	Zr 3d	182	2.10
90 min	C 1s	285.0	48.3
	O 1s	530.7	15.1
	Ag 3d	368.5	35.0
	Zr 3d	181.8	1.6

7.1. XPS spectra investigation for samples of ZrN (15 min, 290 mA).

Figure (7) presents the Zr $3d_{5/2}$ doublet found for samples of ZrN (15 min, 290 mA) without bacteria contact. The deconvolution of the XPS signal has been carried out by means of the Casa-XPS program. The ZrN species shows a peak at 181.3 eV, the ZrO_2 doublet is seen at 182.4 eV, found from other groups [210-212]. Figure (7) presents the evidence for ZrO_2 formation on the polyester when sputtering ZrN under the experimental conditions described previously in the section experimental and discussed in section 3.3.

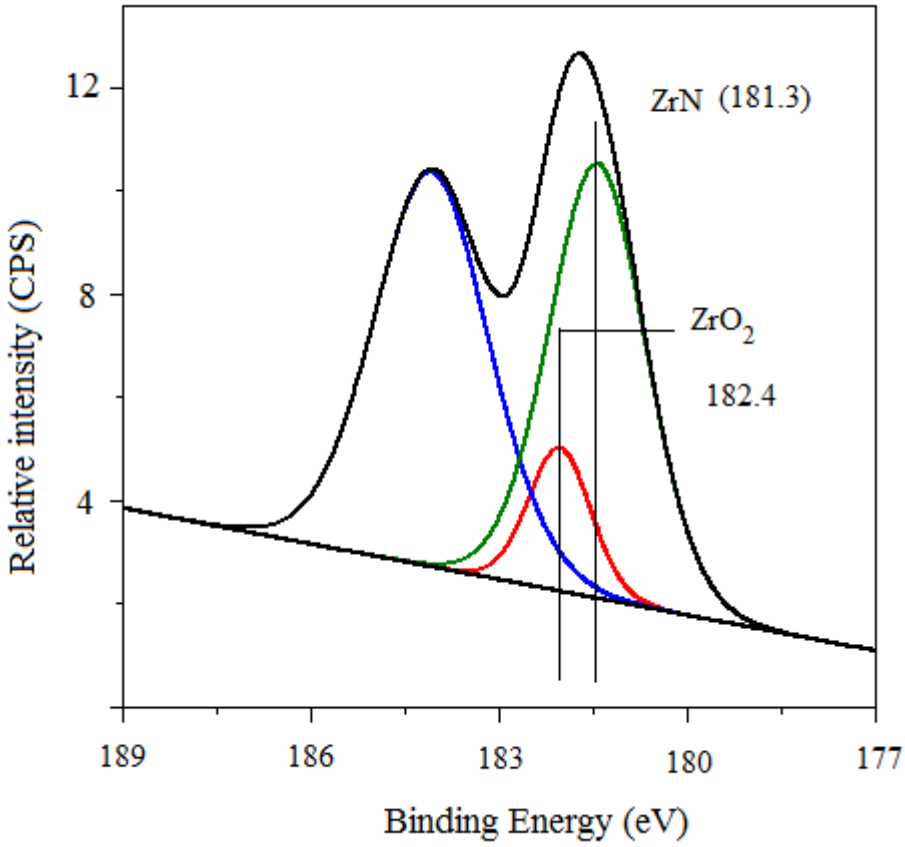

Figure (7): XPS spectra of ZrN DCMSP sputtered polyester (15min, 290 mA) showing the deconvoluted peaks for the Zr species.

7.2. XPS spectra investigation for samples of Zr-Ag-N (sputtering time 20 s, 300 mA and 290 mA).

A survey scan XPS spectrum of Zr-Ag-N (20 s) nanoparticles on the polyester in the range of binding energies 0–1000 eV is shown in figure (8). Original single peaks of Ag 3d and Zr 3d high-resolution XPS spectra are doubled, and these peak positions change a little with elapsed time. The shift of the ordinary peaks is calibrated with respect to the C 1s peak position set at 284.6 eV.

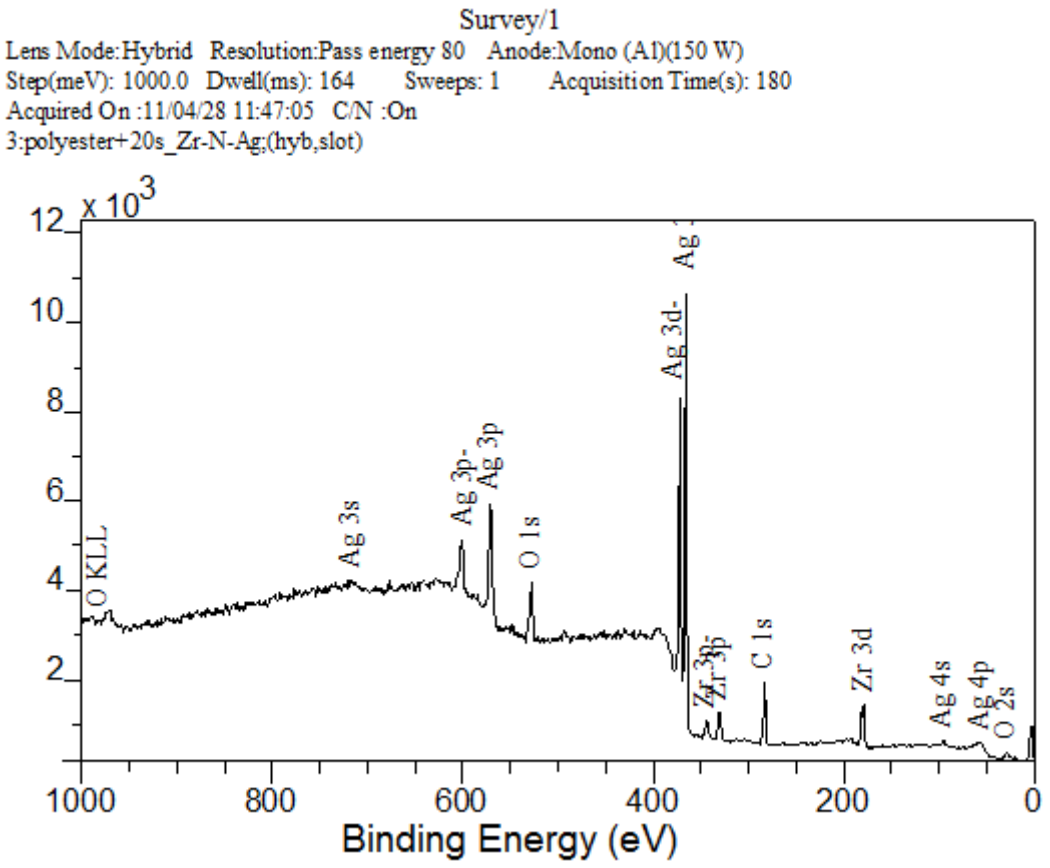

Figure (8): (a) Survey scan XPS spectra in the binding energy range 0–1000 eV (O 2s; Ag 4p; Ag 4s; Zr 3d; C 1s; Zr 3p; Ag 3d; Ag 3p; O 1s; Ag, O KLL), where KLL represent the Auger transition

The Ag $3d_{5/2}$ peak was found at 368.1 eV [180] as shown in figure (9). The charge effects compensation was carried out according to Shirley [181]. The Zr $3d_{5/2}$ peaks were detected at BE of 181.1 eV for the 2 s and also the 20 s Zr-Ag-N samples corresponding to Zr-N species [213] and as shown below in figure (10). ZrO_2 appears when the Zr in the Zr-

Ag-N is exposed to air (O_2) and contacted for 3s with bacteria. Zirconia IR peaks at ~500 cm^{-1} were found for Zr-cluster sizes ≤6 ˚A have recently been reported [213]. A very small signal for N was detected in the topmost 10 layers (2 nm) by XPS on the polyester surfaces indicating that the amounts found were below the detection limit for N in the XPS spectrogram. In figures (4b) and (4c) the Zr was not detected since the limit of resolution by the TEM employed was ~1 nm.

Figure (9a) shows in the left upper inset the $Ag3d_{5/2}$ peak stepwise shift from 368.2 eV to 368.9 eV assigned to the shift from Ag^o to $Ag^{1+/2+}$ ionic species within 90 min during *E. coli* inactivation on a Zr-Ag-N (20s) polyester sample [8,181]. The XPS shift lies in the region related to the oxidation states between Ag^o and Ag^{2+}. Since these shits were observed by XPS on the upper polyester modified layers this is indicative for the presence of Ag ions layers located mainly at the Ag-interface.

Figure (10a) presents in the left inset the shift of the Zr $3d_{5/2}$ peak during E.coli inactivation of the Zr-Ag-N (20 s) sample within 90 min from 182.9 eV to 181.8 eV. This significant negative shift -1.1 eV is further evidence for redox processes taking place on the polyester surface involving Zr^{4+}/Zr^{2+} during bacterial inactivation. Shifts in the peaks of 0.2 eV reflect valid changes in the oxidation stated of the elements [181,189].

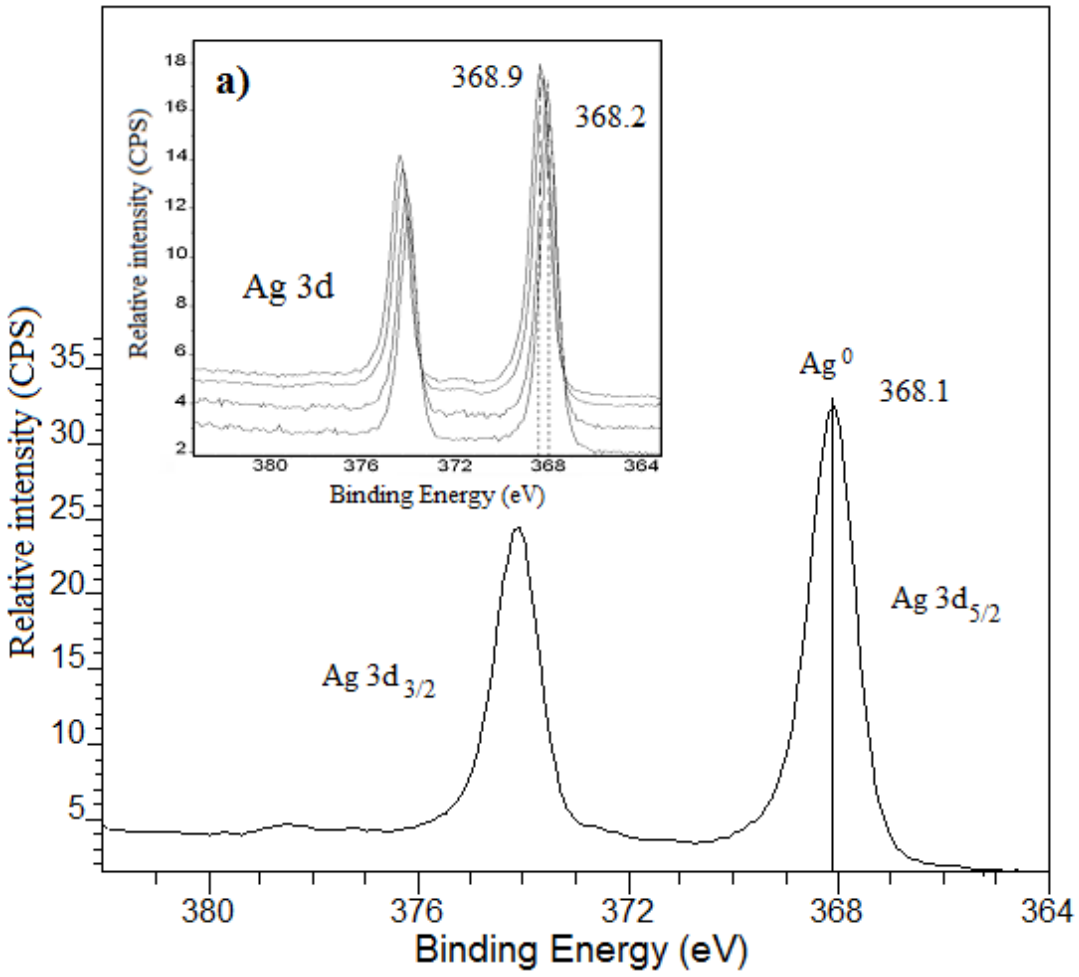

Figure (9): high resolution XPS spectra of the Ag 3d doublet from the Zr-Ag-N (20s) polyester sample, **(a):** Upper left inset: Ag $3d_{5/2}$ shift between times zero and 90 min during *E. coli* inactivation on Zr-Ag-N (20s)

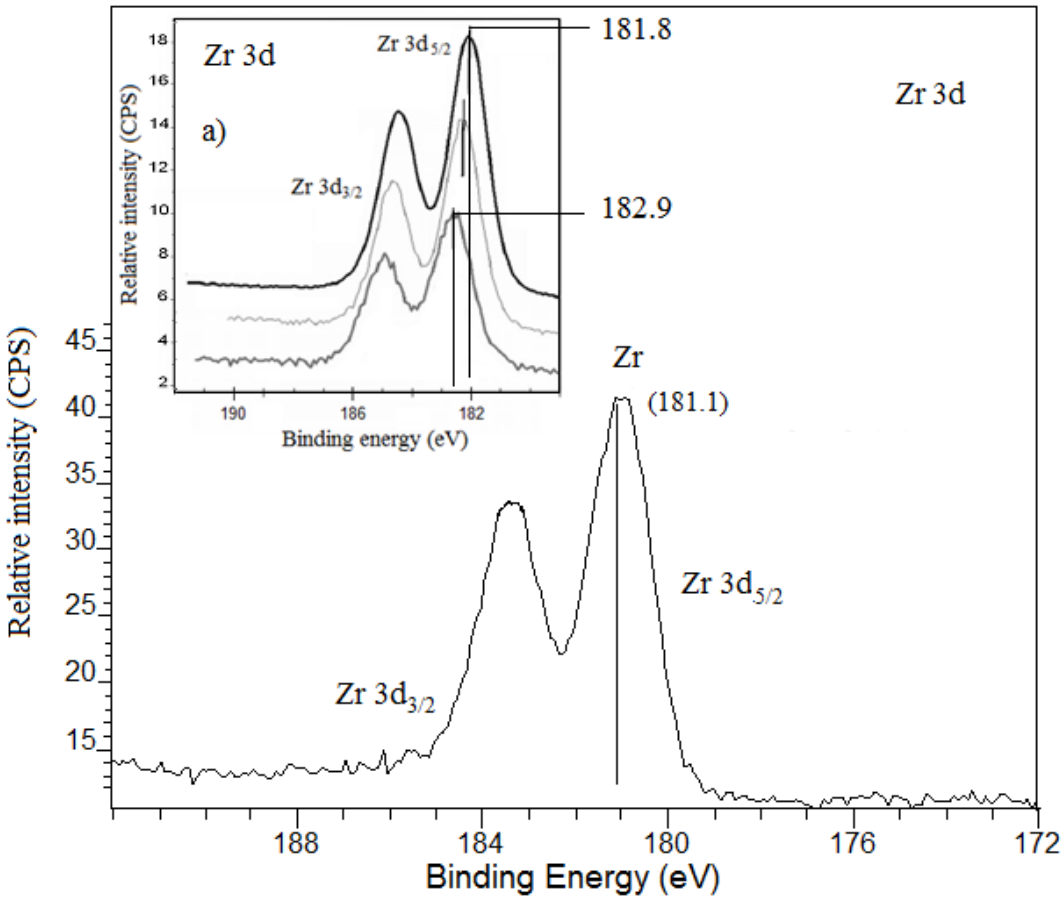

Figure (10): High resolution XPS spectra of the Zr 3d doublet from the Zr-Ag-N (20s) polyester sample, **(a):** Upper left inset: Zr $3d_{5/2}$ shift during *E. coli* inactivation on Zr-Ag-N (20s) between zero (3s contact with bacteria) and 90 min.

8. Repetitive E. coli inactivation by recycling of a Zr-Ag-N sample and ions release during bacterial inactivation detected by ICPS.

Figure (11) shows the recycle of the co-sputtered Zr-Ag-N (20s) sample during *E. coli* bacterial inactivation. Figure (11) shows that after 6 cycles, the samples kept their initial performance. After the first and second recycling the discontinuity in the abscissa shows a non-sequential kinetics for the 4th and 6th recycling conserving the initial loss of viability. The inactivation bacterial time remained within 60-90 min.

The surface atomic percentage concentration of elements in the Zr-Ag-N (20s) sputtered samples after being contacted 3s with bacteria as shown in Table 3 were: O1s 09.6%; C1s 37.1%; Zr3d 2.8% and Ag3d 50.5%. These percentages did vary less than 16% during the 90 min reaction leading to the total bacterial loss of viability. Therefore, the rapid

destruction of the fragments of bacterial decomposition accounts for the constant rate observed for the total loss of viability reported in figure (11).

Figure (12) shows the Ag- and Zr-ions concentrations released during the recycle of Zr-Ag-N (20s) sputtered samples. The Ag-ions release during 6 cycles was < 5 ppb/cm^2, which is below the allowed cytotoxicity levels of 40 - 95 ppb/cm2 [214]. Therefore, the bacterial inactivation mediated by Zr-Ag-N (20s) does not introduce cytotoxicity but proceeds through an oligodynamic effect.

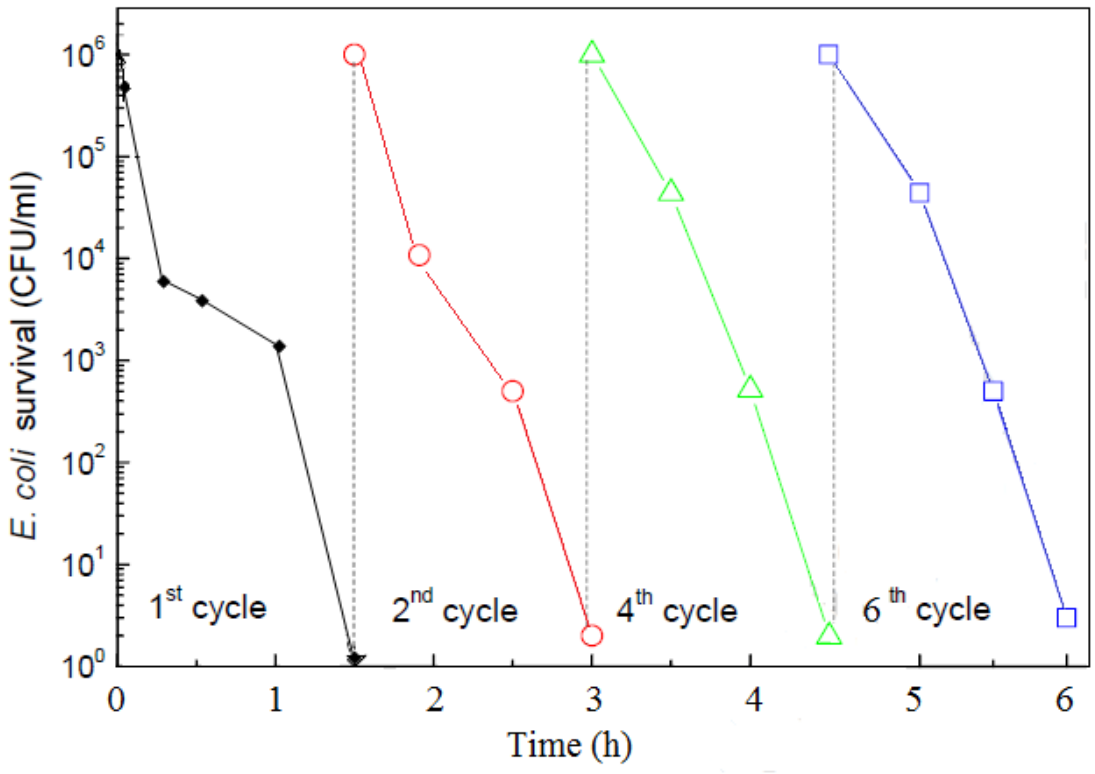

Figure (11): Cycling of a Zr-Ag-N (20 s) samples leading to the total loss of bacterial viability

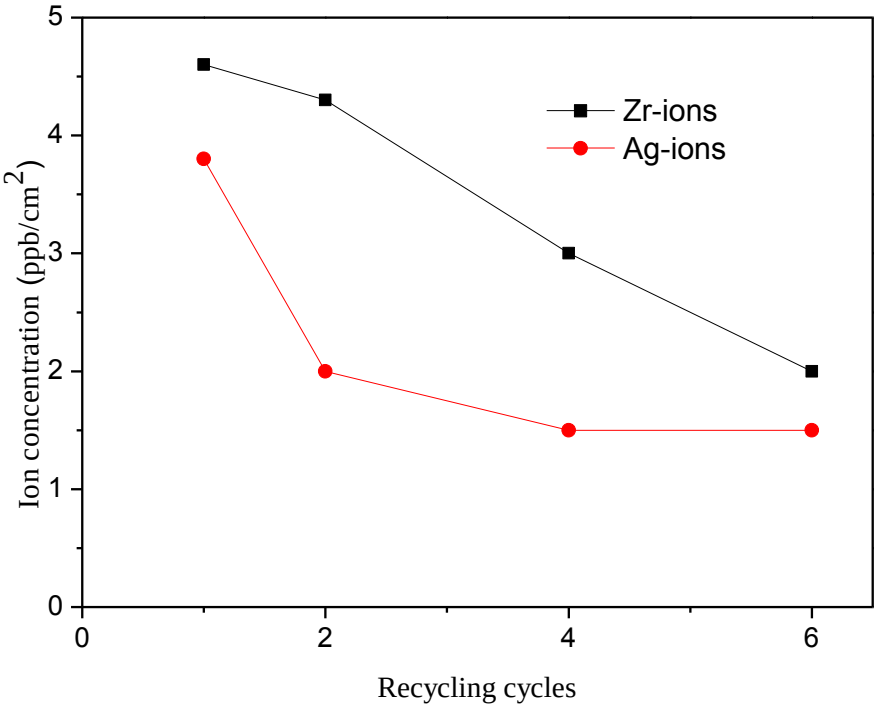

Figure (12): Ion-coupled plasma mass spectrometry (ICP-MS) determination of Ag-ions and Zr-ions released from a co-sputtered Zr-Ag-N (20 s) within the *E. coli* loss of bacterial viability.

9. Bacterial inactivation by light activated ZrN and Zr-Ag-N-polyester surfaces

Figure (13) shows the inactivation of E. coli under low intensity visible/actinic light (400–700 nm, 4 mW/cm^2) by ZrN-sputtered (15 min) and Zr-Ag-N polyester samples. Figure (13) shows the beneficial effect of the visible light revealing the semiconductor behavior of the coating sputtered on polyester as detected by XPS. Section 10 suggest a mechanism for the photo-activated Zr-Ag-N cause interfacial charge transfer leading to the formation of reactive oxidative species leading to the bacterial loss of viability. The ZrN-polyester samples (15 min) under visible light irradiation inactivate completely *E. coli* within 240 min (trace 5). The Zr-Ag-N for 20s sample under light shows the fast bacterial inactivation compared in the dark leads to a 6 $\log_{10}$ bacterial reduction was observed within 45 min and this result is shown in the figure (13) trace 4.

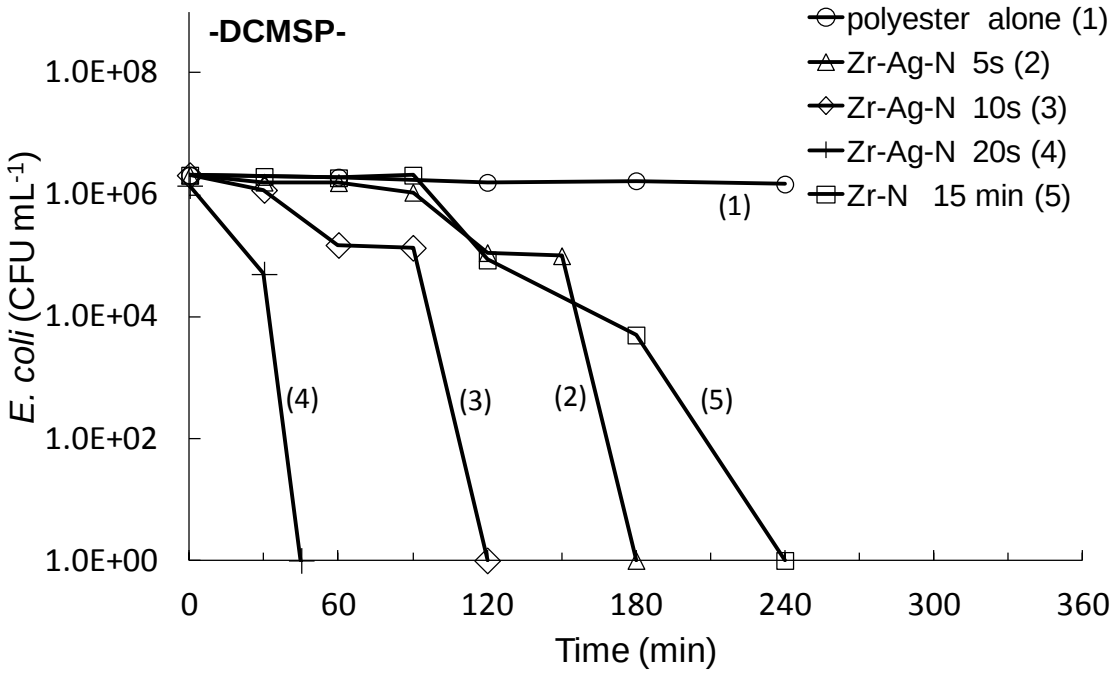

Figure (13): *E. coli* loss of viability by ZrN and Zr-Ag-N as a function of time. The samples were irradiated with an Osram Lumilux18/827 actinic lamp at a dose 4.1 mW/cm^2

10. Suggested reaction mechanism.

The ZrO_2 species has been deconvoluted as described in the XPS section for the Zr-N (15min) and for Zr-Ag-N (20s) sample after 3s contacted with bacteria. All metals with exception of Hg are known to form surface hydroxide in contact with air containing water vapor. Zr-Ag-N samples form AgOH on its surface. The favorable decomposition of AgOH leads to Ag_2O as in (eq1) [215].

$$2\ AgOH \longrightarrow Ag_2O + H_2O \ (pk= 2.87) \quad (1)$$

Ag_2O is thermodynamically stable at pH 6-7 where the bacterial inactivation of *E. coli* is shown to proceed in Figures 1a-1c. For mechanistic considerations of the ZrO_2/Ag_2O under visible light we consider next the energy level of Ag_2O and ZrO_2. The ZrO_2 nanoparticles in Figure (4c) present sizes of ~10 nm and these nanoparticles have been reported with a band-gap (bg) ~3.2 eV [216], a conduction band (cb) at -1.0 eV NHE and a valence band (vb) at +2.2 eV NHE [217]. Visible light photo-activates the semiconductor Ag_2O with $1.46 < bg < 2.25$ eV [218- 219]

$$Ag_2O + light \longrightarrow Ag_2O(h_{vb}^{+}) + Ag_2O(e_{cb}^{-}) \quad (2)$$

The bacterial inactivation kinetics reported in figure (13) suggests that the interfacial charge transfer process (IFCT) [220] in the co-sputtered Zr-Ag-N film proceeds more readily compared to the sputtered Zr-N sample (Figure 13 trace 5) due to the shorter distance between Zr and Ag inducing higher quantum efficiency. Donor-acceptor pair interactions depend on the charge diffusion distance and this is a function of the particle size and shape in the film microstructure.

Under visible light, the transfer of charge from Ag_2O to ZrO_2 is thermodynamically favorable. The Ag_2O_{cb} is -1.3 eV NHE at pH 0. The valence band vb of Ag_2O +0.2 eV NHE at pH 0 [218-220] lie above the ZrO_2 presenting a conduction band (cb) at -1.0 eV and the valence band (vb) at +2.2 eV. The electrons in the Ag_2O_{cb} inject electron into the ZrO_{2cb} since they are situated at a higher energetic level. The electrons in eq(2) react with ZrO_2

$$ZrO_{2(e-)} + O_2 \longrightarrow ZrO_2 + O_2^{-} \quad (3)$$

We suggest that O_2 eq(3) promote the reactions (5,6) producing highly oxidative radicals, while the h^+ in eq (2) would react with H_2O (water vapor) as shown below in eq(4). This reaction runs parallel with eq(5) generating OH^o radicals or other highly reactive oxidative radicals able to inactivate *E. coli*. The h_{vb}^{+} in eq (4) originate from the Ag_2O nanopaticles in eq(2)

$$h_{vb}^{+} + H_2O \longrightarrow OH^o + H^+ \quad (4)$$

$$e_{cb}^{-} + H_2O + O_2 \longrightarrow OH^o + OH^- + 1/2O_2^{-} \quad (5)$$

$$e_{cb}^{-} + O_2 \longrightarrow O_2^{\cdot -} \quad (6)$$

11. Conclusions

• Zr-nitride films and Zr-Ag-N on polyester have been deposited by sputtering methods. This study presents the effect of visible light induced processes on *E. coli* inactivation

• A sputtered Zr-promoted polyester coated with Zr-Ag-N led in the dark to a faster *E. coli* bacterial inactivation compared with an Zr–N and Ag surface.

• Higher energies (currents) of 0.3 A used during the confocal Zr-Ag-N sputtering on polyester led to a higher Ag-deposition compared with 0.05 A currents having beneficial effect on the antibacterial E. coli inactivation time.

• Zr-Ag-N film sputtered at 0.3 Amp for 20 s was able to inactivate *E. coli* within 3/2 h.

• This study presents the first experimental evidence relating the thickness of the Zr-Ag-N layer to the Ag-grain sizes, the hydrophobic and roughness properties of the Zr-Ag-N film. These properties are shown to be controlling parameters affecting the observed E. coli inactivation kinetics.

Conclusion

The development of surfaces and coatings that can kill bacteria is important to maintain a clean environment. This study has shown the beneficial antibacterial activity of TiO_2 and silver grafted on textile fabrics (polyester) under light and in the dark. A minimum loading of TiO_2 and silver is necessary to inhibit the airborne bacterial growth. This effect was investigated and reported taken *E. coli* K-12 as a bacterial model.

We report polyester treated by RF-plasma followed by chemical deposition of TiO_2 on polyester surface. The results show that plasma-treated polyester fabrics had much better antibacterial performance compared with untreated samples. The RF-plasma increased the number of active sites and bondability on the polyester a higher TiO_2 loading compared to non-pretreated samples. Accordingly, the pretreated samples accelerated *E. coli* inactivation reducing by a factor of >3 the bacterial inactivation time compared to non-pretreated polyester TiO_2 samples.

The polyester RF-plasma pretreatment modified of the surface ratio of oxidative and reductive species in the polyester surface The ratio of oxidized to reduced functionalities (COOH + COH / CH_2) were seen to remain constant with RF-treatment time beyond 30 min. Oxidative species (mainly OH-radicals) were identified on the irradiated polyester-TiO_2 as a function of time on RF modified samples. The effects parameters such as light dose, initial *E. coli* concentration, type of lamp and repetitive bacterial inactivation have been investigated with the best sample. It was seen that the *E. coli* inactivation kinetics are strongly dependent on these parameters. Applying an Osram Lumilux L18 W/840 lamp, the time of inactivation become longer by a factor of 2, compared with light from an Osram Lumilux 18 W/827 lamp.

TEM of the RF-plasma pretreated polyester followed by coating of TiO_2 shows a continuous TiO_2 film. Evidence is presented by XPS for Ti^{4+}/Ti^{3+} redox processes during bacterial inactivation. By XPS, self-cleaning of the bacterial inactivation residues on the polyester-TiO_2 were evaluated.

In the second part, the deposition of silver films by DCMS, DCMSP and HIPIMS on the polyester were compared and the Ag-coatings did not affect the flexibility/handling of the textile. We produced evidence for lower amounts of Ag-deposited by HIPIMS required to inactivate *E. coli* compared to DCMS and DCMSP. This study shows the potential of HIPIMS to produce Ag-polyester having a low content of Ag compared to DCMS and DCMSP effective in *E. coli* inactivation. Indeed, the most effective *E. coli* inactivation by DCMS and DCMSP sputtered for 160s had Ag-loadings ~3 times higher than the loading obtained by HIPIMS after 150s of 0.0630 %Ag wt/wt polyester. The Ag-nanoparticle films

sputtered by DCMSP at 0.3 Amp for 160 s was observed to inactivate completely *E. coli* within 2 h having a content of 0.205% Ag wt%/polyester wt%. HIPIMS-sputtered at 5 Amps for 75 s led to complete *E. coli* bacterial inactivation also within 2 h having a content Ag 0.031% Ag wt%/polyester wt%.

To determine the thickness of Ag deposited on polyester, a nominal calibration of the Ag-film thickness was carried out for DCMS, DCMS Pulsed and HIPIMS Ag-deposition at different Amp on Si wafers. That lead, the atomic rate of deposition with DCMS and DCMSP is 6.2×10^{15} atoms Ag/cm^2 s while with HPIMS this rate was 2.7×10^{15} atoms Ag/cm^{2}s. The results show that the nominal thickness of the Ag-HIPIMS layer of 80 nm was about 21/2 times lower than the ones attained with DCMS and DCSMP inducing a faster *E. coli* inactivation kinetics.

An electron microscopy (TEM) of the Ag-polyester full fiber sputtered by DCMS, DCMSP and HIPIMS shows that the HIPIMS sputtered Ag-nanoparticles provide a high polyester fiber surface coverage, reaches up to 85-90% of the total fiber, compared to the DCMS and DCMSP sputtered Ag on polyester (the coverage were 40–50% and 65–70% successively). This allows for a greater interaction surface which accelerates the bacterial inactivation compared to DCMS and DCMPS-sputtered polyester.

X-ray diffraction shows Ag-metallic character for DCMS and DCMSP sputtered samples for longer times compared to the sputtered Ag-clusters sputtered for short times. Three types of Ag (Ag^0, Ag^+, Ag^{2+}) were deposited by the DCMSP and HIPIMS as determined by X-ray photoelectron spectroscopy (XPS). On the other side, one type of silver (Ag^0) was deposited by DCMS. This allows the bacterial inactivation to proceed in similar times in HIPIMS compared to DCMS and DCMPS-samples in spite of having a much lower loading of Ag/cm^2 since the disinfection is shown to proceed due to Ag-ions and not due to Ag^o. (XPS) was also used to determine the surface atomic concentration of O, Ag, and C on the Ag–polyester. These surface atomic concentrations were followed during the *E. coli* inactivation time providing the evidence for the *E. coli* oxidation on the Ag–polyester.

In the last part of this work, evidence is presented for ZrN and Zr-Ag-N films as bactericide films in the dark and when exposed to low intensity visible/actinic light. Zr-Ag-N films were deposited on polyester by DCMSP in Ar + N_2 atmosphere. These composite films were more active in *E. coli i*nactivation compared to the Ag-films by themselves. The most suitable bacterial inactivation under light was attained with the Zr-Ag-N co-sputtered samples on polyester for 45 min. In the dark, the *E. coli* inactivation kinetics on Zr-Ag-N polyester surfaces was accelerated >4 times compared to samples sputtering only Ag. Sputtering Zr in

N_2 atmosphere presented no antibacterial activity by itself when applied for short times (< one min). Bacterial inactivation kinetics of *E. coli* depends on the amount of Ag on the polyester and the type of sputtering either sequential or simultaneous of ZrN and Ag. The Zr-Ag-N polyester sample sputtered for 20 s at 0.3 a led to the fastest antibacterial *E. coli* inactivation kinetics within 90 min. The Zr-Ag-N XPS envelope was deconvoluted showing ZrO_2 and ZrN. A possible reaction mechanism is suggested based on the energetic band levels of Ag_2O and ZrO_2.

References

[1] A. Kramer, I. Schwebke, G. Kampf, BMC Infect. Dis. 6 (2006) 130–138.

[2] S. Dancer, J. Hosp. Infect. 73 (2009) 378–385.

[3] K. Page, M. Wilson, I.P. Parkin, J. Mater. Chem. 19 (2009) 3819–3831 and references therein

[4] K. Page, R. Palgrave, I.P. Parkin, M. Wilson, S. Shelley, A. Chadwick, J. Mater. Chem., 17 (2007) 95−104

[5] H. Pant, D. Pandeya, K. Nam, W. Baek, S. Hong, H. Kim, Journal of Hazardous Materials 189 (2011) 465–471

[6] T. Yuranova, R. Mosteo, J. Bandara, D. Laub, J. Kiwi, J. Mol. Catal. A 244 (2006) 160–167.

[7] M.I. Mejı´a, J.M. Marı´n, G. Restrepo, C. Pulgarı´n, E. Mielczarski, J. Mielczarski, Y. Arroyo, J.-C. Lavanchy, J. Kiwi, Preparation, Appl. Catal. B 91 (2009) 481–488.

[8] M.I. Mejı´a, J.M. Marı´n, G. Restrepo, C. Pulgarı´n, E. Mielczarski, J. Mielczarski, J. Kiwi, ACS Appl. Mater. Interf. 2 (2010) 230–235.

[9] D. Gumy, C. Pulgarin, C. Morais, P. Bowen, J. Kiwi, Applied Catalysis B 63 (63) (2005) 76–84.

[10] J. Kiwi, C. Pulgarin, Catalysis Today 151 (2010) 2–7 (and references therein).

[11] A.W. Daoud, S.K. Leung, W.S. Tung, J.H. Xin, K. Cheuk, K. Qi, Chem. Mater. (2008), 1242–121254.

[12] W. Daoud, H. Xin, Chem. Comm. (2005) 2110–2112.

[13] M. Radetic, V. Ilic, V. Vodnik, S. Dimitijevic, P. Jovancic, Z. Saponjic, J. Nedeljkovic, Polym. Adv. Technol. 19 (2008) 1816–1821.

[14] M. Amberg, K. Greder, M. Barbadoro, M. Heureberg, D. Hegemann, Plasma Proc. Polym. 5(2008) 874–880.

[15] C. Gunawan, W. Teoh, P. Marquis, J. Lifia, R. Amal, Small 5 (2009) 341.

[16] T. Yuranova, A.-G. Rincon, A. Bozzi, S. Parra, C. Pulgarin, P. Albers, J. Kiwi, J Photochem.Photobiol. A. Chem. 161 (2003) 27-34.

[17] T. Yuranova, A.-G. Rincon, C. Pulgarin, D. Laub, N. Xanthopoulos, H.-J. Mathieu, J. Kiwi, J. Photochem. Photobiol. A. 181 (2006) 363.

[18] O. Baghriche, A. Zertal, R. Sanjines, C. Ruales, C. Pulgarin, I. Stolitchnov, J. Kiwi, Surface & Coatings Technology 206 (2012) 2410–2416

[19] E. Rupp, T. Fitzgerald, N. Marion, V. Helget, S. Puumala, R. Anderson, D. Fey, Am. J. Infect. Control 32 (2004) 445–452.

[20] P. Ehiasarian, Y.A. Gonzalvo, T.D. Whitmore, Plasma Processes Polym. 4 (2007) 5309.

[21] A.P. Ehiasarian, A. Vetushka, A. Hecimovic, S. Konstantinidis, J. Appl. Phys. 104 (2008) 083305.

[22] A.P. Ehiasarian, R. New, W-D. Münz, L. Hultman, U. Helmersson, V. Kouznetsov, Vacuum 65 (2002) 147–154.

[23] K. Sarakinos, J. Alami, S. Konstantinidis, Surf. Coat. Technol.204 (2010) 1661–1684.

[24] V. Stranak, M. Cada, Z. Hubicka, M. Tichy, R. Hippler,J. Appl. Phys.108 (2010) 043305.

[25] J. Lin, J. Moore, W. Sproul, B. Mishra, Z. Wu, Wang, Surf. Coat. Technol. 204 (2010) 2230–2239.

[26] P.J. Kelly, H. Li, K.A. Whitehead, J. Verran, R.D. Arnell, I. Iordanova, Surface and Coatings Technology 204 (2009) 1137–1141.

[27] L. Zhang, R. Dillert and D. Bahnemann, En & Environ. Sci. 5 (2012) 7491-7507.

[28] A. Fujishima, T. Rao, D. Tryk. J. Photochem. Photobiol. C Revs. 1 (2009) 1-21.

[29] W. Tung, W. Daoud. J. Materr. Chem. 21 (2011) 7858-7869.

[30] P. V. Kamat, Accounts Chem. Res. 45 (2012) 1906-1915

[31] von Recum AF. :A review. J Biomed Mater Res, 18, 323-336 (1984).

[32] Taylor TL. Journal of American Podiatry Association, 65, 1-12 (1975).

[33] Seitz H, Marlovits S, Schwendenwein I, Müller E, Vécsei V. Biomaterials,19, 189-196 (1998).

[34] A. Bozzi, T. Yuranova, J. Kiwi, J. Photochem. Photobiol. A 108 (1997) 1–16.

[35] C.M. Chan, T.M. Ko, H. Hiraoka, Surface Science Reports 24 (1996) 1–54

[36] G. Kill, D.H. Hunter, N.S. McIntyre, J. Polym. Sci. Part A: Polym. Chem. 34 (1996) 2299.

[37] P.K. Chu, J.Y. Chen, L.P. Wang, N. Huang, Mater. Sci. Eng.: Rep. 36 (5&6) (2002) 143–206.

[38] D. Mihailovic, Z. Saponjik, M. Radoicic, T. Radetic, J. Jovancic, M. Nedeljovic, M. Radetic, Carbohydrate Polym. 79 (2010) 526-532.

[39] D. Hegemann, M. Hossain, M. Balazs, Prog. Org. Coatings. 58 (2007) 237-240.

[40] D. Hegemann, M, Amberg, A. Ritter, M. Heuberger, Mats.Technol. 24 (2009) 41-45.

[41] J. Kasanen, M. Suvanto, Z. Pakkanen, J. Appl. Polym. Sci. 111(2007) 2597-2602.

[42] A. Bozzi T. Yuranova, J. Kiwi, J. Photochem. Photobiol. A. 172 (2005) 27-34.

[43] M. I. Mejía, J. M. Marín, G. Restrepo, C. Pulgarín, E. Mielczarski, J.Mielczarski, J. Kiwi, ACS Appl. Mater. &Interf. 1 (2009) 2190-2198.

[44] A. Torres, C. Ruales, C, Pulgarin, C. Aimable, P. Bowen, V. Sarria, J. Kiwi, ACS Appl. Mater. & Interf. 2(2010) 2547-2552.

[45] A. Bogaerts, , E. Neyts, R. Gijbels, J. Mullen, Spectrochimica Acta Part B 57 (2002) 609–658.

[46] R. Sharmaa, E. Holcomb, S. Trigwell, M. Mazumder, Journal of Electrostatics 65 (2007) 269–273.

[47] A. Kinloch, Adhesion and Adhesives. Chapman and Hall Inc. New York, USA(1987).

[48] M. Willert-Porada, Advances in microwave and radio frequency processing, 8th International Conference on Microwave and High-Frequency Heating, Germany (2001) 440-443.

[49] X. Li, Y. Oiu, Appl. Surf. Sci., 258 (2012) 7787-7793.

[50] A, Johnson, The theory of Coloration of textiles: Society of Dyes and Colourists, Bradford, UK.,1983.

[51] M. Dhananjeyan, E. Mielczarski, K. Thampi, Ph. Buffat, M. Bensimon, A. Kulik, J. Mielczarski and J. Kiwi, J. Phys. Chem. B 105 (2001) 12046-12055.

[52] D. Wu, M. Long, J. Zhou, W. Cai, X. Zhu, C. Chen, Y. Wu, Surf. & Coat. Technol. 203 (2009) 3728–3733.

[53] M. Dhananjeyan, J. Kiwi, R. Thampi, Chem. Com. (2000) 1443-1444.

[54] Handbook of thin film deposition processes and techniques, edit by Krishna Seshan , second edition,. Noyes Publications, Norwich, New York, U.S.A. 2002, p.14.

[55] W. R. GROVE,Phil. Trans. Royal Soc. London, 142 (1852) 87.

[56] J. A. Thornton, J. E. Greene, Handbook of Deposition Technologies for Films and Coatings, 2e edition, R. F. BUNSHAH (éditeur), Noyes Publications, Park Ridge, New Jersey, U.S.A., 1994, p.249.

[57] D. Mattox, Handbook of physical Vapor Deposition (PVD) Processing, Noyes, Westwood, Neww Jersey, U.S.A., 1998.

[58] G. K. Wehner, Appl. Phys. 26 (1955)1056.

[59] L. Holland, Vacuum Deposition of Thin Films, Wiley, New York, U.S.A., 1961.

[60] L. Maissel, R. Glang, Handbook of Thin Films Technology, McGraw Hill, 1970.

[61] K. Wasa, Bull. Mater. Sci . 16 (1993) 6643.

[62] U. Klueh, V. Wagner, S. Kelly, S. Johnson, A. Bryers, J. Biomed. Mater. Res. 53 (2000) 621–631.

[63] H.A. Foster, W.D. Sheel, P. Sheel, P. Evans, S. Varghese, N. Rutschke, M.H. Yates, J. Photochem. Photobiol. A 216 (2010) 283–289.

[64] M.S.P. Dunlop, P.C. Sheeran, A.J. Byrne, S.A.M. McMahon, A.M. Boyle, G.K. McGuigan, J. Photochem. Photobiol. A 216 (2010) 303–310.

[65] S. Ohashi, S. Saku, K. Yamaamoto, J. Oral Rehabil. 31 (2004) 364–369.

[66] AgION Technologies Inc., www.agion-tech.com.

[67] C. Castro, R. Sanjines, C. Pulgarin, P. Osorio-Vargas, A. Giraldo, J. Kiwi, J. Photochem. Photobiol. A 216 (2010) 295–302.

[68] P. Osorio-Vargas, R. Sanjines, C. Ruales, C. Castro, C. Pulgarin, A.-J. Rengifo- Herrera, J.-C. Lavanchy, J. Kiwi, J. Photochem. Photobiol. A 220 (2011) 70–76.

[69] S.P. Bugaev, N.S. Sochugov, K. V. Oskomov, A. A. Solovjev, and A. N. Zakharov, Laser and Particle Beams 21 (2003) 279.

[70] B. Window, Recent advances in sputter deposition, Surface and Coatings Technology 71 (1995) 93.

[71] G. Beister, E. Dietrich, C. Schaefer, M. Schere, J. Szczyrbowski, Surface & Coatings Technology,776 (1995) 76-77.

[72] N. Hosokawa, Thin Solid Films, 136 (1996) 281-282.

[73] D. Degout, G. Farges, E. Bergmann, F. Dupont, Surface & Coatings Technology,57 (1993) 105.

[74] B. Window, N. Savvides, *J Vac Sci Technol* A; *4*(*2*) *(1986) 196*–202.

[75] S.M. Rossnagel, J.J. Cuomo et W.D. Westwood: Handbook of Plasma Processing Technology. Noyes Publications, New Jersey, USA, 1990.

[76] C Vitelaru, C Aniculaesei, L de Poucques, T M Minea, C Boisse-Laporte, J Bretagne and G Popa, J. Phys. D: Appl. Phys. 42 (2010) 124013.

[77] I. Safi. , a review Surface and Coatings Technology 127 (2000). 203-219.

[78] J.C Imbert, L de Poucques, C Boisse-Laporte, J Bretagne, M.C Hugon, D Pagnon, P Pitach, L Teule-Gay, M Touzeau, Thin Solid Films 516 (2008) 4700

[79] S. Schiller, K. Goedicke, J. Reschke, V. Kirchhoff, S. Schneider, F. Milde, Surface & Coatings Technology, 61(1993) 331.

[80] S. Schiller, K. Goedicke, V. Kirchhoff, Paper Presented at the 7th International Conference on Vacuum Web Coating, Miami,FL, USA, November 1993, pp. 2-18.

[81] P. Frach, U. Heisig, C. Gottfried, H. Walde, Surface Coatings Technol. 59 (1993) 177-183.

[82] B.J. Pond, T. Du, J. Sobczak, C.K. Carniglia, Proceedings of the Optical Society of America Annual Meeting, September 1992, pp. 1-36.

[83] A. Belkind , A. Freilich, R. Scholl, 108–109 (1998) 558–563.

[84] P.S. Henderson, P.J. Kelly, R.D. Arnell, H. Backer, J.W. Bradley, Surface & Coatings Technology, 174 –175 (2003) 779–783.

[85] R.D. Arnell, P.J. Kelly, J.W. Bradley, Surface & Coatings Technology, 188–189 (2004) 158–163.

[86] D.A.Glocker, J. Vac Sci. Technol. A 11, 6. (1993) 2989.

[87] J.W. Bradley, H. Backer, P.J. Kelly, R.D. Arnell, Surface & Coatings Technology,135 (2001) 221.

[88] J.W.Lee, J.J. Cuomo, M. Bourham, J. Vac Sci. Technol, A 22, 2 (2004) 260.

[89] H. Bartzsch, P. Frach, K. Goedicke, Surface & Coatings Technology 132 (2000) 244-250.

[90] U. Helmersson, M. Lattemann, J. Alami, J. Bohlmark, A.P. Ehiasarian, J.T. Gudmundsson, 48th Annual Technical Conference of the Society of Vacuum Coaters, April 23–28, 2005, Denver, CO, USA, 2005, p. 458.

[91] M. Ganciu, S. Konstantinidis , Y. Paint,. J-P Dauchot, M. hecq,L. de Poucques, P. Vasina, M. Mesko, J-C. Imbert, J. Bretagne, M. Touzeau, J. Optoelectron. Adv. Mater. **7** (2005) 2481

[92] U. Helmersson , M. Lattemann , J. Bohlmark, A. P. Ehiasarian ,J. T.Gudmundsson. Thin Solid Films, 513 (2006) 1–24.

[93] P.J. Kelly, D.R. Arnell, Vacuum 56 (2000) 159-172.

[94] K. Macák, V. Kouznetsov, J. Schneider, U. Helmersson and I. Petrov, J. Vac. Sci. Technol., A,Vac. Surf. Films, 18 (2000) 1533.

[95] J.T. Gudmundsson, J. Alami and U. helmersson. Surf. Coat. Technol, 161 (2002) 249.

[96] A.P. Ehiasarian, W.D. Munz, L. Hultmann U. helmersson and I. Petrov, Surface & Coatings Technology 163 (2003) 267.

[97] S.P. Bugaev, V.G. Podkovyrov, K.V. Oskomov, S.V. Smaykina and N. S. Sochugov, Thin Solid Films, 389 (2001) 16.

[98] D.J. Christie, *Journal* of *Vacuum Science & Technology* A, Vac. Surf. Films, 23 (2005) 330.

[99] S.P. Bugaev, N.N. Koval, N.S. Sochugov, A.N. Zakharov, Proceedings of the XVIIth International Symposium on Discharges and Electrical Insulation in Vacuum, July 21–26, 1996 Berkeley, CA, USA, 1996, p. 1074.

[100] S. Konstantinidis, J.P. Dauchot, M. Ganciu, M. Hecq, J. Appl. Phys. 99 (2006) 013307.
[101] J. Vlček, A.D. Pajdarová, J. Musil, Contrib. Plasma Phys. 44 (2004) 426.
[102] W.D. Sproul, D.J. Christie, D.C. Carter, F. Tomasel, T. Linz, Surf. Eng. 20 (2004) 174.
[103] N. Hosokawa, T. Tsukada, H. Kitahara, Proceedings of the 8th International Vacuum Congress, Sept. 22–26, 1980, Cannes, France, vol. 1, 1980, p. 11.
[104] M.E. Graham, W.D. Sproul, Society of Vacuum Coaters, 37th Annual Technical Conference Proceedings, 1994, pp. 275-279.
[105] A. Okamoto, T. Serikawa, Thin Solid Films 137 (1986) 143-151.
[106] S. PalDey, S.C. Deevi, Mater. Sci. Eng., A Struct. Mater.: Prop. Microstruct. Process. 342 (2003) 58.
[107] O. Knotek, W.D. Mqnz, T. Leyendecker, *Journal* of *Vacuum Science & Technology* A Vac.Surf. Films, 5 (1987) 2173.
[108] J. Probst, U. Gbureck, R. Thull, Surface & Coatings Technology,148 (2001) 226.
[109] R. Lamni, E. Martinez, S.G. Springer, R. Sanjine´s, P.E. Schmid, F. Le´vy, Thin Solid Films 447 –448 (2004) 316–321
[110] R. Lamni, R. Sanjine´s, F. Le´vy, Thin Solid Films 478 (2005) 170– 175.
[111] Z. Kertzman, J. Marchal, M. Suarez, M.H. Staia, P. Filip, P. Kohli, S.M. Aouadi, J. Biomed. Mater. Res. 84 (2008) 1061–1067.
[112] J.H. Hsieh, C.C. Tseng, Y.K. Chang, S.Y. Chang, W. Wu, Surface & Coatings Technology, 202 (2008) 5586–5589.
[113] P.C. Liu, J.H. Hsieh, C. Li, Y.K. Chang, C.C. Yang, Thin Solid Films 517 (2009) 4956–4960.
[114] Fujishima, A., T.N. Rao, and D.A. Tryk,. Journal of Photochemistry and Photobiology C, 1 (2000) 1-21.
[115] Rincon, A.G. and C. Pulgarin,. Catalysis Today, 101 (2005) 331-344.
[116] Andrew Mills, Soo-Keun Lee Journal of Photochemistry and Photobiology A: Chemistry 152 (2002) 233–247
[117] Huang, Z., Maness, P._C., Blake, D.M., Wolfrum, E.J., Smolinski, S.L., and Jacoby, W.A, Journal of Photochemistry and Photobiology A, 130 (2000) 163–170.
[118] Sunada, K., Watanabe, T., and Hashimoto, K.J. Journal of Photochemistry and Photobiology A, 156 (2003) 227–233.
[119] R. Cai , K. Hashimoto, Y. Kubota, and A. Fujshima, Chem. Lett, 3 (1992) 427–430.
[120] Hoffmann, M.R., Martin, S.T., Choi, W.Y., and Bahnemannt, D.W., Environmental Applications of Semiconductor Photocatalysis, Chem. Rev, 95 (1995) 69–96.

[121] E.R. Carraway, A.J. Hoffman, M.R. Hoffmann, Environ. Sci. Technol, 28 (1994) 786–793.

[122] E. Pelizzetti, C. Minero, P. Piccinini, M. Vincenti, coord. Chem. Rev, 125 (1993) 183–193.

[123] H. Yamashita, M. Harada, J. Misaka, M. Takeuchi, K. Ikeue, M. Anpo, J. Photochem. Photobiol., A, 148 (2002) 257–261.

[124] Y. Inel, D.J. Ertek, , J. Chem. Soc., Faraday Trans., 89 (1993) 129–133.

[125] E. Borgarello, N. Serpone, G. Emo, R. Harris, E. Pelizzettie, C. Minero, Inorg. Chem., 25 (1986) 4499–4503.

[126] E.N. Savinov, Soros. Obraz. Zh., 6 (2000) 52–56.

[127] A. Mills, S.J.Le Hunte, Photocatalysis, J. Photochem. Photobiol., A, 108 (1997) 1–35.

[128] K. Tanaka, M. F. V. Capule, T. Hisanaga, Chem. Phys. Lett. 187 (1991) 73-76.

[129] Jayendran C . Rasaiah, Joseph Hubbard, Robert Rubin, and Song Hi Lee , J. Phys. Chem., 94, (1990) 652-662.

[130] J. Cunnigham, P. Sedlak., J.Photochem.Photobiol A: Chem; 77 (1994) 255-263.

[131] E. J. Wolfrum, D. F. Ollis, Aquatic and Surface Photochemistry. Lewis Publishiers, (1994) 451-463

[132] P. Pichat, C. Guillard, A.Laurence, A.-C. Renard, O.Plaidy, Solar Energy Materials and Solar Cells, 38 (1995) 391-399.

[133] J. C. Ireland, P. Klostermann, E. W. Rice and R. M. Clark, Applied and Environmental Microbiology, 59 (1993) 1668–1670.

[134] M. Bideau, B. Claudel, C. Dubien, L. Faure, H. Kazouan, Journal of Photochemistry and Photobiology A: Chemistry 91 (1995) 137-144.

[135] D.M. Teschner, R. Shumacher and R. Stritzker, Ber. Bunsenges. Phys.Chem., 90 (1986) 593.

[136] J. Fernandez, J. Bandara, A. Lopez, Ph. Buffat, J. Kiwi, Langmuir 15 (1999) 185–192.

[137] M. Dhananjeyan, J. Kiwi, P. Albers, O. Enea, Helv. Chim. Acta 84 (2001) 3433–3445.

[138] T. Yuranova, O. Enea, E. Mielczarski, J. Mielczarski, P. Albers, J. Kiwi, Appl. Catal. B 49 (2004) 39–50.

[139] Roberto L. Pozzo, Miguel A**.** Baltanfis, Alberto E. Cassano, Catalysis Today 39 (1997) 219-231.

[140] Jimmy C. Yu , Hung Yuk Tang , Jiaguo Yu , H.C. Chan, Lizhi Zhang, Yinde Xie, H. Wang, S.P. Wong Journal of Photochemistry and Photobiology A: Chemistry 153 (2002) 211–219.

[141] Akinori Yamamoto, Hiroaki Imai, Journal of Catalysis 226 (2004) 462–465.

[142] B. Siffert and J-M. Metzger, Colloids and Surfaces, 53 (1991) 79-99.

[143] D. S . Kim and S. Y. K wak., Environ. Sci. Technol.**,** 43 (2009) 148–151.

[144] Amrita Pal, Simo O. Pehkonen, Liya E. Yu, and Madhumita B. Ray, Ind. Eng. Chem. Res**,** 47 (2008) 7580–7585.

[145] Jean-Marie Herrmann, Catalysis Today 53 (1999) 115–129.

[146] L. Caballero, K.A. Whitehead, N.S. Allen, J. Verran Journal of Photochemistry and Photobiology A: Chemistry 202 (2009) 92–98.

[147] P. Pizarro, C. Guillard, N. Perol, J.-M. Herrmann. Catalysis Today 101 (2005) 211–218.

[148] A.G. Rincón, C. Pulgarin, Applied Catalysis B: Environmental 44 (2003) 263–284.

[149] Kubelt, J. (2004). Investigations on the rapid transbilayer movement of phospholipids in biogenic membranes. Mathematisch-Naturwissenschaftlichen Fakultät I.Humboldt-Universität zu Berlin. Berlin.

[150] V. Nadtochenko, A. Rincon, S. Stanka, J. Kiwi, J. Photochem. Photobiol. A 169 (2005) 131–137.

[151] J. Kiwi, V. Nadtochenko, Journal of Physical Chemistry B 108 (2004) 17675–17684.

[152] J. Kiwi, V. Nadtochenko, Langmuir 21 (2005) 4631–4641.

[153] Matsunaga, T.; Tomada, R.; Nakajima, T.; Wake, H. FEMS Microbiology. Letters.,29, (1985) 211.

[154] T. Matsunaga, R. Tomoda, T. Nakajima, N. Nakamura, T. Komine, Appl. Environ. Microbiol. 54 (1988) 1330.

[155] T. Saito, T. Iwase, J. Horis, T. Morioka, J. Photochem. Photobiol. B: Biol. 14 (1992) 369.

[156] R. J. Watts, S. H. Kong, M. P. Orr, G. C. Miller and B. E. Henry, Water Research, 29 (1995) 95–100.

[157] Z. X. Lu, L. Zhou, Z. L. Zhang, W. L. Shi, Z. X. Xie, H. Y. Xie, D. W. Pang and P. Shen, Langmuir, , 19 (2003) 8765–8768.

[158] M. Wilson, Journal of Applied Microbiology, 75 (1993) 299–306.

[159]K. Holt, A. Bard, Biochemistry 44 (2005) 13214.

[160] A. Nel, T. Xia, L. Mädler, N. Li, Science 311 (2006) 622.

[161]H.S. Jeong, Y.S. Yeo, C.S. Yi, J. Mater. Sci. 40 (2005) 5407.

[162] S.J. Yeon, Appl. Surf. Sci. 221 (2004) 281.

[163] S Y. Liau, D. C. Read, W. J. Pugh, J. R. Furr, A.D. Russell, Lett. Appl. Microbiol. 25 (1997) 279–83

[164] K. Nomiya, A. Yoshizawa, K. Tsukagoshi, N. C. Kasuga, S. Hirakawa, J. Inorg. Biochem. 98 **(**2004) 46–60.

[165] Q L. Feng, J. Wu, G.Q. Chen, F.Z. Cui, T. N. Kim, J. O. Kim, J. Biomed. Mater. Res. 52 **(**2000) 662

[166] M. Ip, S. L. Lui, V. K. M. Poon, I. Lung, A. Burd, J. Med. Microbiol., 55 (2005) 59.

[167] O. D. Schneider, S. Loher, T. J. Brunner, P. Schimidlin, W. J. Stark, J.Mater. Chem., 18 (2008) 2679.

[168] V. A. Oyanedel-Craver, J. A. Smith, Environ. Sci. Technol., 42 (2008) 927.

[169] S.K Gogoi, P.Gopinath, A. Paul, A. Ramesh, S. Sankar. Ghosh, and A. Chattopadhyay .Langmuir**,** 22 (2006) 9322-9328.

[170] Blake, D. M., P.-C. Maness, Z. Huang, E. J. Wolfrum, J. Huang and W. A. Jacoby. Separation and Purification Methods 28 (1): (1999) 1-50.

[171] J.M. Grace, L. Gerenser, J. Dispersion Sci. Technol. 24 (2003)305–341.

[172] K. Ishibashi, A. Fujishima, T. Watanabe, K. Hashimoto, Electrochemistry Communications 2 (2009) 207–210.

[173] F. Liu, C. Roussel, G. Lagger, P. Tacchini, H. Girault, Analytical Chemistry 77 (2005) 7687–7694.

[174] R. Houk, B. Jacobs, F. Gabaly, N. Chang, D. Graham, S. House, I. Roberstson, M. Allendorf, Frameworks, Nano Letts. 9 (2009) 3413–3418.

[175] P. Kubelka, F. Munk, Zei. Tech. Phys. 12 (1931) 593–601.

[176] A.D. Roming in Metals Handbook 9th ed. 10 Materials Characterization 429, American Society for Metals, (1986).

[177] A. Okada, T. Nikaido, M. Ikeda, K. Okada, J. Yamauchi, R. M. Foxton, H. Sawada, J. Tagami, and K. Matin, Dental Materials Journal, 2008. 27:p. 256–272.

[178] R. Reid, T. Sherwood, the Properties of Gases and Liquid, McGraw-Hill, New York, 1958.

[179] J.B. Lumsden in Metals Handbook 9^{th} ed. 10 Materials Characterization 568, American Society for Metals, (1986).

[180] C.D. Wagner, M.W. Riggs, E.L. Davis, G.E. Müllenberg (Eds.), Handbook of Xray Photoelectron spectroscopy, Perkin-Elmer Corporation Physical Electronics Division, Minnesota, 1979.

[181] A.D. Shirley, Physical Reviews B5 (1972) 4709–4716.

[182] R. Dastjerdi, M. Montazer, Th. Stegmaier, M. Moghadm, Colloids and Surfaces B: Biointerfaces 91 (2012) 280–290.

[183] H. Yaghoubi, N. Thagavinia, K. Alamdari, A. Volinsky, ACS Applied Materials and Interfaces 2 (2010) 2629–2636.

[184] O. Akhavan, R. Azimirad, S. Safa, M.M. Larijani, Journal of Materials Chemistry 20 (2010) 7386–7392.

[185] C.h. Cheng, L.Y. Zhang, R.J. Zhan, Surf. Coat. Technol.200 (2006) 6659.

[186] N. De Geyter, R. Morent, C. Leys, Surf. Coat. Technol. 201 (2006) 2460.

[187] N.Y. Cui, N.M.D. Brown, Appl. Surf. Sci. 189 (2002) 31.

[188] F. Leroux, A. Perwuelz, C. Campagne, N. Behary, J. Adhes. Sci. Technol.20(2006) 939.

[189] J.W. Mathews (Ed.), Epitaxial Growth, Part B, Ch. 4: Nucleation of thin Films, Academic Press, New York, 1975, p. 382.

[190] S. Turner, O. Lebedev, F. Schroeder, D. Esken, A. Fisher, V. Tendeloo, Chem. Mater. 20 (2008) 5622.

[191] U. Evans, E. Arnold Pub. Co., London, 1975, p. 97.

[192] L. Gang, B.G. Anderson, J. Grondelle, R.A. van Santen, Applied Catalysis B 40 (2002) 101–107, and references therein.

[193] H. Tada, K. Teranishi, Y. Inubushi, S. Ito, Langmuir 16 (2000) 3304–3309.

[194] D.P. Dowling, A.J. Betts, C. Pope, M.L. McConnell, R. Eloy, M.N. Arnaud, Surface and Coatings Technology 163–164 (2003) 637–640.

[195] F. Mazille, T. Schoettl, C. Pulgarin,; Appl. Catal. B, 89 (2009) 635-644.

[196] O. Akhavan, E. Ghaderi, J.Phys. Chem. C 113 (2009) 20214–20220.

[197] S. Yumitori, J. Mater.Sci. 35 (2000) 139–146.

[198] Abe Y, Hasegawa T, Kawamura M and Sasaki K, Vacuum76 **(**2004) 1

[199] X. Gao, S. Wang, J. Li, Y. Zheng, R. Zhang, P. Zhou, Y. Yang and Chen L, Thin Solid Films 438 (2004) 455-456

[200] J. F. Weaver and G. B. Hoflund, J. Phys. Chem. 98 **(**1994) 8519

[201] J. F. Weaver and G. B. Hoflund, Chem. Mater.6 (1994) 1693

[202] Y. Chiu, U. Rambabu, M. Hsu, H. Shieh, C. Y. Chin and H. H. Lin, J. Appl. Phys. 94 (2003)1996

[203] H.P. Boehm, Discuss. Faraday Soc. 52 (1971) 264.

[204] M. Kaneko, I. Okura,(Eds.), Photocatalytic Science and Technology, Springer-Kodansha, (2002) 117.

[205] O.V. Krylov, Catalysis by Nonmetals, Academic Press, New York, 1980, p. 248.

[206] A. Bozzi, T. Yuranova, E. Mielczarski, J. Mierzcalski, P.A. Buffat, P. Lais, J. Kiwi, Appl. Catal. B 42 (2003) 289–303.

[207] A. Bozzi, T. Yuranova, J. Mielczarski, J. Kiwi, New J. Chem. 28 (2004)521–528.

[208] O. Baghriche, A.P. Ehiasarian, E. Kusiak-Nejman, A.W. Morawski, C. Pulgarin, R. Sanjines, J. Kiwi, Thin Solid Films 520 (2012) 3567–3573.

[209] Sukdeb Pal, Yu Kyung Tak, and Joon Myong Song, Applied and Environmental Microbiology, Mar. (2007) 1712–1720

[210] N. Stojilovic, E.T. Bender, R.D. Ramsier Progress in Surface Science 78 (2005) 101–184.

[211] P.C. Wong, Y.S. Li and K.A.R. Mitchell, Surf. Rev. Lett. 2 (3) (1995) 297.

[212] P. Marcus, M.E. Bussell, Appl. Surf. Sci 59 (1992) 7.

[213] S. Chen, Y. Yin, D. Wang, Y. Lu, X. Wang, J. Cryst. Growth 282 (2005) 498–505 (and references therein).

[214] A. Ewald, S. K. Glückerman, R. Thull, U. Gbureck, Biomedical Eng.on line 5(2006) 20-32

[215] M. Pourbaix, Atlas of Electrochemical Equilibria in Aqueous Solutions, NACE Int Texas, USA, 1976.

[216] A. Emeline, G. Kateva, V. Rudakova, N. Ryabchuk, N. Serpone, Langmuir 14 (1998) 5011-5022.

[217] K. Sayama; H. Arakawa, J. Phys. Chem. 97 (1993) 531-533.

[218] Y. Ida, T. Watase, M. Shinagawa, M. Watabanbe, M. Chigane, M. Inaba, A. Tasaka, M. Izaki, Chem. Mater. 20 (2008) 1254-1256.

[219] A. Varkey, Solar. En. Mater. & Solar Cells 29 (1993) 253-259.

[220] H. Irie, S. Miura, K. Kamiya, K. Hashimoto, Chem. Phys. Letts. 457 (2008) 202-207.

ملخص

أثبت أن المعالجة الاولية بالبلازما للبوليستر سمحت بزيادة تثبيت ال TiO_2 على البوليستر المانح لأصناف مؤكسدة تحت اشعت ضوء منخفض الشدة. أسرع نسبة لتعطيل البكتيريا القولونية E تم تحديدها عند العينة المعالجة أوليا بالبلازما لمدة 30 دقيقة عن طريق أ) النسبة الأكبر للوظائف المؤكسدة الى الوظائف الكربونية المرجعة أثناء اتصال البكتيريا بالبوليستر كما حددت ب ال XPS . ب) الامتصاص البصري للعينة كما وضحت بال DRS. ج) أعلى تركيز للجذور OH روقب بتقنية التفلور لحمض هيدروكسيد تلفتاريك. وجد دليل على التنظيف الذاتي للعينة بوليستر- TiO_2 بواسطة ال XPS وهذا بانعدام البكتيريا المهدمة من طرف بوليستر- TiO_2. دليل أخر لقابلية التنظيف الذاتي ظهر في قدرة العينة على تعطيل البكتيريا بطريقة متكررة. هدا الدليل تبين عن طريق تفاعلات الأكسدة والاختزال Ti^{4+} / Ti^{3+} التي تحدث أثناء التحفيز الضوئي خلال تعطيل البكتيريا.

تم تغليف البوليستر بطبقات من الفضة بالرش المهبطي المغناطيسي ذي التيار المباشرDCMS و ذي التيار النابض المباشر DCMSP لتعزيز تعطيل بكتيريا القولونية E وتمت مقارنة هذه العملية بتلك المحصل عليها من خلال الرش بتقنية طاقة عالية النبض المغناطيسي HIPIMS. كانت كمية الفضة اللازمة لتعطيل البكتيريا القولونية E بواسطة ال HIPIMS قليلة مقارنة مع DCMS و DCMSP, مظهرة درجة معتبرة من التوفير للمعدن النفيس ولوحظ بصورة متزامنة تعطيل أسرع للبكتيريا مقارنة مع العينات المرشة بتقنيتي DCMS و DCMSP. الطبقات السميكة المحصل عليها بواسطة DCMS و DCMSP اللازمة لتعطيل البكتيريا القولونية E تتألف من تراكمات أو تجمعات سميكة من الفضة مقارنة بطبقات الفضة الرقيقة المحصل عليها بتقنية ال HIPIMS. الرش لمدة زمنية طويلة بواسطة التقنيات الثلاث يؤدي الي تكوين ترسبات من الفضة داكنة بصريا يصل الى حدود امتصاص للفضة ل 1000 نانومتر. بينت تقنية التحليل الكتلي الطيفي و مطيافية الالكترونات الضوئية المثارة بالأشعة السينية أن تقنية الHIPIMS أنتجت كمية أكبر من أيونات الفضة Ag^+ و Ag^{2+} مقارنة بتقنيتي DCMS و DCMSP وهذا بسبب تيار التفريغ عالي الذروة المستعمل في الحالة السابقة و المتمثلة في الكثافة العالية المولدة من الألكترونات في المتر مكعب e^-/m^3 والتوليد الكبير لأيونات الفضة.

تم رش البوليستر بطبقات منZr-Ag-N بواسطة الرش المهبطي المغناطيسي ذي التيار النابض المباشر (DCMSP) في جو من N_2 +Ar . ZrN على سطح البوليستر يتفاعل مع Ag يؤدي الى طبقة من Zr-Ag-N. تم اظهار ذرات الفضة بتقنية المجهر الالكتروني الماسح والنفادي بانعدام دوبانيتها في طبقات Zr-Ag-N. هذه الأخيرة كانت أكبر فعالية في تعطيل بكتيريا القولونية مقارنة بطبقات الفضة. حركية تعطيل البكتيريا على سطح البوليستر مرش ب Zr-Ag-N كانت 4 مرات أسرع مقارنة بتلك المرشة بالفضة لوحدها على البوليستر.لم يقدم عنصر الزركنيوم المرش على البوليستر تحت الغلاف الجوي N_2 أي نشاط مضاد للبكتيريا في حد ذاته عند رشه لأوقات قصيرة أقل من واحد دقيقة. العينة Zr-Ag-N البوليستر المرشة لمدة 20 ثانية عند 0.3 أمبير أدت إلى أسرع حركية لتعطيل البكتيريا القولونية.E في غضون 90 دقيقة. ولكن تم تسريع حركية تعطيل البكتيريا القولونية .E على العينة Zr-Ag-N مرتين تحت اشعت ضوء منخفض الشدة(نانومتر 700-400)، $4\ mW/cm^2$. العينة مكونة من جسيمات الفضة ذات أحجام من 15-40 نانومتر وسمك طبقة مابين 30-45 نانومتر تغطي 70-60٪ من ألياف البوليستر في اتجاه تدفق أيونات الفضة من مصدر الفضة. رش الفضة لمدة 20 ثانية يعطي النسبة الأمثل من حجم تحميل الفضة الى تراكم الفضة مع أكبر كمية من مواقع الفضة المحصورة في مواقع مفتوحة على سطح البوليستر. جسيمات النانو الفضية المرشوشة لمدة 20 ثانية تتجمع في شكل وحدات كبيرة تؤدي الى وقت أطول لتعطيل البكتيريا. تزداد الخشونة و خاصية كره الماء لطبقات Zr-Ag-N المرشوشة تزامنا مع الزيادة في سمك الZr-Ag-N عند الرش لمدة طويلة. أظهرت أغطية الZr-Ag-N توزيع معدني موحد و لون رمادي بني مائل شفاف. نوقشت الشحنة المنقولة من Ag_2O و ZrO_2 و المحفزة ضوئيا من حيث المواقع المحتملة للروابط الالكترونية لكلا المؤكسدين مع الأخذ بعين الاعتبار ميكانيزم انتقال الشحنة بينيا (IFCT) لشرح عملية ادخال الالكترون المحفز ضوئيا.

تقنيات التحليل السطحي مثل التفلور بالأشعة السينية (XRF)، التحليل الانعكاس الطيفي (DRS)، المجهر الإلكتروني الماسح والنفادي (EM)، انعراج الأشعة السينية (XRD)، زاوية الاتصال (CA) ومطيافية الالكترونات الضوئية المثارة بالأشعة السينية (XPS) أستعملت لوصف البنية المجهرية لاسطح TiO_2، Ag ، Zr-Ag-N و Zr -N- وتقديم أدلة على تدمير البكتيريا القولونيةE على هذه الأسطح.

كلمات مفتاحية :البكتيريا القولونية ، TiO_2 تحفيز ضوئي، -RF البلازما، الفضة، طاقة عالية النبض المغناطيسي (HIPIMS)، بالرش المهبطي المغناطيسي ذي التيار المباشرDCMS، ومطيافية الالكترونات الضوئية المثارة بالأشعة السينية .(XPS).

Résumé

Dans le cas d'un prétraitement RF-plasma de polyester, l'amélioration de la génération des espèces oxydantes/radicaux, induite par TiO_2 sous irradiation en lumière actinique/visible de faible intensité, est mise en évidence. Après 30 min de prétraitement, l'inactivation bactérienne la plus rapide a été détectée par (a) le rapport le plus élevé des fonctions oxydées/fonctions-C réduites des bactéries en contact du polyester déterminé par l'XPS, b) la forte absorption optique de l'échantillon obtenue par DRS et (c) la concentration de surface maximale des radicaux-OH contrôlée par la fluorescence de l'acide hydroxy-téréphtalique. Le caractère autonettoyant du polyester-TiO_2 a été démontré par l'XPS suite à l'absence de la destruction des bactéries sur ce support. Une preuve supplémentaire du caractère autonettoyant est la capacité de l'échantillon à inactiver les bactéries de façon répétitive. Ceci est expliqué par les réactions d'oxydo-réduction Ti^{4+}/Ti^{3+} s'effectuant au niveau du photocatalyseur durant l'inactivation bactériennes.

Le revêtement du polyester de films-Ag par DC-magnétron (DCMS) et DCMS-pulsé a été réalisé afin d'induire l'inactivation d'E. coli sur le polyester-TiO_2 et a été comparé au Magnétron pulsé de haute puissance « HIPIMS ». Les quantités d'Ag nécessaires pour l'inactivation d'E. coli par HIPIMS étaient inférieures à celles des DCMS et DCMSP indiquant un important gain du métal noble. En même temps, par rapport à des échantillons pulvérisés avec DCMS et DCMSP, une inactivation plus rapide d'E. coli a été enregistrée. Par DCMS et DCMSP, les couches les plus épaisses nécessaires pour l'inactivation contenaient plus d'agrégats-Ag par comparaison aux couches-Ag les plus minces, pulvérisées par HIPIMS. Un temps plus long de pulvérisation par les trois techniques entraîne des dépôts-Ag optiquement sombres jusqu'à la limite d'absorption de l'argent (environ 1000 nm). Les analyses de la spectrométrie de Mass et de la spectroscopie de photoélectrons X indiquent que le HIPIMS produit une quantité d'Ag^{1+} et Ag^{2+} beaucoup plus importante par rapport au DCMS et DCMSP en raison du pic supérieur du courant de décharge utilisé dans le premier cas.

Des films de Zr-Ag-N ont été déposés sur du polyester par DCMSP dans une atmosphère d'Ar + N_2. Le ZrN, sur la surface du polyester, interagit avec Ag et conduit à des films de Zr-Ag-N. Les analyses TEM montrent que les atomes Ag sont non miscibles avec les couches ZrN. Du point de vue inactivation d'E. coli, ces derniers composites ont été plus actifs que les films Ag. La cinétique d'inactivation, sur les surfaces du polyester Zr-Ag-N, était 4 fois plus rapide par rapport aux échantillons pulvérisés sur le polyester sous vide en présence d'Ag seulement. La pulvérisation Zr en atmosphère N_2 n'a présenté aucune activité antibactérienne lorsqu'elle est appliquée pendant des périodes très courtes (< 1minute). L'échantillon du polyester Zr-Ag-N pulvérisé pendant 20 s à 0,3 Amp conduit à une cinétique d'inactivation plus rapide durant les 90 min de contact. Cependant, la cinétique d'inactivation d'E. coli sur Zr-Ag-N a été deux fois plus accélérée sous une lumière visible/actinique de faible intensité (400-700 nm, 4 mW/cm^2). L'échantillon est constitué de particules d'Ag avec des tailles de 15-40 nm, au sein d'une couche de 30-45 nm d'épaisseur couvrant ~ 60-70% de la fibre de polyester dans le sens de AgO/flux-d'ions-Ag de la cible-Ag. La pulvérisation d'Ag pendant 20 s conduit au rapport optimal Ag-chargé/taille du cluster d'Ag avec le plus grand nombre de sites d'Ag détenus dans des positions exposées sur la surface du polyester. Les nanoparticules Ag pulvérisés à des temps > 20 s, s'agglomèrent en plus grandes unités qui mènent à des temps d'inactivation bactérienne plus longs. L'augmentation de l'épaisseur de Zr-Ag-N à des temps de pulvérisation plus importants conduit à un accroissement simultané de la rugosité et du caractère hydrophobe des couches pulvérisées de Zr-Ag-N. Les films Zr-Ag-N présentent une distribution uniforme du métal et une couleur gris-brun semi-transparente. Le transfert photo-induit des charges d'Ag2O et ZrO_2 est discuté en considérant les positions relatives des bandes électroniques des deux oxydes. Dans ce contexte, on doit tenir compte du mécanisme de transfert interfacial de charges (IFCT) pour expliquer l'injection photo-induite d'électrons.

Différentes techniques d'analyse de surface telles que la fluorescence de Rayons-X (XRF), la spectroscopie de réflectance diffuse (DRS), la microscopie électronique (EM), la diffraction des rayons-X (XRD), les mesures de l'angle de contact (CA) et la spectroscopie de photoélectrons X (XPS) ont été appliquées afin de révéler la microstructure de la surface de TiO_2, Ag, ZrN et Zr-Ag-N et apporter la preuve de la destruction d'*E. coli* sur ces surfaces.

Mots clés : *E. coli*, Photocatalyse TiO_2, Plasma-RF sous vide, Ag, HIPIMS, DCMS, XPS.

Abstract

Evidence is presented for the RF-plasma pretreatment of polyester enhancing the TiO_2 induced generation of oxidative species/radicals under a low intensity actinic/visible light irradiation. After 30 min RF-plasma pretreatment, the fastest bacterial inactivation was detected by (a) the largest ratio of oxidized-functionalities / reduced C-functionalities on the bacteria contacted polyester as determined by XPS, b) the sample optical absorption as seen by DRS and (c) the highest concentration surface OH-radicals monitored by the fluorescence of the hydroxy-terephthalic acid. Evidence for the TiO_2-polyester self-cleaning was found by XPS by the lack of bacteria destruction on the polyester-TiO_2. A further proof of self-cleaning was the sample ability to inactivate bacterial in a repetitive way. Evidence is presented by Ti^{4+}/Ti^{3+} redox reactions occurring in the photocatalyst during bacterial inactivation.

DC-magnetron sputtering (DCMS) and DCMS-pulsed coating of Ag-films on polyester was carried out to induce *E. coli* inactivation and compared with highly intensity pulse plasma power magnetron sputtering (HIPIMS). The amounts of Ag needed to inactivate *E. coli* by HIPIMS sputtering were an order of magnitude lower than with DCMS and DCMSP indicating a significant saving of noble metal. Concomitantly a faster *E. coli* inactivation was observed compared to samples sputtered with DCMS and DCMSP. By DCMS and DCMSP the thicker layers needed to inactivate *E. coli* comprised larger Ag-aggregates compared to the thinner Ag-layers sputtered by HIPIMS. Longer sputtering times by DCMS, DCMSP and HIPIMS lead to optically darker Ag-deposits up to the absorption edge of silver of ~1000 nm. Mass spectroscopic analyses and X-ray photoelectron spectroscopy indicated that HIPIMS produced a much higher amount of Ag^{1+} and Ag^{2+} compared to DCMS and DCMSP due to the higher peak discharge current employed in the former case, the higher density generated of e^-/m^3 and the much higher generation of Ag-ions compared to DCMS sputtering.

Zr-Ag-N films were deposited on polyester by direct current pulsed magnetron sputtering (DCMSP) in an Ar + N_2 atmosphere. ZrN on the polyester surface interacts with Ag leading to Zr-Ag-N films. The Ag-atoms are shown by TEM to be immiscible with the ZrN-layer. These composite films were more active in *E. coli* inactivation compared to the Ag-films. The *E. coli* inactivation kinetics on Zr-Ag-N polyester surfaces was about 4 times compared to samples sputtering only Ag under vacuum on the polyester. Sputtering Zr in N_2 atmosphere presented no antibacterial activity by itself when applied for short times below one min. The Zr-Ag-N polyester sample sputtered for 20 s at 0.3 Amp led to the fastest antibacterial *E. coli* inactivation kinetics within 90 min. but the E. coli inactivation kinetics on Zr-Ag-N was accelerated two times under low intensity visible/actinic light (400–700 nm, 4 mW/cm^2). The sample consisted of Ag-particles with sizes of 15–40 nm, within a layer thickness of 30–45 nm covering ~60–70% of the polyester fiber in the direction of the AgO/Ag-ion-flux from the Ag-target. Ag sputtering for 20 s leads to the optimal ratio of Ag-loading/Ag cluster size with the highest amount of Ag-sites held in exposed positions on the polyester surface. The Ag-nanoparticles sputtered for times >20 s agglomerated to bigger units leading to longer bacterial inactivation times. The increase in thickness of the Zr-Ag-N at longer sputtering times lead to a concomitant increase in the rugosity and hydrophobic character of the Zr-Ag-N sputtered layers. The Zr-Ag-N films showed a uniform metal distribution and a semi-transparent gray-brown color. The photo-induced charge transfer from Ag_2O and ZrO_2 is discussed considering the relative positions of the electronic bands of the two oxides. Taking into consideration the interfacial charge transfer mechanism (IFCT) to explain the photo-induced electron injection.

Surface techniques analysis such as X-ray fluorescence (XRF), diffuse reflectance spectroscopy (DRS), electron microscopy (EM), X-ray diffraction (XRD), contact angle (CA) measurements and X-ray photoelectron spectroscopy (XPS) were applied to describe the microstructure of the surface of TiO_2, Ag, ZrN and Zr-Ag-N and provide evidence for the destruction of *E. coli* on these surfaces.

Keywords: *E. coli*, TiO_2 photocatalysis, Vacuum RF-plasma, Ag, HIPIMS, DCMS, XPS.

PUBLICATIONS:

1- O. Baghriche, C. Ruales R. Sanjines, C. Pulgarin, A. Zertal, I. Stolitchnov, J. Kiwi, Surface & Coatings Technology 206 (2012) 2410–2416.

2- Oualid Baghriche, Abed Zertal, Arutiun P. Ehiasarian, R. Sanjines, Cesar Pulgarin, Ewelina Kusiak-Nejman, Antoni W. Morawski, John Kiwi, Thin Solid Films 520 (2012) 3567–3573

3- O. Baghriche, A.P. Ehiasarian, E. Kusiak-Nejman, C. Pulgarin, R. Sanjinesd, A.W. Morawski,J. Kiwi, Journal of Photochemistry and Photobiology A: Chemistry 227 (2012) 11– 17.

4- O. Baghriche, J. Kiwi, C. Pulgarin, R. Sanjines, Journal of Photochemistry and Photobiology A: Chemistry 229 (2012) 39– 45

5- S. Rtimi, O. Baghriche, R. Sanjines, C. Pulgarin, M. Ben-Simon, J.-C. Lavanchy, A. Houas, J. Kiwi, Applied Catalysis B: Environmental 123– 124 (2012) 306– 315

6- E. Kusiak-Nejman, A.W. Morawski, A. P. Ehiasarian, C. Pulgarin, O. Baghriche, E. Mielczarski, J. Mielczarski, A. Kulik, and J. Kiw, J. Phys. Chem. C 2011, 115, 21113–21119

7- O. Baghriche, S. Rtimi, C. Pulgarin, R. Sanjines, and J. Kiwi, ACS Appl. Mater. InterfacesAccepted: August 30, 2012

8- Mamoru Senna, Nicholas Myers, Anne Aimable, Vincent Laporte, Cesar Pulgarin, Oualid Baghriche and Paul Bowen, J. Mater. Res., 2012

9- S. Rtimi, O. Baghriche, C. Pulgarin, R. Sanjines and J. Kiwi, RSC Advances, 2012, 2, 8591–8595